

THE UNIVERSITY OF CHICAGO

FIRST SEARCH FOR  $K_L \rightarrow \pi^0 \pi^0 \nu \bar{\nu}$  AND  $K_L \rightarrow \pi^0 \pi^0 P$

A DISSERTATION SUBMITTED TO  
THE FACULTY OF THE DIVISION OF THE PHYSICAL SCIENCES  
IN CANDIDACY FOR THE DEGREE OF  
DOCTOR OF PHILOSOPHY

DEPARTMENT OF PHYSICS

BY

JONATHAN D. NIX

CHICAGO, ILLINOIS

JUNE 2007

Copyright © 2007 by Jonathan D. Nix

All rights reserved

*Dedicated to my parents.*

## ABSTRACT

We describe the first search for the rare kaon decay  $K_L \rightarrow \pi^0 \pi^0 \nu \bar{\nu}$ . This search was performed by the E391a collaboration at the KEK 12-GeV proton synchrotron. A limit of  $4.7 \times 10^{-5}$  at the 90% confidence level is set. Additionally, we perform a search for the supersymmetric decay mode  $K_L \rightarrow \pi^0 \pi^0 + \text{Sgoldstino}$  up to sgoldstino masses of 200 MeV where we set a limit of  $1.2 \times 10^{-6}$ .

The bifurcation analysis technique for background prediction using data, but maintaining a closed signal box is described. The result is extended to two background sources. Conditions on the applicability under correlated cuts are described. This technique is applied to both a toy model and the background prediction for the searches described above.

## ACKNOWLEDGMENTS

I would like to thank the members of the E391a collaboration which made this work possible. I would also like to thank the staff of KEK for their invaluable work in maintaining and operating the KEK-PS.

I would also like to thank the Grainger Foundation for their generous support.

# TABLE OF CONTENTS

ABSTRACT . . . . .	iv
ACKNOWLEDGMENTS . . . . .	v
LIST OF FIGURES . . . . .	x
LIST OF TABLES . . . . .	xiii
<b>1 INTRODUCTION AND THEORY . . . . .</b>	<b>1</b>
1.1 Flavor Physics in the Kaon System . . . . .	2
1.2 The $K_L \rightarrow \pi^0 \pi^0 \nu \bar{\nu}$ Decay in the Standard Model . . . . .	3
1.2.1 Kinematics of $K_L \rightarrow \pi^0 \pi^0 \nu \bar{\nu}$ . . . . .	5
1.2.2 $K_L \rightarrow \pi^0 \pi^0 \nu \bar{\nu}$ Form Factor . . . . .	7
1.3 Supersymmetry . . . . .	9
1.3.1 The Pseudoscalar Sgoldstino . . . . .	10
1.4 The $K_L \rightarrow \pi^0 \pi^0 P$ Decay . . . . .	10
1.4.1 Branching Ratio and Supersymmetry Parameters . . . . .	11
1.4.2 Decay of the Sgoldstino . . . . .	12
1.5 Previous Limits . . . . .	13
1.5.1 Other Kaon Experiments . . . . .	13
1.5.2 Astrophysical . . . . .	13
1.5.3 Laboratory . . . . .	15
1.5.4 Evidence for a pseudoscalar . . . . .	15
<b>2 E391A EXPERIMENT . . . . .</b>	<b>17</b>
2.1 The E391a Beam . . . . .	17
2.1.1 Beam Profile . . . . .	18
2.2 Detector Overview . . . . .	20
2.2.1 Vacuum System . . . . .	22
2.3 Collar Counters . . . . .	23
2.3.1 Collar Counter 2 . . . . .	23
2.3.2 Collar Counter 3 . . . . .	25
2.3.3 Collar Counters 4 & 5 . . . . .	27
2.3.4 Collar Counter 6 & 7 . . . . .	28
2.3.5 Calibration of Collar Counters . . . . .	28
2.4 Main Barrel . . . . .	29
2.4.1 Calibration . . . . .	29
2.5 Front Barrel . . . . .	32
2.5.1 Calibration . . . . .	32
2.6 Barrel Charge Veto . . . . .	32

2.6.1	Calibration . . . . .	32
2.7	Back-Anti . . . . .	33
2.7.1	Calibration . . . . .	35
2.8	Charge Veto . . . . .	36
2.8.1	Calibration . . . . .	36
2.9	CsI Array . . . . .	36
2.9.1	Calibration Methods . . . . .	37
2.9.2	Cosmic Calibration . . . . .	38
2.9.3	$\pi^0$ Calibration . . . . .	38
3	DAQ SYSTEM . . . . .	41
3.1	Overview . . . . .	41
3.2	Triggering . . . . .	41
3.2.1	Hardware Cluster . . . . .	41
3.2.2	Online Vetoes . . . . .	42
3.2.3	Physics Trigger . . . . .	43
3.2.4	Accidental Triggers . . . . .	43
3.2.5	Calibration & Pedestal Triggers . . . . .	44
3.3	Timing . . . . .	44
3.3.1	Calibration . . . . .	44
4	MONTE CARLO SIMULATION . . . . .	47
4.1	Event Generation . . . . .	47
4.2	Samples . . . . .	47
4.2.1	Decay Region . . . . .	48
4.2.2	Energy Cut-offs . . . . .	48
4.3	Accidental Overlay . . . . .	49
4.4	Data and Monte Carlo Comparison . . . . .	49
5	RECONSTRUCTION . . . . .	53
5.1	Clustering . . . . .	53
5.1.1	Cluster Position . . . . .	54
5.1.2	Cluster Energy Recalculation . . . . .	54
5.1.3	Cluster Timing . . . . .	54
5.2	$\pi^0$ Reconstruction . . . . .	55
5.2.1	Z Vertex . . . . .	55
5.2.2	Selection of Pairing . . . . .	58
5.2.3	Transverse Momentum . . . . .	58
5.3	Normalization Modes . . . . .	59
5.3.1	$2\pi^0$ Mode . . . . .	59
5.3.2	$3\pi^0$ Mode . . . . .	59
5.4	Signal Modes . . . . .	60
5.4.1	$K_L \rightarrow \pi^0 \pi^0 \nu \bar{\nu}$ . . . . .	60

5.4.2	$K_L \rightarrow \pi^0 \pi^0 P$	60
5.4.3	Signal Box	61
5.5	Cut Philosophy	61
5.6	Veto Cuts	63
5.7	Gamma Quality Cuts	63
5.7.1	Neural Network for Fusion Identification	63
5.7.2	Training the Neural Network	65
5.7.3	Energy Cut	66
5.7.4	Gamma Fiducial Cut	66
5.7.5	Gamma EDI	67
5.7.6	Gamma TDI	67
5.7.7	Gamma R.M.S.	70
5.7.8	Gamma Energy Ratio	70
5.8	Reconstruction Quality Vetoes	71
5.8.1	Best $\chi^2$	71
5.8.2	Second Best $\chi^2$	72
5.9	Acceptance and Flux	72
5.9.1	Non-simulated Cuts	74
5.9.2	Flux	74
5.9.3	Signal Mode Acceptance	76
6	BIFURCATION ANALYSIS TECHNIQUE	79
6.1	One Background Case	79
6.2	Two Background Case	82
6.2.1	Derivation	82
6.2.2	Properties of the Two Background Solution	85
6.2.3	Interpretation of Two Background Solution	87
6.2.4	A Second Derivation	88
6.3	Cut Correlation	92
6.3.1	Impact of Cut Correlation	93
6.4	Discussion	96
7	TOY MODEL OF THE BIFURCATION ANALYSIS TECHNIQUE	98
7.1	The Model	98
7.1.1	Cuts	100
7.2	One Background	100
7.2.1	Cut Correlation	101
7.3	Two Backgrounds	102
7.3.1	One background calculation	104
7.3.2	Correction	104
7.3.3	Model 2	105

8	BACKGROUND ANALYSIS . . . . .	107
8.1	Kaon Background Modes . . . . .	107
8.1.1	$K_L \rightarrow \pi^0 \pi^0 \pi^0$ . . . . .	107
8.1.2	$K_L \rightarrow \pi^0 \pi^0$ . . . . .	108
8.1.3	Charged Kaon Decays . . . . .	110
8.2	Neutron Background . . . . .	110
8.2.1	Core Neutrons . . . . .	111
8.2.2	Halo Neutrons . . . . .	111
8.3	Application of the Bifurcation Analysis . . . . .	111
8.4	Background Prediction Errors . . . . .	113
8.4.1	Core Neutron Background . . . . .	114
8.4.2	Other $K_L \rightarrow \pi^0 \pi^0 \pi^0$ Background Channels . . . . .	117
8.4.3	Correlation . . . . .	118
8.4.4	Combining Systematic Errors . . . . .	118
9	RESULTS AND ERROR ANALYSIS . . . . .	120
9.1	Single Event Sensitivity . . . . .	120
9.2	Opening the Box . . . . .	120
9.2.1	Limit . . . . .	120
9.3	Error Analysis . . . . .	122
9.3.1	Acceptance and Flux Errors . . . . .	122
9.3.2	Energy Calibration Errors . . . . .	123
9.3.3	Other Cuts . . . . .	123
9.3.4	Non-Simulated Cuts . . . . .	124
9.3.5	Single Event Sensitivity Error . . . . .	124
10	CONCLUSIONS . . . . .	126
10.1	Results . . . . .	126
10.2	Future Prospects . . . . .	126
	REFERENCES . . . . .	128

## LIST OF FIGURES

1.1	An unitarity triangle. . . . .	3
1.2	The short-ranged Feynman diagrams which contribute to $K_L \rightarrow \pi^0 \pi^0 \nu \bar{\nu}$ . . . . .	4
1.3	The $K_L \rightarrow \pi^0 \pi^0 \nu \bar{\nu}$ decay into dipion and dilepton systems. . . . .	6
1.4	$K_L \rightarrow \pi^0 \pi^0 P$ Diagram . . . . .	11
1.5	$K^- \rightarrow \pi^- \pi^0 P$ results from ISTR A . . . . .	14
2.1	The e391a neutral beamline. . . . .	18
2.2	Schematic diagram of e391a collimation system. . . . .	19
2.3	Beam Profile. . . . .	21
2.4	The e391a detector. . . . .	22
2.5	E391a detector vacuum regions . . . . .	23
2.6	Picture of vacuum membrane . . . . .	24
2.7	Cross section of one of the CC02 modules . . . . .	25
2.8	Energy deposit in CC02 in GeV . . . . .	26
2.9	Energy deposit in CC03 in GeV. . . . .	26
2.10	Diagram of CC04 . . . . .	27
2.11	Energy deposit in CC05 in GeV. . . . .	28
2.12	Schematic diagram of calibration procedure for the Main Barrel. . . . .	30
2.13	Schematic diagram of calibration cosmic muons for Front Barrel(red) and Main Barrel(blue). . . . .	31
2.14	Energy deposit in Main Barrel in GeV. . . . .	31
2.15	Energy deposit in Front Barrel in GeV. . . . .	33
2.16	Diagram of the Back-Anti detector and the Beam Hole Charged Veto. . . . .	34
2.17	Back-Anti energy deposit for muons. . . . .	35
2.18	CsI energy resolution . . . . .	37
2.19	Diagram of geometry of pion target run. . . . .	39
2.20	Reconstructed kaon mass distribution for good $K_L \rightarrow \pi^0 \pi^0 \pi^0$ events. . . . .	40
3.1	Layout of CsI Hardware Clusters. . . . .	42
3.2	Signal propagation between PMT and TDC. . . . .	45
3.3	Time-difference distribution among $6\gamma$ 's for $K_L \rightarrow \pi^0 \pi^0 \pi^0$ [18]. . . . .	46
4.1	Reconstructed invariant mass for data and Monte Carlo for $4\gamma$ events. . . . .	50
4.2	Reconstructed $Z$ decay vertex for $4\gamma$ events. . . . .	51
4.3	Monte Carlo-data comparison in $K_L \rightarrow \pi^0 \pi^0$ signal region. . . . .	52
5.1	Diagram of clustering procedure. . . . .	53
5.2	Reconstruction of pion decay vertex. . . . .	56
5.3	Distribution of Monte Carlo $K_L \rightarrow \pi^0 \pi^0$ events in the $P_T$ -Mass plane. . . . .	60
5.4	Event distributions in the $P_T$ -Mass plane for $K_L \rightarrow \pi^0 \pi^0 \nu \bar{\nu}$ and $K_L \rightarrow \pi^0 \pi^0 P$ signal modes. . . . .	62
5.5	Schematic of neural network. . . . .	64

5.6	The sigmoid function $\sigma(x) = \frac{1}{1+e^{-x}}$ . . . . .	65
5.7	Comparison for Fusion Neural Net output for data and Monte Carlo. Data is represented by the black dots and Monte Carlo by the red line. Samples are normalized by the maximum bin. Lower plot is ratio of Monte Carlo to data. . . . .	66
5.8	Gamma EDI. . . . .	68
5.9	Gamma TDI. . . . .	69
5.10	Cut point for Gamma R.M.S. as a function of cluster size in CsI blocks. . . . .	70
5.11	Gamma RMS. . . . .	71
5.12	Energy ratio. . . . .	72
5.13	Comparison between data and Monte Carlo of $\chi^2$ of vertex reconstruction. . . . .	73
5.14	Comparison between data and Monte Carlo of $\chi^2$ of the second best $\pi^0$ pairing vertex reconstruction. . . . .	73
5.15	$K_L \rightarrow \pi^0\pi^0$ acceptance loss from individual vetoes. . . . .	74
5.16	Single event sensitivity to $K_L \rightarrow \pi^0\pi^0P$ as function of sgoldstino mass. . . . .	78
6.1	Schematic of background distribution in the cut space. . . . .	80
6.2	Cut space with correlated cuts. . . . .	94
7.1	Kinematic variable distributions for Backgrounds 1 and 2. . . . .	99
7.2	Distribution of $a$ for Background 2. . . . .	99
7.3	The value of $\epsilon$ (described in Section 6.3.1 as a function of $\epsilon'$ as given in Equation 7.3.) . . . . .	101
7.4	The statistical correlation, $\rho$ , as a function of $\epsilon$ . . . . .	102
7.5	Predicted and observed background with first order correlation correction. . . . .	103
7.6	Predicted and observed background with practical correlation correction. . . . .	103
7.7	Contour plots of the distribution of $a$ and $b$ for backgrounds 1 and 2 and an equally weighted combination of the two. . . . .	104
7.8	Predicted and observed background for different admixtures of a second background source. . . . .	105
7.9	Predicted and observed background for different admixtures of Background 2 for Model 2. . . . .	106
8.1	$K_L \rightarrow \pi^0\pi^0\pi^0$ Monte Carlo background events in $P_T$ vs invariant mass plane. . . . .	109
8.2	Distribution of Monte Carlo $K_L \rightarrow \pi^0\pi^0\pi^0$ events in $P_T$ - $Z$ plane. . . . .	110
8.3	Reconstructed $Z$ distribution with loose cuts and $P_T$ greater than 100 Mev/c. . . . .	115
8.4	Reconstructed $Z$ distribution with loose cuts and $P_T$ greater than 100 Mev/c with scaled $K_L \rightarrow \pi^0\pi^0\pi^0$ Monte Carlo subtracted. . . . .	116

9.1	Plot of $P_T$ versus invariant mass from data with an opened signal box.	121
9.2	Plot of $P_T$ versus reconstructed $Z$ from data with an opened signal box.	121
9.3	Limits at the 90% confidence level for $K_L \rightarrow \pi^0 \pi^0 \nu \bar{\nu}$ and $K_L \rightarrow \pi^0 \pi^0 P$ decay modes. . . . .	122
10.1	Limits on $ Re(h_{12}^{(D)}) $ versus sgoldstino mass. . . . .	126

## LIST OF TABLES

1.1	A summary of astrophysical limits on the sgoldstino. . . . .	15
1.2	Limits on pseudoscalar sgoldstino couplings. . . . .	16
3.1	Online veto threshold values converted to energy values. . . . .	43
4.1	Monte Carlo samples and their equivalent data size. . . . .	48
4.2	Simulation cut-off values for individual detectors. . . . .	49
5.1	Acceptance loss and signal to noise ratio for individual veto cuts. . .	75
5.2	Flux calculation and non-simulated cut acceptance loss. . . . .	76
5.3	Acceptance and single event sensitivity for the various signal modes. .	77
7.1	Probability distribution functions for the variables of each event type in the Toy Model. . . . .	99
7.2	Cut survival probabilities for each event type. . . . .	100
7.3	Single background study. . . . .	101
7.4	Probability distribution functions for the variables of each event type in Model 2. . . . .	106
8.1	Relative levels of different types of $K_L \rightarrow \pi^0\pi^0\pi^0$ background under different levels of photon separation efficiency. . . . .	109
8.2	Statistical correlation between setup, set A, and set B cuts in $K_L \rightarrow$ $\pi^0\pi^0\pi^0$ background region. . . . .	112
8.3	Background prediction for regions neighboring the signal box. . . . .	113
8.4	Number of events in signal box for various cut conditions and $K_L \rightarrow$ $\pi^0\pi^0\pi^0$ background prediction. . . . .	113
8.5	$K_L \rightarrow \pi^0\pi^0\pi^0$ background survival probability from $K_L \rightarrow \pi^0\pi^0\pi^0$ Monte Carlo. . . . .	117
8.6	Effects of contamination on $K_L \rightarrow \pi^0\pi^0\pi^0$ bifurcation background prediction. . . . .	118
8.7	Contributions to background prediction systematic error. . . . .	119
9.1	Variation in $K_L \rightarrow \pi^0\pi^0$ acceptance due to variation in energy scale for photon vetoes. . . . .	123
9.2	Acceptance loss from non-simulated cuts in different $P_T$ regions. . . .	124
9.3	Contributions to Single Event Sensitivity systematic error. . . . .	125
10.1	Summary of Single Event Sensitivities and Limits . . . . .	127

# CHAPTER 1

## INTRODUCTION AND THEORY

The E391a experiment is the first dedicated experiment to search for the rare kaon decay  $K_L \rightarrow \pi^0 \nu \bar{\nu}$ . It has  $4\pi$  photon veto coverage making it ideal instrument to search for kaon decays with photons in the final state and missing particles. In this thesis, I discuss searches for several decay modes with four photons in the final state.

These modes are the Standard Model mode  $K_L \rightarrow \pi^0 \pi^0 \nu \bar{\nu}$ , the supersymmetric mode  $K_L \rightarrow \pi^0 \pi^0 P$  where  $P \rightarrow$  unobservable. The modes that we are searching for share similar experimental signatures. The  $K_L \rightarrow \pi^0 \pi^0 \nu \bar{\nu}$  mode is predicted to exist within the Standard Model and we will focus on its phenomenology in that case. On the other hand, the  $K_L \rightarrow \pi^0 \pi^0 P$  mode is purely a prediction of certain models of supersymmetry with no Standard Model equivalent. Both of these decays are examples of flavor changing neutral currents.

We begin with an overview of the physics of the neutral kaon system. Kaons are mesons consisting of a strange (or anti-strange) quark and either an up or a down quark. They have isospin of one half and a strangeness of  $\pm 1$ . There are four varieties of kaons, charged kaons,  $K^\pm$ , and two neutral kaons,  $K^0$  and  $\bar{K}^0$ . The neutral kaons can mix through a second-order weak interaction [3]. We therefore observe a linear combination of the neutral kaons. We can form eigenstates of the charge-parity (CP) symmetry,  $K_1$  with  $CP = +1$  and  $K_2$  with  $CP = -1$ . The CP even eigenstate,  $K_1$ , primarily decays to  $2\pi$  which occurs quickly and the CP odd eigenstate,  $K_2$ , primarily decays to  $3\pi$  which occurs on a slower timescale. However, CP is not conserved in weak interaction as first experimentally observed by Cronin and Fitch in 1964 through a decay of the long lived neutral kaon to  $2\pi$ . Therefore, the observed particle wasn't the eigenstate of CP, and rather a mixture of  $K_2$  with a small amount of  $K_1$ , which

we call  $K_L$  [4].

## 1.1 Flavor Physics in the Kaon System

The Standard Model includes three families or flavors of quarks which are distinguished only by their mass. The flavors are conserved by the strong interaction, but the weak force can cause changes of flavors. The kaon system has traditionally been a rich laboratory for the study of these processes. The Lagrangian for the charged weak interaction is given by:

$$-\mathcal{L}_{W^\pm} = \frac{g}{\sqrt{2}} \bar{u}_{Li} \gamma^\mu (V_{uL} V_{dL}^\dagger)_{ij} d_{Lj} W_\mu^\pm + \text{h.c.} \quad (1.1)$$

Here  $\bar{u}_{Li}$  and  $d_{Lj}$  are the left-handed quarks and  $W_\mu^\pm$  is the gauge boson.

In the Standard Model the coupling between flavors of quarks is described by the Cabbibo-Kobayashi-Maskawa (CKM) Matrix. This  $3 \times 3$  unitary matrix contains the couplings between the flavors of quarks:

$$V_{CKM} = V_{uL} V_{dL}^\dagger \quad (1.2)$$

In the Wolfenstein parameterization [5], the matrix is:

$$V_{CKM} = \begin{bmatrix} V_{ud} V_{us} V_{ub} \\ V_{cd} V_{cs} V_{cb} \\ V_{td} V_{ts} V_{tb} \end{bmatrix} = \begin{bmatrix} 1 - \frac{\lambda^2}{2} & \lambda & A\lambda^3(\rho - i\eta) \\ -\lambda & 1 - \frac{\lambda^2}{2} & A\lambda^2 \\ A\lambda^3(1 - \rho - i\eta) & -A\lambda^2 & 1 \end{bmatrix} + \mathcal{O}(\lambda^4). \quad (1.3)$$

The fact that the CKM matrix is unitary requires that the following relationships

are true:

$$V_{ud}V_{us}^* + V_{cd}V_{cs}^* + V_{td}V_{ts}^* = 0, \quad (1.4)$$

$$V_{us}V_{ub}^* + V_{cs}V_{cb}^* + V_{ts}V_{tb}^* = 0, \quad (1.5)$$

$$V_{ud}V_{ub}^* + V_{cd}V_{cb}^* + V_{td}V_{tb}^* = 0. \quad (1.6)$$

These relationships can be represented geometrically by a triangle in the complex plane. The unitarity triangle formed from Eqn 1.4 can be rescaled and with the selection of phase such that  $V_{cd}V_{cb}^*$  is real, the height of the triangle is given by the parameter  $\eta$  and the horizontal position of the vertex is given by  $\rho$ . This triangle is shown in Fig 1.1.

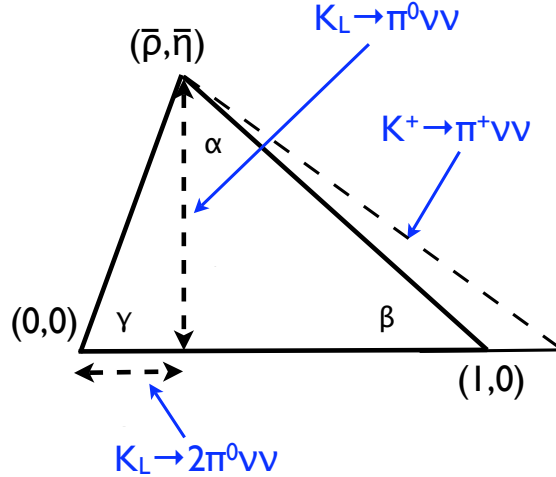


Figure 1.1: An unitarity triangle.

## 1.2 The $K_L \rightarrow \pi^0 \pi^0 \nu \bar{\nu}$ Decay in the Standard Model

The decay  $K_L \rightarrow \pi^0 \pi^0 \nu \bar{\nu}$  is a flavor changing neutral current process. It involves an  $s \rightarrow d \nu \bar{\nu}$  transition. Like the “Golden Mode” of  $K_L \rightarrow \pi^0 \nu \bar{\nu}$ , this mode is not

sensitive to long range interactions so its branching ratio can be predicted with little theoretical uncertainty. This is because as a fully neutral mode it does not suffer from long-range radiative corrections and can be related to a measured semi-leptonic decay mode  $K_{e4}$ . We follow the treatment given in [6].

The effective Lagrangian can be written:

$$\mathcal{L} = \frac{G_F}{\sqrt{2}} \frac{\alpha}{2\pi \sin^2 \theta_W^2} [V_{cs}^* V_{cd} \bar{X}(x_c, y_\ell) + V_{ts}^* V_{td} X(x_t)] \times \bar{s} \gamma_\mu (1 - \gamma_5) d \bar{\nu} \gamma^\mu (1 - \gamma_5) \nu + H.c. \quad (1.7)$$

The functions  $X(x_t)$  and  $\bar{X}(x_c, y_\ell)$  contain the dependence on the charm-quark, top-quark, and tau-lepton masses in terms of  $x_i = M_i^2/M_W^2$  and  $y_\ell = m_\ell^2/M_W^2$ :

$$X(x_t) = \frac{x_t}{8} \left[ \frac{x_t + 2}{x_t - 1} + \frac{x_t - 2}{(x_t - 1)^2} \log x_t \right]. \quad (1.8)$$

The function  $\bar{X}(x_c, y_\ell)$  has a complicated form and can be found in reference [7].

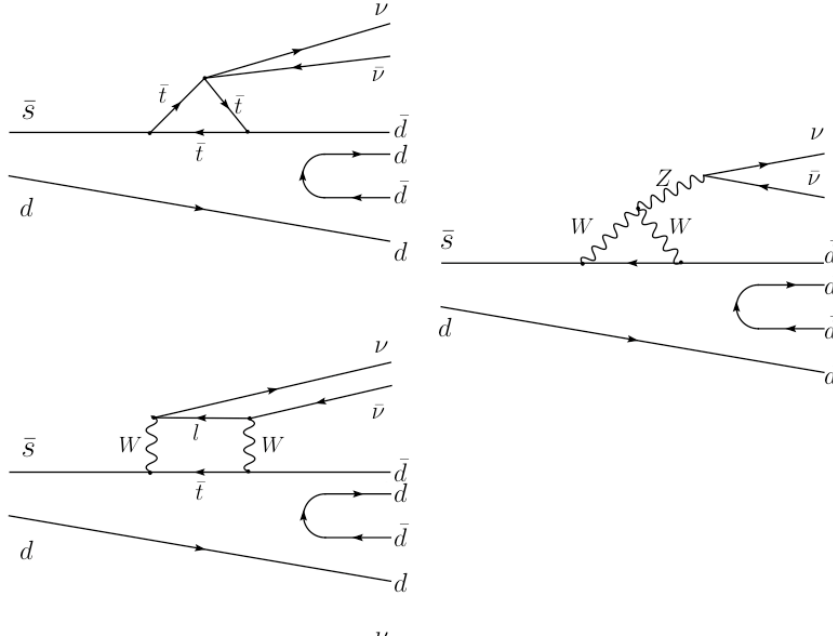


Figure 1.2: The short-ranged Feynman diagrams which contribute to  $K_L \rightarrow \pi^0 \pi^0 \nu \bar{\nu}$ .

The calculation of the decay rate depends on the matrix element for the hadronic current  $\bar{s}\gamma_\mu(1 - \gamma_5)d$  between the kaon and pion states. This matrix element can be extracted from analysis of the  $K_{\ell 4}$  decay using isospin symmetry. The analysis of  $K_{\ell 4}$  uses the form factors defined by [8]. The most recent prediction of the branching by [9] is:

$$\text{Br}(K_L \rightarrow \pi^0 \pi^0 \nu \bar{\nu}) = (1.4 \pm 0.4) \times 10^{-13}. \quad (1.9)$$

Determining the parameters of the CKM matrix is an important test of the Standard Model. The branching ratio of  $K_L \rightarrow \pi^0 \pi^0 \nu \bar{\nu}$  is proportional to  $\rho^2$ . The decay  $K_L \rightarrow \pi^0 \nu \bar{\nu}$  is proportional to  $\eta^2$ . Measurement of this branching ratio would allow us to specify the position of the vertex of the unitarity triangle purely through neutral decays of  $K_L$ . It is important to note that this is an extremely small branching ratio, two orders of magnitude smaller than  $K_L \rightarrow \pi^0 \nu \bar{\nu}$  and eight orders smaller than  $K_{e4}$ .

### 1.2.1 Kinematics of $K_L \rightarrow \pi^0 \pi^0 \nu \bar{\nu}$

The  $K_L \rightarrow \pi^0 \pi^0 \nu \bar{\nu}$  decay has a vector matrix element which causes the momentum to vary from what a pure phase space decay would produce.

The decay can be described as a two-body decay of the kaon into a dipion and dilepton. We can then treat the decay of the dipion and dilepton in their own center of mass systems. The decay can be described by five variables:

1.  $s_\pi = M_{\pi^0 \pi^0}^2$ , square of the center of mass energy of the dipion system.
2.  $s_\nu = M_{\nu \bar{\nu}}^2$ , square of the center of mass energy of the dilepton system.
3.  $\theta$ , angle of one of the  $\pi^0$  in the center of mass frame of the dilepton with respect to the direction of flight of the dilepton in the kaon rest frame.

4.  $\zeta$ , angle of the  $\bar{\nu}$  in the center of mass frame of the dipion with respect to the direction of flight of the dipion in the kaon rest frame.
5.  $\phi$ , the angle between the plane formed by the pions in the kaon rest frame and the corresponding plane formed by the neutrinos.

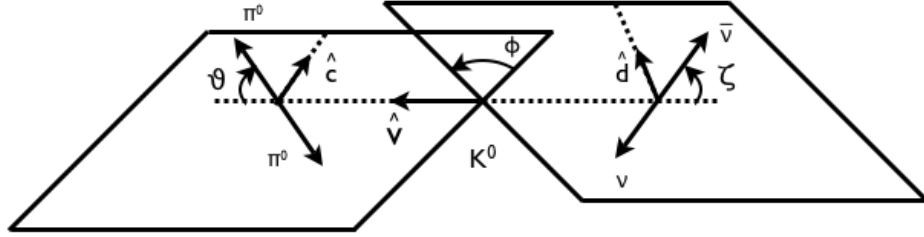


Figure 1.3: The  $K_L \rightarrow \pi^0 \pi^0 \nu \bar{\nu}$  decay into dipion and dilepton systems.

The labels of the four-momenta are  $p_1$  and  $p_2$  for the two pions and the neutrinos are  $p_\nu$  and  $p_{\bar{\nu}}$ . The three-momenta are in bold. The angular variables range  $0 \leq \theta \leq \pi$ ,  $0 \leq \zeta \leq \pi$ , and  $-\pi < \phi \leq \pi$ .  $\hat{v}$  is the unit vector along the direction of flight of the dipion. The projection of  $\mathbf{p}_1$  perpendicular to  $\hat{v}$  is  $\hat{c}$ .  $\hat{d}$  is an unit vector along the projection of  $\mathbf{p}_{\bar{\nu}}$  perpendicular to  $\hat{v}$ :

$$\cos \theta = \hat{v} \cdot \mathbf{p}_1 / |\mathbf{p}_1|, \quad (1.10)$$

$$\cos \zeta = \hat{v} \cdot \mathbf{p}_{\bar{\nu}} / |\mathbf{p}_{\bar{\nu}}|. \quad (1.11)$$

We introduce the following combinations of momentum and scalar products to sim-

plify the form factor:

$$P = p_1 + p_2, \quad (1.12)$$

$$L = p_{\bar{\nu}} + p_{\nu}, \quad (1.13)$$

$$Q = p_1 - p_2, \quad (1.14)$$

$$Q^2 = 4m_{\pi}^2 - s_{\pi}, \quad (1.15)$$

$$P \cdot L = \frac{1}{2}(m_K^2 - s_{\pi} - s_{\nu}), \quad (1.16)$$

$$X = [(P \cdot L)^2 - s_{\pi}s_{\nu}]^{1/2}. \quad (1.17)$$

### 1.2.2 $K_L \rightarrow \pi^0\pi^0\nu\bar{\nu}$ Form Factor

The distribution of the  $K_L \rightarrow \pi^0\pi^0\nu\bar{\nu}$  decay depends on the hadronic current  $\bar{s}\gamma_{\mu}(1 - \gamma_5)d$  between the kaon and the two pions. This can be extracted from measurements of the  $K_{\ell 4}$  decay using isospin symmetry. Isospin symmetry gives us the relationship:

$$\langle \pi^0\pi^0 | (\bar{s}d)_{V-A} | K^0 \rangle = \langle \pi^0\pi^0 | (\bar{s}u)_{V-A} | K^+ \rangle. \quad (1.18)$$

The decays  $K^{\pm} \rightarrow \pi\pi e^{\pm}\bar{\nu}$  in general have four terms in the matrix element. In the case of  $K^+ \rightarrow \pi^0\pi^0 e^+\nu_e$  and  $K_L \rightarrow \pi^0\pi^0\nu\bar{\nu}$  the fact that the pions of the final state are identical neutral pions means they cannot be in an  $I = 1$  state. The transition requirement of  $\delta I = \frac{1}{2}$  eliminates two of the terms. We can then use this to relate the matrix elements of  $K_L \rightarrow \pi^0\pi^0\nu\bar{\nu}$  to those of  $K^+ \rightarrow \pi^0\pi^0 e^+\nu_e$ . The matrix element for when the pions are in the  $I = 0$  state. The  $K_{\ell 4}$  decays have the matrix elements:

$$\langle \pi^+(p_1)\pi^-(p_2) | \bar{s}\gamma_{\mu}\gamma_5 d | K_L^0(k) \rangle = \frac{i}{M_K} \left[ P_{\mu}F + L_{\mu}G + (k - P)_{\mu}R \right]. \quad (1.19)$$

$$\langle \pi^+(p^+) \pi^-(p^-) | \bar{s} \gamma_\mu \gamma_5 u | K^+(k) \rangle = \frac{H}{M_K^3} \epsilon_{\mu\nu\alpha\beta} k^\nu (p^+ + p^-)^\alpha (p^+ - p^-)^\beta. \quad (1.20)$$

The isospin considerations above mean that the G and H terms are zero for  $K_L \rightarrow \pi^0 \pi^0 \nu \bar{\nu}$ . Additionally the R term is suppressed by the lepton mass, in this case the neutrino mass. This can obviously be ignored for our purposes.

The F term has the form:

$$F = (f_s + f'_s q^2 + O(q^4)) e^{i\delta_0^0}. \quad (1.21)$$

$$(1.22)$$

Here the pion momentum in the pion system reference frame is  $q^2 = ((p^+ + p^-)^2 - 4m_\pi^2)/4m_\pi^2$  and  $\delta_J^I$  are the the  $\pi - \pi$  scattering phase shifts. The phase shift  $\delta_0^0$  can be related to the scattering length. The constants  $f_s$  and  $f'_s$  have been measured in the  $K_{e4}$  decay [10],[11]:

$$f_s = 5.75 \pm 0.02 \pm 0.08, \quad (1.23)$$

$$f'_s = 1.06 \pm 0.10 \pm 0.40. \quad (1.24)$$

$$(1.25)$$

The differential decay rate for  $K_L \rightarrow \pi^0 \pi^0 \nu \bar{\nu}$  is given by:

$$d\Gamma_5 = \frac{G_F^5 V_{us}^2}{2^{12} \pi^6 m_K^5} X \sigma_\pi J_5(P^2, L^2, \theta, \zeta, \phi). \quad (1.26)$$

The function  $\sigma_\pi$  is defined as:

$$\sigma_\pi = (1 - 4m_\pi^2/s_\pi)^{1/2}. \quad (1.27)$$

Where the function  $J_5$  is:

$$J_5 = I_1 + I_2 \cos 2\theta. \quad (1.28)$$

Where the distribution functions  $I_1$  and  $I_2$  are:

$$I_1 = -I_2 = \frac{1}{8} \{2|XF|^2 \sin^2 \zeta\}. \quad (1.29)$$

The  $K_{\ell 4}$  and  $K_L \rightarrow \pi^+ \pi^- \nu \bar{\nu}$  decays have a much more complex form factor with nine distribution functions. The isospin values of the  $\pi^0$ 's and the fact that there are two identical particles simplify the structure considerably.

### 1.3 Supersymmetry

One of the leading theories for physics beyond the Standard Model is supersymmetry. In supersymmetric models, there is a symmetry between fermions and bosons. For every fermion there is a corresponding bosonic partner and for each boson there is a fermion. This symmetry does not exist at low energies and therefore must be broken in some manner. There are many models of supersymmetry breaking, but we are interested in models that “spontaneously” break supersymmetry.

The spontaneous breaking of any global symmetry results in a massless Nambu-Goldstone mode with the same quantum numbers as the symmetry generator. In the case of supersymmetry, the symmetry generator is fermionic resulting in a Nambu-Goldstone fermion, the goldstino. The exact nature of the goldstino depends on the specific model of supersymmetry. For example, in the case of supergravity theories, the superpartner of the graviton, the gravitino, absorbs the goldstino and thereby acquires a mass.

As the goldstino is part of a superfield it has a superpartner, the complex scalar field  $z = (S + iP)/\sqrt{2}$ . The real component,  $S$ , is the scalar sgoldstino and the imaginary part,  $P$ , is the pseudoscalar sgoldstino [12]. The masses of these two particles are model dependent and could be below a few GeV or a few MeV. Sgoldstinos are light in in some gravity mediated theories and gauge mediated models.

### 1.3.1 The Pseudoscalar Sgoldstino

We consider the case where parity is conserved in the interactions of the sgoldstino with quarks and gluons. The Lagrangian for the low energy interactions of  $P$  with quarks is written [13]:

$$\mathcal{L} = -P \cdot (h_{ij}^{(D)} \cdot \bar{d}_i i\gamma^5 d_j + h_{ij}^{(U)} \cdot \bar{u}_i i\gamma^5 u_j), \quad (1.30)$$

where

$$d_i = (d, s, b) \qquad u_i = (u, c, t), \quad (1.31)$$

$$h_{ij}^{(D)} = \frac{1}{\sqrt{2}} \frac{\tilde{m}_{D,ij}^{(LR)2}}{F}. \quad (1.32)$$

The energy scale of supersymmetry breaking is  $\sqrt{F}$ . Off-diagonal elements in the coupling matrices produce flavor changing and CP violating processes.

## 1.4 The $K_L \rightarrow \pi^0 \pi^0 P$ Decay

If the sgoldstino is light enough ( $m_P < m_{K_L} - 2m_{\pi^0}$ ) then the decay of a neutral kaon to  $2\pi^0$  and the pseudoscalar sgoldstino is a very interesting probe of the physics. This is not an unreasonable possibility as it arises in a variety of models.

The decay  $K^+ \rightarrow \pi^+\pi^0 P$  is forbidden at first order by the conservation of total isospin. The violation of isospin, chiral loops and derivative couplings in the effective meson-goldstino Lagrangian all allow the decay to occur.

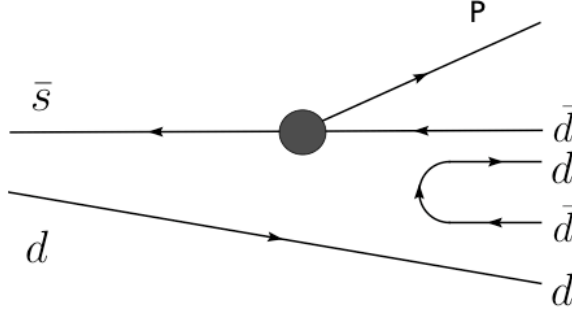


Figure 1.4: Diagram of the  $K_L \rightarrow \pi^0\pi^0 P$  decay.

#### 1.4.1 Branching Ratio and Supersymmetry Parameters

The branching ratio of  $K_L \rightarrow \pi^0\pi^0 P$  gives us direct means of determining some of the couplings between the sgoldstino and quarks. The partial width of the  $K_L$  for this decay is [13]:

$$\Gamma(K_L \rightarrow \pi^0\pi^0 P) = (\text{Re}h_{12}^{(D)})^2 \frac{M_K B_0^2}{1152\pi^3 f_\pi^2} \cdot F(M_P, m_\pi, m_K). \quad (1.33)$$

Here  $F(m_P, m_\pi, m_K)$  is a correction factor accounting for finite masses of pions and  $P$ ; at  $m_P \approx 0$  it is  $F \approx 0.3$ .  $B_0$  and  $f_\pi$  are related to the quark condensate,  $\langle 0|q\bar{q}|0\rangle = -\frac{1}{2}B_0 f_\pi^2$ . Then  $B_0 = M_K^2/(m_d + m_s) = 1.9\text{GeV}$  and  $f_\pi = 130\text{MeV}$ . This allows us to estimate the branching ratio as a function on the real component of the coupling to be:

$$\text{Br}(K_L \rightarrow \pi^0\pi^0 P) \sim 1.4 \times 10^{14} \cdot (\text{Re}h_{12}^{(D)})^2. \quad (1.34)$$

The coupling constants are constrained by the limits on the mass difference be-

tween  $K_L$  and  $K_S$  and requiring that the contribution to the  $\epsilon$  CP violation parameter in the kaon system is less than its measured value:

$$\Delta M_K \equiv M_{K_L^0} - M_{K_S^0} = [(\text{Re}h_{12}^{(D)})^2 - (\text{Im}h_{12}^{(D)})^2] \frac{B_0^2 f_K^2}{M_K(M_K^2 - M_P^2)}, \quad (1.35)$$

$$|(\text{Re}h_{12}^{(D)})^2 - (\text{Im}h_{12}^{(D)})^2| < 5 \times 10^{-15}, \quad (1.36)$$

$$\Delta M' = \text{Re}h_{12}^{(D)} \cdot \text{Im}h_{12}^{(D)} \cdot \frac{B_0^2 f_K^2}{M_K(M_K^2 - M_P^2)}, \quad (1.37)$$

$$|\text{Re}h_{12}^{(D)} \cdot \text{Im}h_{12}^{(D)}| < 1.5 \times 10^{-17}. \quad (1.38)$$

Depending on the phase of  $h_{12}^{(D)}$  bounds are set on the possible  $Br(K_L \rightarrow \pi^0 \pi^0 P)$  and other related kaon decays. If the real and imaginary components are approximately equal then:

$$Br(K_L \rightarrow \pi^0 \pi^0 P) \lesssim 1 \times 10^{-3}. \quad (1.39)$$

If the imaginary component is close to zero then there are no meaningful bounds on  $Br(K_L \rightarrow \pi^0 \pi^0 P)$ . In the case that the real component is close to zero then we have the bound:

$$Br(K_L \rightarrow \pi^0 \pi^0 P) \lesssim 1.5 \times 10^{-6}. \quad (1.40)$$

#### 1.4.2 Decay of the Sgoldstino

The sgoldstino can couple to a wide variety of particles with differing strengths. In this analysis, we assume that sgoldstino does not interact or decay to visible particles inside the detector.

## 1.5 Previous Limits

We briefly discuss other searches for the sgoldstino. The sgoldstino can potentially couple to a variety of different particles and has a wide range of possible mass. A variety of experiments and observations can set limits on different scenarios. These limits are summarized in Tables 1.5.2 and 1.2.

### 1.5.1 Other Kaon Experiments

The sgoldstino can appear in decays of the charged kaons. The branching ratio of the charged mode is estimated from chiral perturbation theory to be:

$$\text{Br}(K^- \rightarrow \pi^- \pi^0 P) \sim 8.5 \times 10^{10} \cdot |h_{12}^{(D)}|^2. \quad (1.41)$$

The mode  $K^- \rightarrow \pi^- \pi^0 P$  was searched for by the ISTRA+ experiment. ISTRA+ is located at the IHEP 70 GeV proton synchrotron U-70. ISTRA+ uses a negative unseparated beam of  $\approx 25\text{GeV}/c$ . A total of 713 million trigger events were recorded. Their primary background is the decay  $K_L \rightarrow \pi^0 \pi^0 \pi^-$  which limits their sensitivity in the region of  $M_P = M_{\pi^0}$ . They set a limit for at  $9 \times 10^{-6}$  for  $m_P$  between 0 and 200 MeV/ $c^2$  [1]. The limits for different masses are shown in Fig 1.5. The coupling of the sgoldstino to the charged kaon is suppressed by isospin conservation, so the bound on the coupling constant derived from this is significantly weaker than we can achieve with the neutral mode.

### 1.5.2 Astrophysical

A wide variety of astrophysical phenomena have been used to search for the axion. These studies can also be used to set limits on the interactions of the sgoldstino,

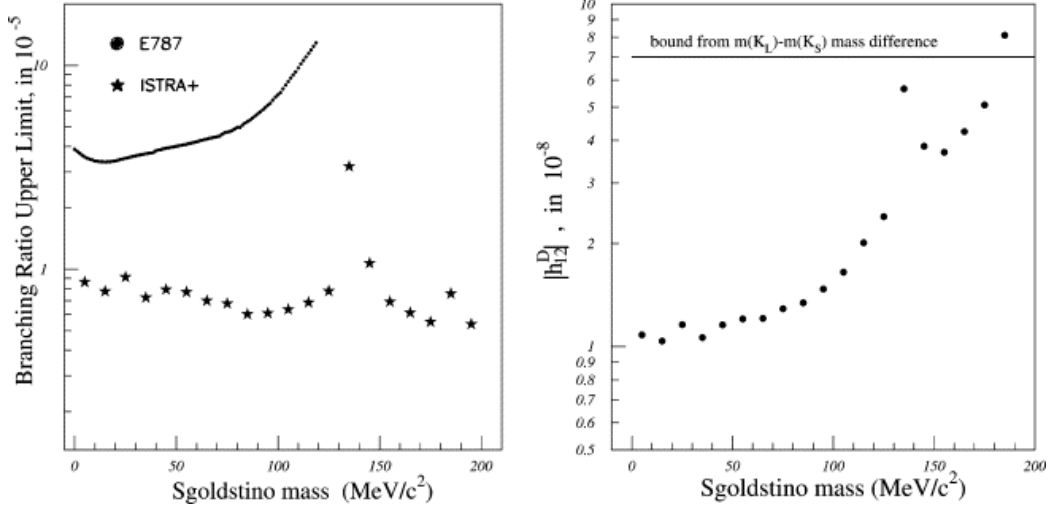


Figure 1.5: The 90% upper limit for the  $\text{Br}(K^- \rightarrow \pi^- \pi^0 P)$  versus sgoldstino mass compared with the E787 upper limit (left), the 90% CI upper limit for the  $|h_{12}^D|$  compared with the theoretical limit from  $K_L - K_S$  mass difference (right) [1]

either its coupling to photons or electrons [14]. A light pseudoscalar can be produced by a star through the Primakoff process,  $\gamma \rightarrow P$  in an external magnetic field. The inverse Primakoff process can be used to detect pseudoscalars in the “helioscope” method where a dipole magnet aimed at the Sun is used to change pseudoscalars into X-rays. This process can also occur in galactic magnetic fields, the absence of anomalous X-ray fluxes from 1987A from this provides the tightest bound on  $g_\gamma$ , but it applies for an unrealistically small  $m_P$ . Therefore, the helium-burning lifetime of Horizontal Branch Stars (HBS) in globular clusters provides the most sensitive probe of the supersymmetry breaking scale  $F$  for small  $m_P$ . These limits apply for masses of the sgoldstino significantly lower than the  $K_L \rightarrow \pi^0 \pi^0 P$  decay can probe. The upper mass from these searches is 10 MeV from SN1987a for the coupling of sgoldstinos to fermions.

Experiment	$m_P$	Coupling Constant	$\sqrt{F}$ , GeV	$m_{3/2}$
Helioscope	$\lesssim 0.03\text{eV}$	$g_\gamma < 6 \times 10^{-10}$	$> 0.5 \times 10^6$	$> 60\text{eV}$
SN1987A	$< 1\text{keV}$	$g_\gamma < 5.56 \times 10^{-10}$ or $> 10^{-2}$	$5 \times 10^5$ or $g_\gamma < 120$	$> 50\text{eV}$ or $< 3 \times 10^{-6}\text{eV}$
HBS	$< 10\text{keV}$	$g_\gamma < 6 \times 10^{-11}$	$> 4 \times 10^6$	$> 3.5\text{keV}$

Table 1.1: A summary of astrophysical limits on the sgoldstino.

### 1.5.3 Laboratory

Bounds on the sgoldstino can also be set by studying the behavior of laser beams. In a transverse magnetic field the production of real sgoldstinos would cause a rotation in the beam polarization. Additionally, the emission and absorption of virtual sgoldstinos would produce ellipticity in the beam. These effects have not been observed and this places limits on the  $g_\gamma$  coupling. Light pseudoscalars could also allow light to penetrate an optic shield. In this scenario light would convert to the sgoldstino through the Primakoff process and then reconvert on the other side. These limits apply for sgoldstino masses significantly below that which can be studied in kaon decays.

It is also possible to use reactor experiments to detect sgoldstinos. Here the sgoldstino would be produced by an isoscalar transition and then the sgoldstino detected by means of its decay products. Again this technique probes mass values significantly below what  $K_L \rightarrow \pi^0 \pi^0 P$  can probe. These are limited to masses less than 1.5 MeV.

### 1.5.4 Evidence for a pseudoscalar

The HyperCP collaboration has found evidence for the existence of a new particle of mass  $214.3 \pm 0.5 \text{MeV}/c^2$  [15] whose properties are consistent with a pseudoscalar particle [16]. They studied the decay  $\Sigma^+ \rightarrow p\mu^+\mu^-$ . In the Standard Model the ratio

Experiment	$m_P$	Coupling Constant	$\sqrt{F}$ , GeV	$m_{3/2}$
Laser	$< 10^{-3}\text{eV}$	$g_\gamma < 3.6 \times 10^{-7}$	$> 2.0 \times 10^4$	$> 93\text{MeV}$
$\gamma$ -regeneration	$< 10^{-3}\text{eV}$	$g_\gamma < 6.7 \times 10^{-7}$	$> 1.5 \times 10^4$	$> 50\text{MeV}$
NOMAD	$\lesssim 40\text{eV}$	$g_\gamma < 6.7 \times 10^{-4}$	$> 970$	$> 0.22$
Reactor $e^+e^-$	$< 1.5\text{MeV}$	$g_N^{(0)} \cdot \text{Br}_{(P \rightarrow X)}^{1/2} \lesssim$	$\gtrsim \frac{3 \times 10^5}{\text{Br}_{(P \rightarrow X)}^{-1/4}}$	$\gtrsim \frac{25\text{eV}}{\text{Br}_{(P \rightarrow X)}^{1/2}}$
Final State		$7 \times 10^{-10}$		
Reactor $\gamma\gamma$	$< 1\text{MeV}$	$g_N^{(0)} \cdot \text{Br}_{(P \rightarrow X)}^{1/2} \lesssim$	$\gtrsim \frac{9 \times 10^3}{\text{Br}_{(P \rightarrow X)}^{-1/4}}$	$\gtrsim \frac{20\text{MeV}}{\text{Br}_{(P \rightarrow X)}^{1/2}}$
Final State		$8 \times 10^{-7}$		

Table 1.2: Limits on pseudoscalar sgoldstino couplings.

is of  $\Sigma^+ \rightarrow p\mu^+\mu^-$  to  $\Sigma^+ \rightarrow pe^+e^-$  is bounded:

$$\frac{1}{120} \gtrsim \frac{\Gamma(\Sigma^+ \rightarrow p\mu^+\mu^-)}{\Gamma(\Sigma^+ \rightarrow pe^+e^-)} \gtrsim \frac{1}{1210}. \quad (1.42)$$

A limit has been set for the branching ratio of  $\Sigma^+ \rightarrow pe^+e^-$  as  $< 7 \times 10^{-6}$ .

The HyperCP group observed three events which allowed them to set a branching ratio of  $[8.6_{-5.4}^{6.6}(\text{stat}) \pm 5.5(\text{syst})] \times 10^{-8}$ . The invariant mass of the  $\mu^+\mu^-$  of these events were grouped near 214 MeV. This suggests that there is intermediate state which when fit for has a mass of  $214.3 \pm 0.5$  MeV. This intermediate state is allowed by existing constraints to be a pseudoscalar or axial-vector particle.

## CHAPTER 2

### E391A EXPERIMENT

In this chapter I will describe the components of the E391a experiment. There are two major components to the experiment, the E391a beamline, which produces a well collimated beam of neutral kaons for study, and the E391a detector to measure the decays of interest.

#### 2.1 The E391a Beam

The E391a beam line was designed with the search for  $K_L \rightarrow \pi^0 \nu \bar{\nu}$  as the primary goal. Of primary importance is making a narrow, well collimated beam to minimize the transverse momentum of the kaon. The second important consideration is the eliminating as much as possible the beam halo.

The beam is produced by 12 GeV protons striking a platinum target. The target is 60 mm thick which corresponds to 0.68 interaction lengths and 8 mm in diameter. The beam line is 10m long to reduce the number of neutral hyperons in the beam. There are a series of six collimators made of 5 cm thick tungsten disks arranged as shown in Figure 3.1. After the first collimator there is are lead and beryllium absorbers. During standard physics running the lead absorber was inserted in the beam to increase the kaon to neutron ratio.

The regions of the beam after collimation are described by the lines in the schematic diagram.

- A. The edge of the 2 mrad beam core. It is defined by the surfaces of collimators C2 and C3.

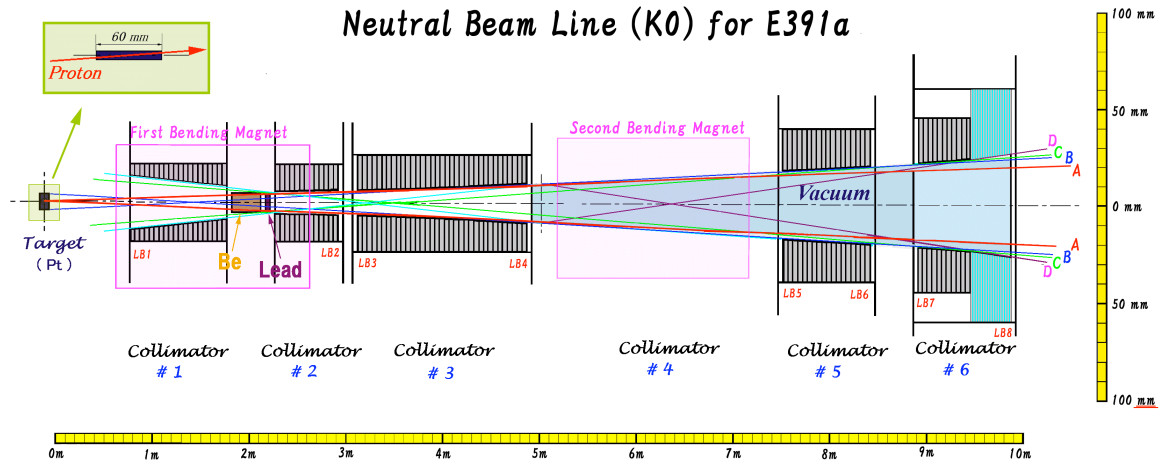


Figure 2.1: The e391a neutral beamline.

- B. Connects the edge of the target and the end of C3 and shows the penumbra due to the size of the target.
- C. Connects the beginning of C2 and P6. This is the limit of secondaries produced by the lead and beryllium absorbers.
- D. The outer edge of the beam. It is the boundary for secondaries produced by interaction with the collimators and for particles scattered by air in the beam line. The line connects the end of C3 and P6.

### 2.1.1 Beam Profile

The beam profile was measured in a series of beam-survey experiments in April and December 2000 and December 2001 [2]. The profiles of photons, neutrons and charged particles were measured separately using a counter telescope. The telescope consisted of a 1 cm-thick plastic scintillator, a 6 cm-thick plastic scintillator, and a lead scintil-

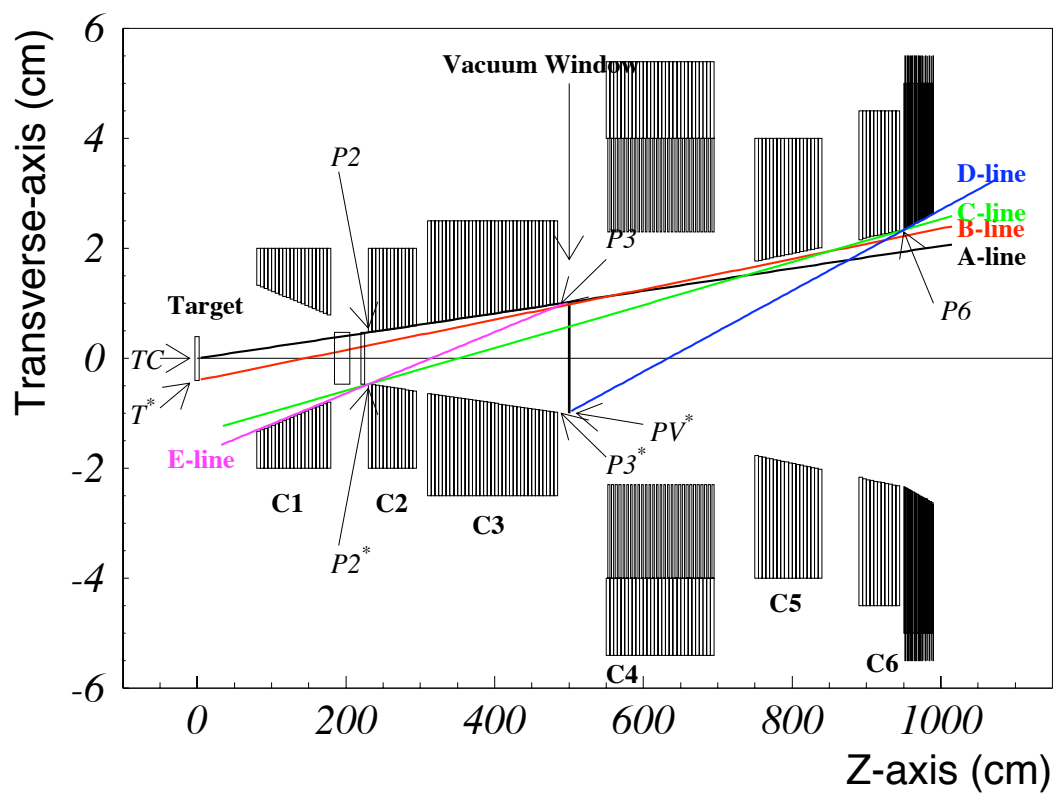


Figure 2.2: Schematic diagram of e391a collimation system.

lator sandwich counter. The sandwich counter had 15 layers of 1 mm lead and 5 mm thick scintillator for a total thickness of 9 cm or 2.85 radiation lengths. The counters had a cross section of  $4 \times 5\text{cm}^2$ . The front face of the telescope was located 1.7 m downstream of C6 and an X-Y stage was used to move the telescope.

Charged particles were identified as a coincidence of the two scintillator counters. Photons were identified as a signal in the sandwich counter vetoed by the first counter. Signals in the second scintillator without signals in the first scintillator were identified as neutrons.

## 2.2 Detector Overview

The E391a detector consists of a hermetic photon veto system and a CsI crystal calorimeter. Most of the detector is enclosed in a steel vacuum vessel, excluding CC05 - CC07 and the Back-Anti. The detector consists of the CsI Array which is used to detect the photons produced by the decay modes and a variety of other detectors which are either photon or charged vetoes. The photon vetoes are the Main and Front Barrels, a series of collar counters located close to the beamline, and finally the Back-Anti which is located directly in the beam as the farthest downstream detector. The charged vetoes are the Charge Veto which is front of the CsI Array, the Barrel Charge Veto which is an inner layer of the Main Barrel, and the Beam Hole Charge Veto which sits in front of the Back-Anti.

In the following sections the detector's energy spectrums are compared between data and Monte Carlo. The data sample is four cluster events taken from the physics trigger (Section 3.2.3). The Monte Carlo sample is  $K_L \rightarrow \pi^0\pi^0$  and  $K_L \rightarrow \pi^0\pi^0\pi^0$  events which is normalized to the data through the size of the  $K_L \rightarrow \pi^0\pi^0$  signal peak (Section 4.2).

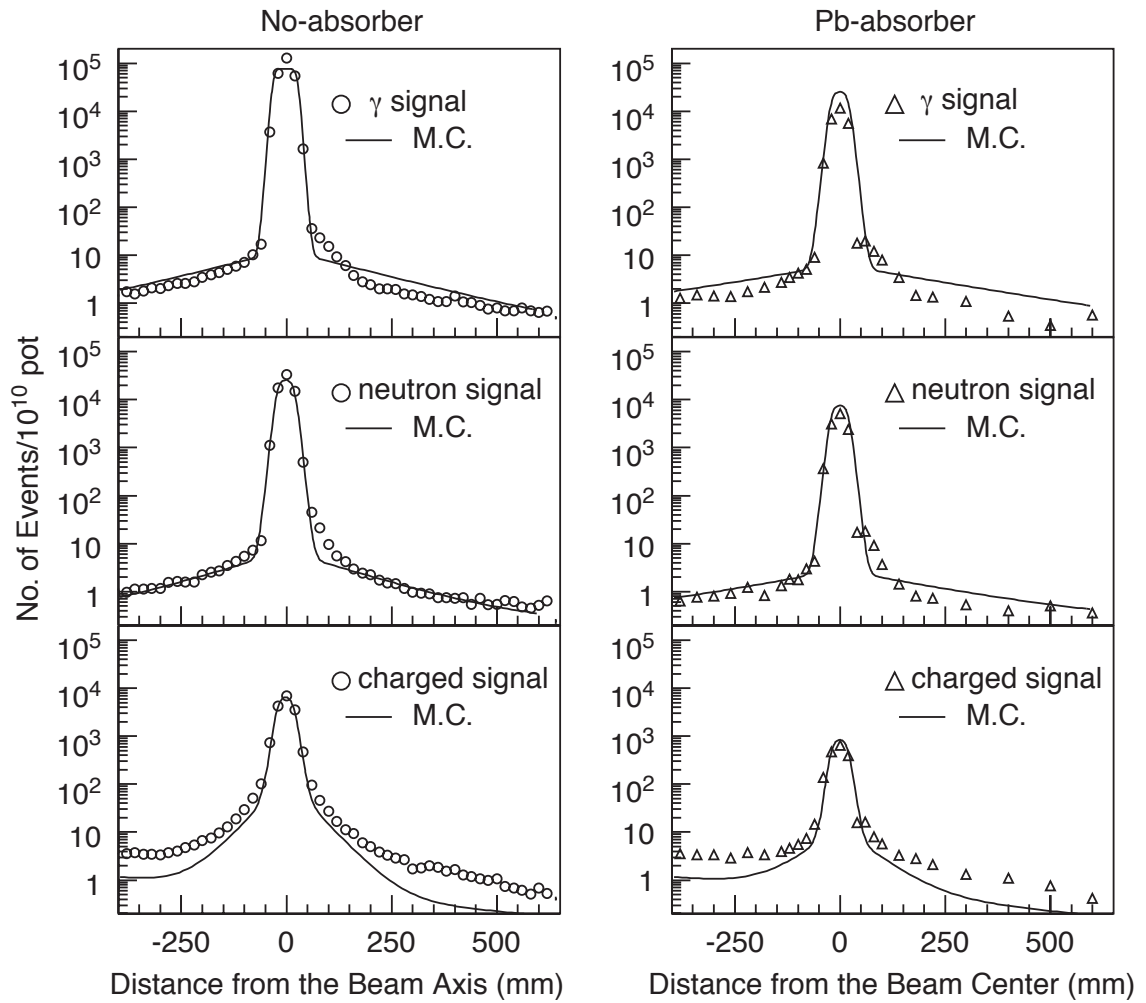


Figure 2.3: Measured beam profiles. The left-side figures are the case with no absorber in the beam. The figures on the right are with the Pb-absorber inserted. Solid lines are the results of Monte Carlo simulation. [2]

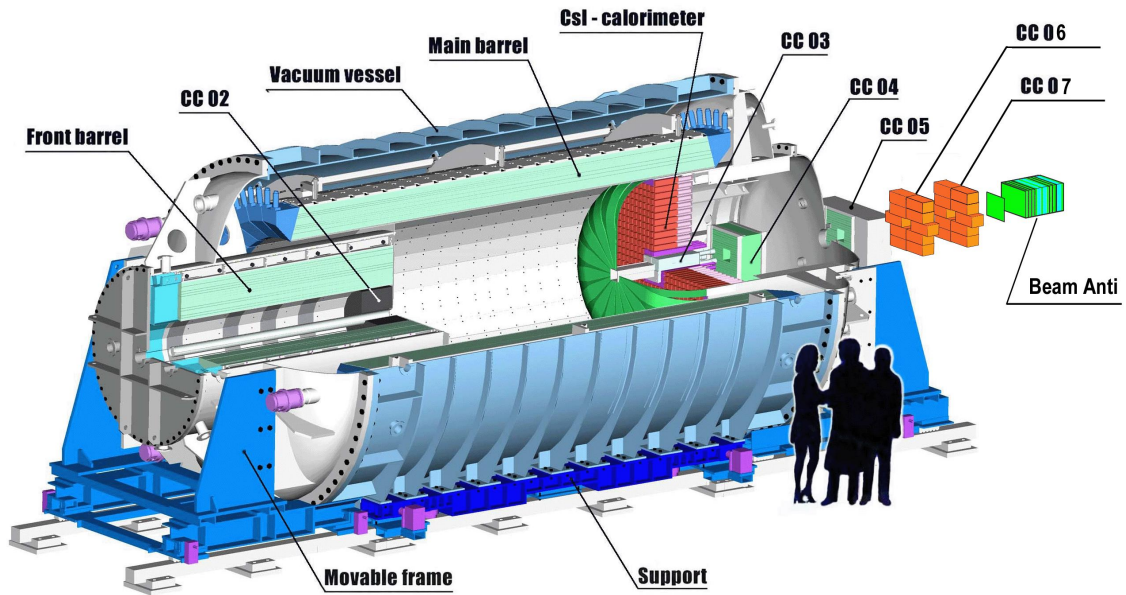


Figure 2.4: The e391a detector.

### 2.2.1 Vacuum System

To reduce beam interactions which could produce background the E391a detector is kept in vacuum [17]. There are two different regions of vacuum maintained. Region 1, also called the low vacuum region, is maintained at less than 1 Pa ( $10^{-5}$  atmospheres) during operation. The high vacuum region, region 2, is at a pressure of less than  $10^{-4}$  Pa ( $10^{-9}$  atmospheres) during operation. The high vacuum region contains the fiducial decay region inside the main barrel. The two regions are separated by a thin multi-layer vacuum membrane of  $190\ \mu\text{m}$  thickness or  $4 \times 10^{-4} X_0$ . The membrane consists of two layers of  $80\ \mu\text{m}$  low-density polyethylene, an aluminized EVAL film of  $15\ \mu\text{m}$ , and a  $15\ \mu\text{m}$  film of nylon.

Unfortunately, this membrane is a major background source. The measures taken to secure the membrane were not sufficient and the membrane drooped into the beam line. Fig. 2.6 shows the membrane relative to the beam hole. There it served as

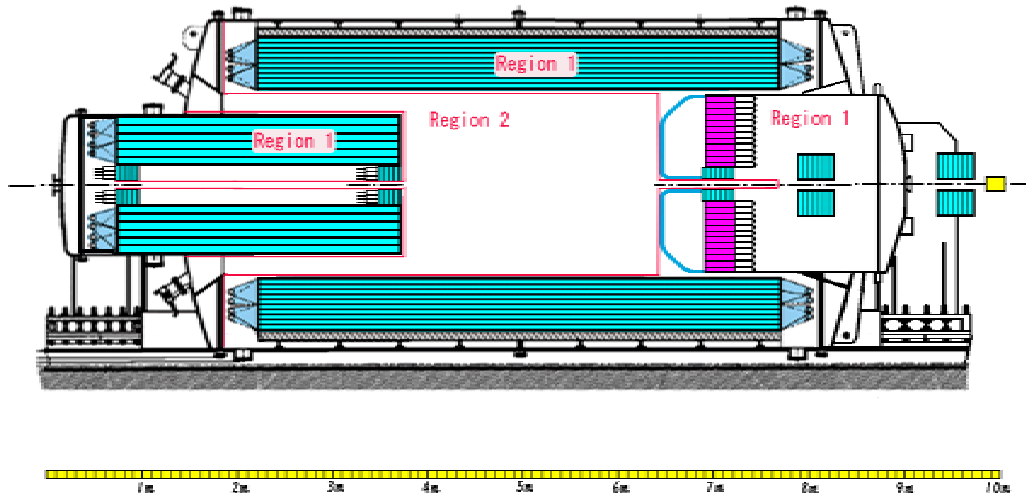


Figure 2.5: The E391a detector with the locations of the different vacuum regions indicated. Region 1 is at  $< 1$  Pa and region 2 is at  $< 10^{-4}$  Pa. They are separated by a thin vacuum membrane

target for interactions of neutrons in the beam core. This problem has been fixed for the later runs of the experiment.

## 2.3 Collar Counters

The collar counters are a series of electromagnetic calorimeters close to the beamline. There are six collars, two through seven. Initial plans called for a first collar counter, but simulation studies indicated that it did not significantly reduce photon inefficiency or background rate, so it was removed at the design stage.

### 2.3.1 Collar Counter 2

Collar Counter 2 is located inside the downstream end of the Front Barrel. It is a lead-scintillator sandwich Shashlyck calorimeter. A Shashlyck calorimeter is distinguished by its use of optical fibers running perpendicular to the the lead and scintillator plates to pass the scintillation light to the photo-tubes. CC02 is divided into eight pentagon

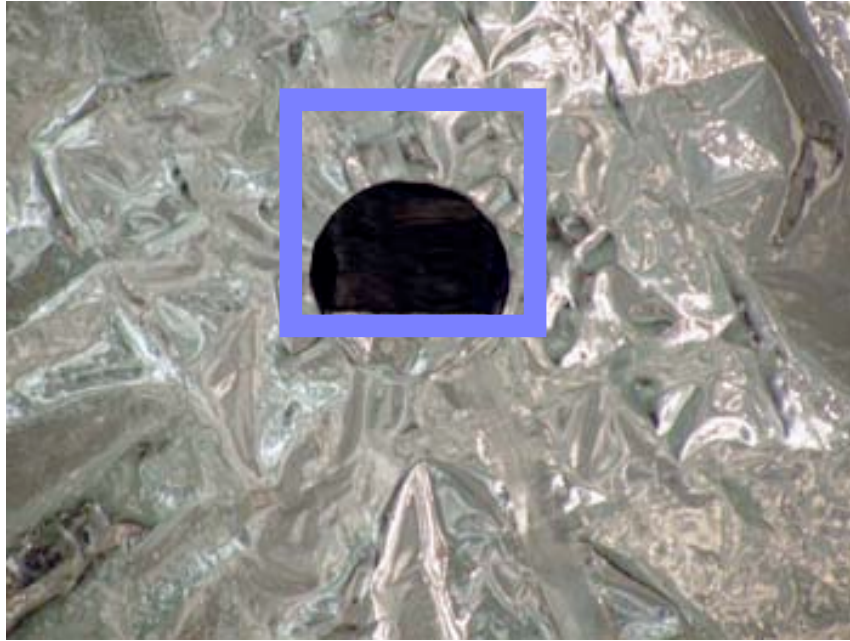


Figure 2.6: The vacuum membrane hanging in the beam line. The blue box indicates the beam hole in the center of CC03.

shaped segments as shown in Fig. 2.7. The outer diameter of CC02 is 60.8 cm and the inner diameter is 12.7 cm.

There are 45 .5 cm scintillator plates. Two thicknesses of lead plates are used, 1 mm at the upstream and downstream sides and 2 mm lead in the center. There are a total of 14 1 mm pieces and 29 2 mm pieces. Each piece of lead is has a 0.375 mm layer of brass on each side for support and ease of machining. For structural support there are also 1.5 cm aluminum plates at the ends of the detector with a single scintillator plate outside of them. CC02 is in total  $13.8 X_0$  thick.

Each plate has 296 holes which are of 1.5 mm diameter to feed through the optical fibers. The holes are regularly spaced with a 1 cm separation. The optical fibers are wavelength shifting fibers that shift the scintillation light into to green light. The fibers from each section are bundled together and fed to a single PMT. The PMT's are located at the front of the Front Barrel which requires the optical fiber to be 2.8

m long. This causes an attenuation of the light signal by approximately a factor of two. A comparison of the energy deposit in CC02 in data and Monte Carlo is shown in Fig. 2.8.

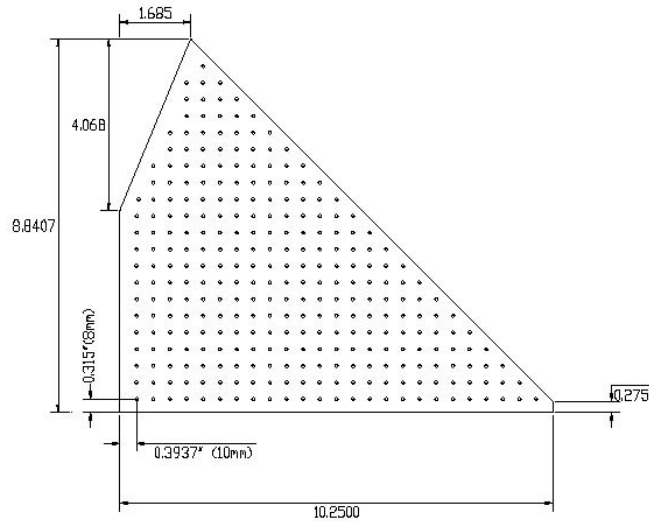


Figure 2.7: Cross section of one of the CC02 modules

### 2.3.2 Collar Counter 3

Collar Counter 3 is a tungsten scintillator sandwich calorimeter located inside the CsI array. The plates are aligned parallel to the beam axis in order to veto decays inside the beam hole. CC03 is  $25 \times 25$  cm with a beam hole of  $12 \times 12$  cm. Six rectangular modules make up CC03. The detector is  $5.2 X_0$  thick. A comparison of the energy deposit in CC03 in data and Monte Carlo is shown in Fig. 2.9.

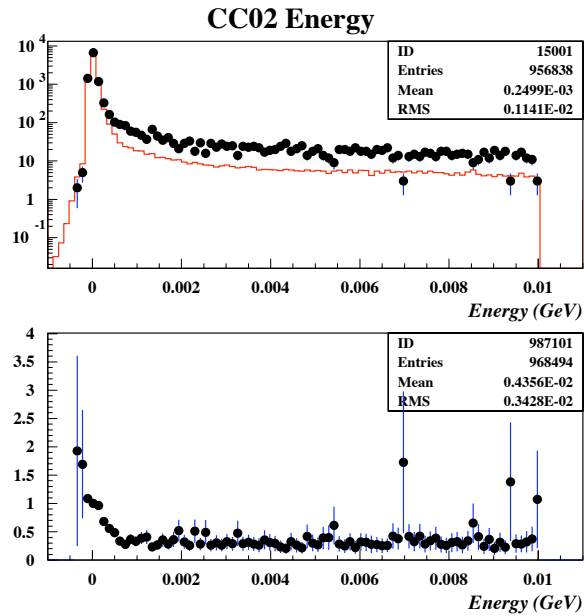


Figure 2.8: Energy deposit in CC02 in GeV. Data is represented by the black dots and Monte Carlo by the red line. Samples are normalized by the maximum bin. Lower plot is ratio of Monte Carlo to data.

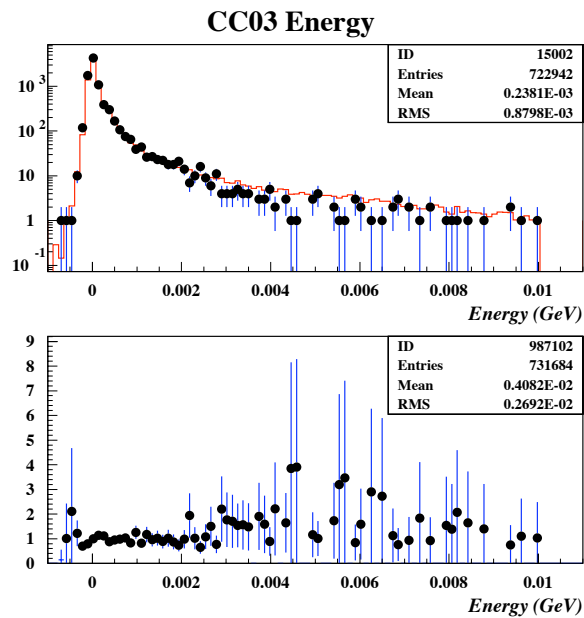


Figure 2.9: Energy deposit in CC03 in GeV. Data is represented by the black dots and Monte Carlo by the red line. Samples are normalized by the maximum bin. Lower plot is ratio of Monte Carlo to data.

### 2.3.3 Collar Counters 4 & 5

Collar Counter 4 and 5 are lead-scintillator sandwich calorimeters located downstream of the CsI array. They serve to detect photons which pass through the beamhole. Both detectors are  $40 \times 40$  cm squares with  $6.2 \times 6.2$  cm beam holes. A diagram of the CC04 cross-section is shown in Fig. 2.10.

CC04 consists of 32 5 mm scintillator plates and 32 2 mm lead plates serving as a calorimeter. This totals 11.8 radiation lengths. Two scintillator plates are placed on the upstream end to serve as a charge veto. The scintillation light is read out through wave length shifting optical fibers. Two PMT's read out the charge veto layers and two read out the calorimeter layers.

The design of CC05 is similar, but with only 30 layers in the calorimeter and the charged veto is on the downstream end of the detector to protect against backplash from the detectors downstream of it. A comparison of the energy deposit in CC05 in data and Monte Carlo is shown in Fig. 2.11.

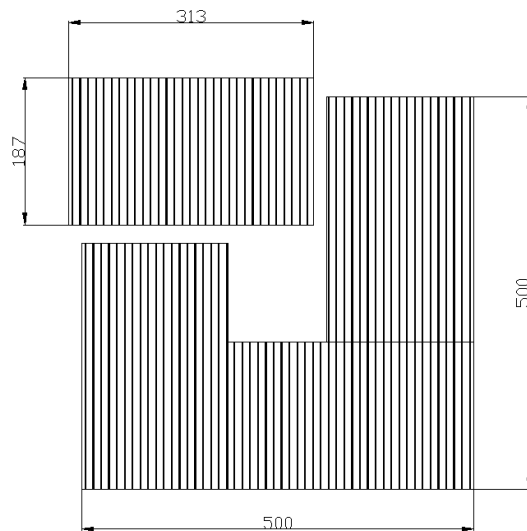


Figure 2.10: Diagram of CC04

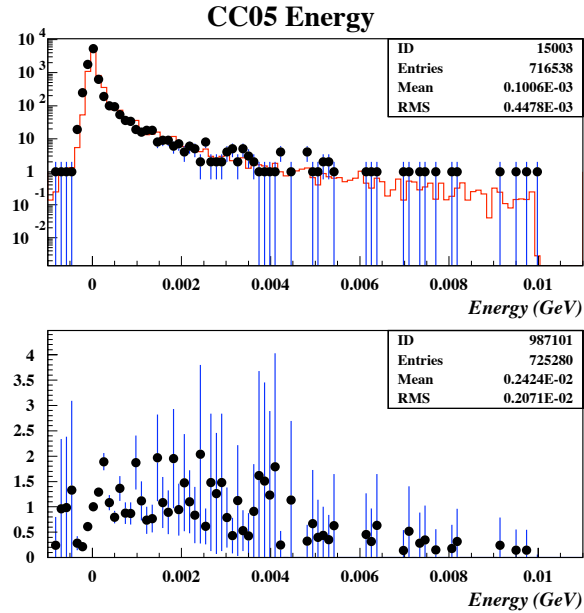


Figure 2.11: Energy deposit in CC05 in GeV. Data is represented by the black dots and Monte Carlo by the red line. Samples are normalized by the maximum bin. Lower plot is ratio of Monte Carlo to data.

### 2.3.4 Collar Counter 6 & 7

Collar counters 6 and 7 are each made of 10 lead glass blocks. They are located in upstream of the BA detector. Each block is  $15 \times 15 \times 30\text{cm}^3$ . The detectors are 5 blocks high aligned so that the 30 cm dimension is perpendicular to the beam. The primary purpose of CC06 is to further protect against photons escaping through the beamhole. CC07 is used to block splashback from the BA. Neither CC06 or CC07 was used as a veto in this analysis.

### 2.3.5 Calibration of Collar Counters

The collar counters, except CC03, were calibrated using beamline muons. This data was taken during special muon runs with the beam shutter closed. Events were triggered by coincidence of other collar counters.

CC03 is calibrated by cosmic ray muons using the procedure that is used for the CsI array.

## 2.4 Main Barrel

The largest element of the photon veto system is the Main Barrel. It is a lead-scintillator sandwich detector. It is divided into 32 sections forming a cylinder enclosing the fiducial decay region. It is 5.5 m long and has an inner diameter of 2.0 m. There are 45 5 mm layers of scintillator and 45 layers of lead. The lead consists of 15 layers of 1 mm thick and 30 layers of 2 mm thick plates. The detector is 14 radiation lengths thick. Wavelength shifting optical fibers run parallel to the scintillator plates for the length of the barrel. The fibers are read out on both the upstream and downstream end by inner and outer photo-multiplier tubes.

### 2.4.1 Calibration

The Main Barrel was calibrated using cosmic ray muons. These events were selected online by a coincidence of modules on the opposite side of the barrel. The path of the cosmic ray was reconstructed using timing information. Since the Main Barrel is read out from both ends, the time difference between the two PMT's can be used to determine the z position of the cosmic ray in each module. The speed of propagation of the signal was measured by using a radioactive source.

A track can be determined by minimizing the deviation of these points from the track as shown in Figs. 2.12 and 2.13. We introduce a correction to the timing,  $T_0$  for each module by finding the difference mean difference between the fit z position and the z position directly from the TDC value. After determining  $T_0$ , we refit the tracks. We then can use the track length to fit the charge produced by the minimum

ionizing particles by normalizing the charge measured by the ADC. A comparison of the energy deposit in the Main Barrel in data and Monte Carlo is shown in Fig. 2.14.

$$V = 17.7 \frac{\text{cm}}{\text{ns}} \quad \text{Speed of propagation in module} \quad (2.1)$$

$$z = a \cdot r + b \quad \text{Cosmic Ray Track} \quad (2.2)$$

$$S = \frac{1}{4} \sum (z_i - a \cdot r_i + b)^2 \quad \text{Deviation from track} \quad (2.3)$$

$$T_0 = 2 \cdot (z_{fit} - z_{tdc})/V \quad \text{Time correction for each module} \quad (2.4)$$

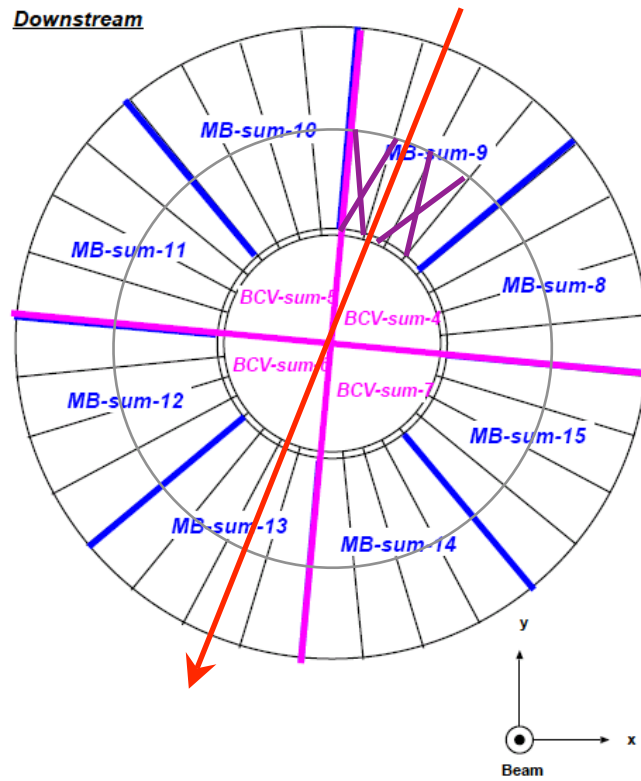


Figure 2.12: Schematic diagram of calibration procedure for the Main Barrel.

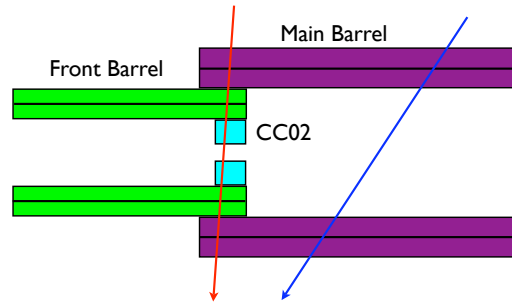


Figure 2.13: Schematic diagram of calibration cosmic muons for Front Barrel(red) and Main Barrel(blue).

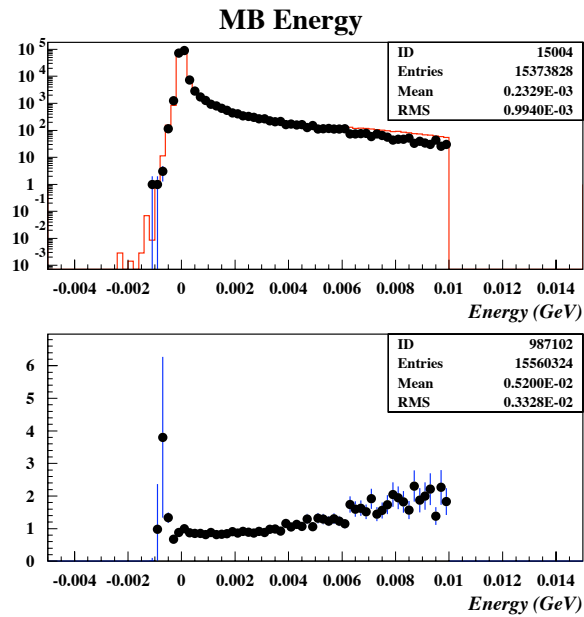


Figure 2.14: Energy deposit in Main Barrel in GeV. Data is represented by the black dots and Monte Carlo by the red line. Samples are normalized by the maximum bin. Lower plot is ratio of Monte Carlo to data.

## 2.5 Front Barrel

The Front Barrel is a lead-scintillator sandwich calorimeter located upstream of the Main Barrel. It has 16 sections which are read out to inner and outer PMT's located upstream of the detector. The Front Barrel is 2.75 m long and has an inner diameter of 60 cm. Each module has 59 layers of 5 mm thick scintillator and 59 layers of 1.5 mm thick lead. The detector is 26.5 radiation lengths thick. CC02 is located inside the downstream end of the Front Barrel.

### *2.5.1 Calibration*

The calibration of the Front Barrel uses the tracks determined by the Main Barrel. Tracks are selected by requiring energy deposit in CC02. The charge deposit is normalized by the path length in the Front Barrel and fit by a Landau distribution. A comparison of the energy deposit in the Front Barrel in data and Monte Carlo is shown in Fig. 2.15.

## 2.6 Barrel Charge Veto

To help veto charged particles which strike the Main Barrel, there is an inner layer of scintillator before any lead. This layer is separately read out as the Barrel Charge Veto.

### *2.6.1 Calibration*

The Barrel Charge Veto is calibrated using cosmic rays. The events are selected for vertical tracks located at the middle of the Main Barrel.

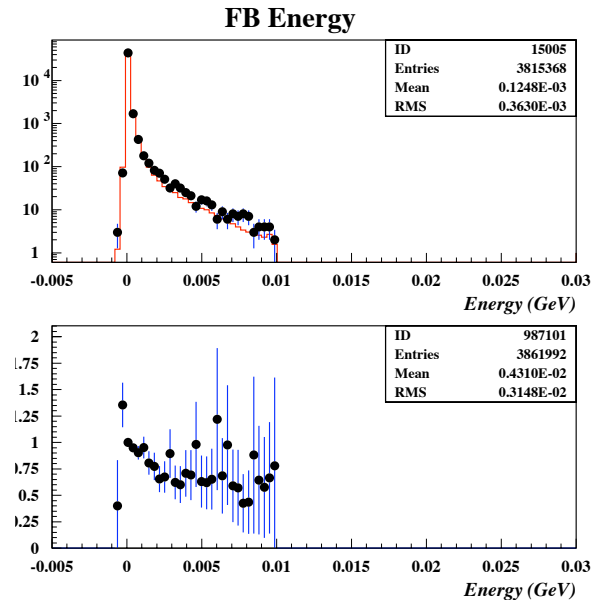


Figure 2.15: Energy deposit in Front Barrel in GeV. Data is represented by the black dots and Monte Carlo by the red line. Samples are normalized by the maximum bin. Lower plot is ratio of Monte Carlo to data.

## 2.7 Back-Anti

The Back-Anti (BA) is the final detector element. It is located 4.4 m downstream of the CsI face. It consists of alternating lead-scintillator sandwich and quartz crystal layers. The principle challenge to the BA is properly vetoing photons while avoiding over-vetoing from beam related accidentals. This is the motivation for including the two different detection methods in the detector. One of the most important means of improving photon-neutron discrimination is longitudinal segmentation. The electromagnetic shower generated by the interaction of a photon has a smooth profile with small fluctuations. A hadronic shower initiated by a neutron has large fluctuations.

The Back-Anti consists of 6 scintillator-lead modules and 6 quartz modules. The scintillator-lead modules are made of six layers of 1 cm scintillator and six layers of 2.54 mm lead. Each scintillator layer is read out separately. The quartz modules are made of 2 layers of 0.7 cm thick quartz blocks which are stacked 4 blocks. Each

quartz block is read out by an individual PMT.

Our back-anti has 3 separate components: a cut on the shower shape, a cut on the Cerenkov light produced by the quartz, and a timing cut. The shower shape cut is based on the energy deposit in the scintillator layers. Events are cut if the ratio of the energy deposit in the last scintillator modules to the total energy deposit in the scintillator is below a maximum value.

$$\frac{E_{\text{scintillator module 5}}}{E_{\text{total scintillator}}} < 0.9 \quad (2.5)$$

$$\frac{E_{\text{scintillator module 4}} + E_{\text{scintillator module 5}}}{E_{\text{total scintillator}}} < 0.95 \quad (2.6)$$

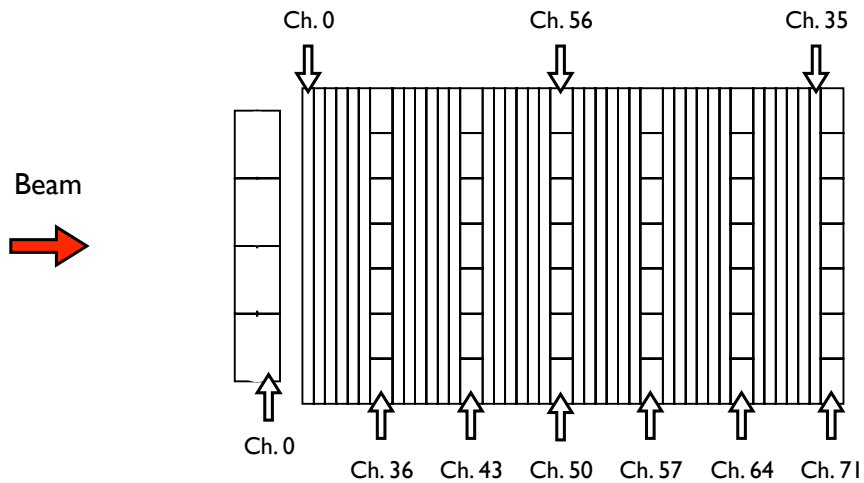


Figure 2.16: Diagram of the Back-Anti detector and the Beam Hole Charged Veto.

The Cerenkov cut is applied if there is more energy deposited in the quartz layer than half the energy deposited by a minimum ionizing particle. The timing cut is based on the number of scintillator channels which have hits on time. If more than 3 channels have hits in a timing window four sigma wide around the time peak and the energy in the scintillator is above an energy threshold.

## 2.7.1 Calibration

Pedestals were stable to a few percent over the course of Run I. The primary cause of pedestal instability were discrete hardware related changes which showed significant jumps in the pedestal values.

Calibration of the Back-Anti was done using beam line muons. The beam shutter was closed to produce a muon beam. The trigger was either a coincidence between the first and last scintillator layers or a coincidence between the last scintillator layer of the BA and a BHCV channel. The energy deposit in the scintillator panels was fit with a Landau function and measured in terms of MeV. In the quartz layers, we fit with a Gaussian function and calibrate in terms of the energy deposit left by a minimum ionizing particle.

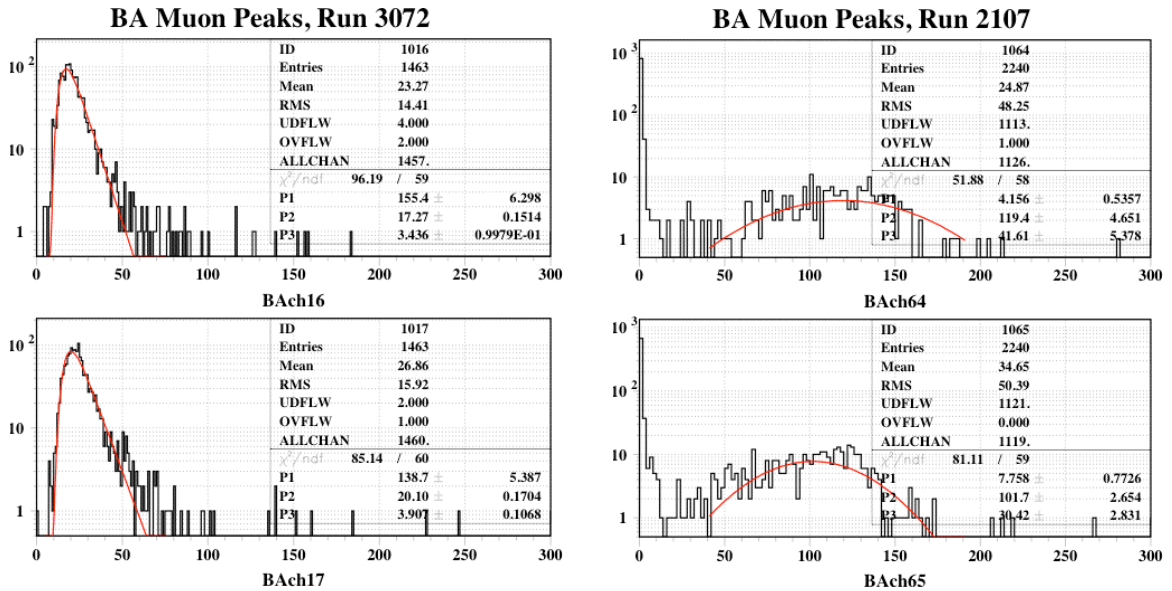


Figure 2.17: Typical BA muon peaks for scintillator layers (left) and quartz layers (right). The scintillator layers are fit with a Landau function and the quartz layers are fit with a Gaussian.

## 2.8 Charge Veto

To prevent misidentification of charged particles hitting the CsI as photons, there is the Charge Veto in front of the CsI. The Charge Veto consists of 32 curved scintillator pieces. They are secured at the outer edge of the CsI array and are bent around in front of the CsI where they meet around the beam hole. They are supported around the beam hole with an aluminum square tube that is attached to the CsI array structure. The panels of the Charge Veto overlap in front of the CsI, so there are two chances to detect the charged particle. There are four more scintillator panels on the inside of the beam hole to protect from charged particles produced by decays in the beam hole region.

The Charge Veto panels are read out by use of a light guide connecting them to the PMT. Each channel is read out by one PMT. Each panel is 6 mm thick. The total length of the panels in front of the CsI is 234 cm.

### *2.8.1 Calibration*

The Charge Veto is calibrated by beam muons. By requiring single block clusters in the CsI array we can identify which panel the muon passed through. One significant issue is the length of the scintillator panels which produces significant attenuation and position dependence in the signal.

## 2.9 CsI Array

The CsI array consists of 576 undoped cesium iodide crystals. There are 496  $7 \times 7 \times 30\text{cm}^3$  crystals. We call these the KEK crystals. At the outer edge of the array we have 56 crystals which have been cut into trapezoidal shapes which are called the

deformed crystals. Around the beamhold are 24  $5 \times 5 \times 50\text{cm}^3$  crystals which were borrowed from the KTeV collaboration and are therefore called the KTeV crystals. Inside the KTeV crystals is CC03. The CsI is arranged in to circular shape with a radius of approximately 94 cm [18].

The energy resolution of a 25 KEK crystal sample was measured in a separate beam test using a positron test beam. An example of the measurement is shown in Fig 2.18 The value was approximately [19]

$$\frac{\sigma_E}{E(\text{GeV})} \simeq \frac{1\%}{\sqrt{E(\text{GeV})}} \oplus 1\%. \quad (2.7)$$

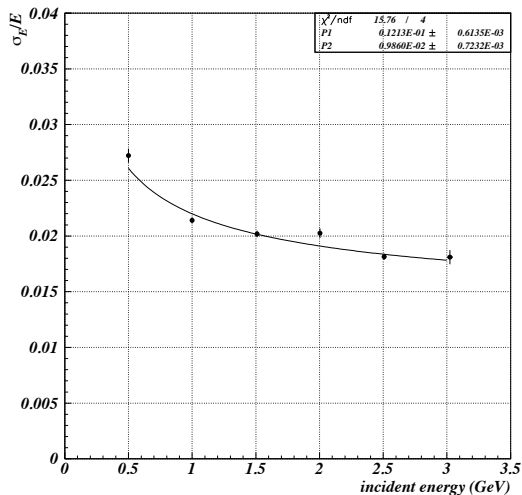


Figure 2.18: The energy resolution of a CsI crystal as a function of incident energy measured in the positron beam test.

### 2.9.1 Calibration Methods

Multiple methods were used to calibrate the CsI array. At the end of the run, we placed an aluminum plate inside the fiducial decay region to serve as a  $\pi^0$  source. With the  $\pi^0$  decay vertex known, we can use the reconstruct its mass and tune the calibration to match the known value. This allows us to set an absolute energy scale

from photons with a experimental signature similar to the physics decays. Additionally, we use cosmic ray muons passing through the CsI array to measure changes in the CsI array during the run. Muons from the beamline which are identified using the Charged Veto can also be used for calibration. Finally, the  $K_L \rightarrow \pi^0 \pi^0 \pi^0$  decay has enough kinematic constraints that it can be fully reconstructed with information from only five of the final state photons.

### 2.9.2 Cosmic Calibration

The first calibration method is the use of cosmic ray muons. For the data in this analysis, the cosmic rays were taken in dedicated cosmic ray runs. The trigger conditions for a cosmic ray event was four hardware clusters with a deposited energy above 40 MeV. The path of the cosmic ray in the CsI array was determined by fitting a straight line to the blocks with energy deposited in them. We required a minimum of 10 blocks along the path to have an energy deposit. The path length inside each crystal was calculated from this path and used to normalize the signal from the crystal. For each crystal path lengths between 3.5 cm and 10 cm were selected for use. After normalizing for the path length, the energy deposit was fitted with a Landau function and the gain calculated using the energy deposit of a minimum ionizing particle in CsI which is 5.63 MeV/cm.

### 2.9.3 $\pi^0$ Calibration

During a special run at the end of data taking for Run I, a 5 mm aluminum target was placed after CC02 to produce  $\pi^0$ 's. A diagram of the setup is shown in Fig. 2.19. With the decay vertex known, we then can use correct the energy deposit so

the reconstructed mass matches the  $\pi^0$  mass.

$$M_{\gamma\gamma} = \sqrt{2E_1E_2(1 - \cos\theta)}. \quad (2.8)$$

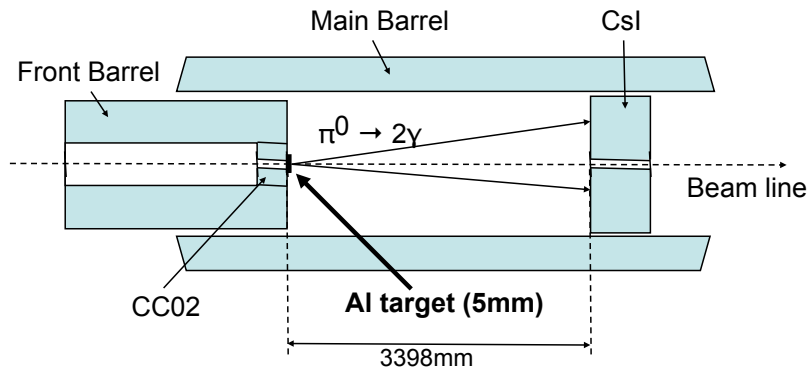


Figure 2.19: Diagram of geometry of pion target run.

With the CsI array full calibrated the mass resolution for  $K_L \rightarrow \pi^0\pi^0\pi^0$  reconstruction is 4.8 MeV as shown in Fig. 2.20.

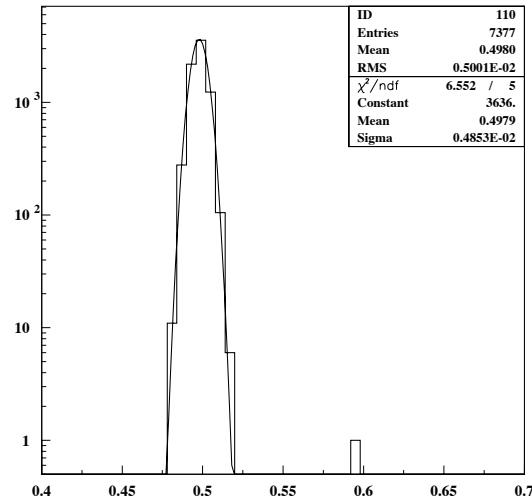


Figure 2.20: Reconstructed kaon mass distribution of good  $K_L \rightarrow \pi^0\pi^0\pi^0$  events. The mass peak was fit with a Gaussian. Scale is in  $\text{GeV}/c^2$ . The reconstructed mass peak is  $497.9 \pm 4.9 \text{ MeV}/c^2$ . The PDG value of the neutral kaon mass is  $497.648 \pm 0.022 \text{ MeV}/c^2$ .

## CHAPTER 3

### DAQ SYSTEM

In this chapter, I describe the data acquisition system used in the E391a experiment.

#### 3.1 Overview

All of the detectors in the E391a experiment use photo-multiplier tubes (PMT's) to change light that they produce into electrical signals. The signals that the PMT's produce are sent to Amplifier/Discrimination modules. These modules take the input from eight detector channels and produce individual analog signals for each channel, an analog sum signal of the eight channels, and an individual logic signal for the TDC. The individual analog signals are transferred to the ADC by 90 m long coaxial cables. The sum signal are passed to the trigger logic by 30 m long coaxial cables. The logic signal is transported by a 30 m twisted pair cable and has an additional 100 ns logic delay.

#### 3.2 Triggering

##### *3.2.1 Hardware Cluster*

The CsI array is divided in 72 different 8 block regions called the hardware clusters. These are used to define the online triggering. The analog signals from the eight CsI blocks in each cluster are summed in the Amp-Discriminator modules and then converted to a logic pulse with a threshold of 60 MeV. The logic pulses from all 72 hardware clusters are then summed. Physics data taking was done requiring 2 or

more hardware clusters to pass the threshold. The division of the CsI array into hardware clusters is shown in Fig 3.1.

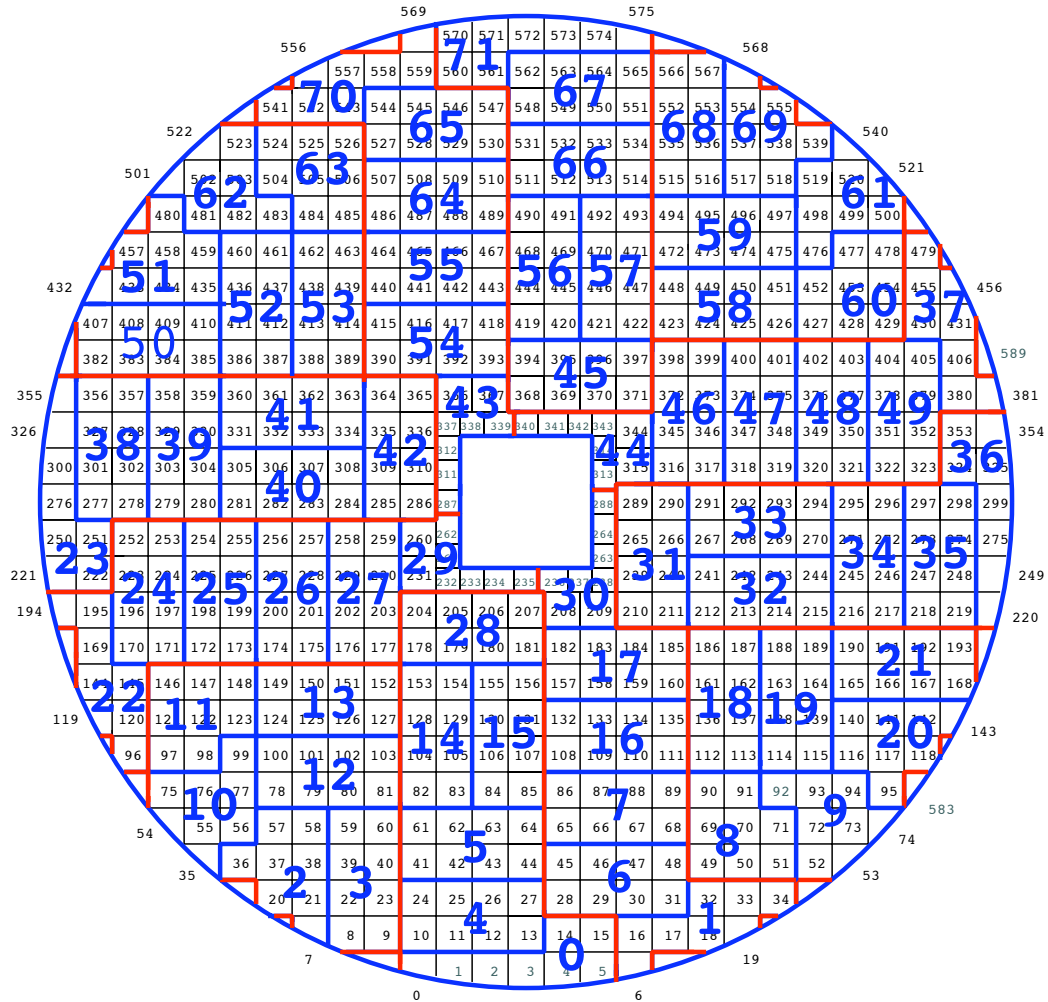


Figure 3.1: Layout of CsI Hardware Clusters.

### 3.2.2 Online Vetoes

To reduce the amount of data written to disk, loose vetoes were applied during data taking to remove obvious background events. The analog signals of the different

Detector	Online Veto Threshold (MeV)
CC02(Sum)	25
CC03(Sum)	15
CC04(Sum)	45
CC05(Sum)	25
Main Barrel(Downstream)	15
Front Barrel	30
Charge Veto	1.5

Table 3.1: Online veto threshold values converted to energy values.

photon vetoes were summed by Amp-Discriminator modules and converted into logic pulses if they passed the energy threshold. The signals from CC02, CC03, CC04, CC05, the downstream signals of the Main Barrel, the Front Barrel, and the Charge Veto are summed individually. Additionally to reduce over vetoing due to accidentals, the timing of these veto signals were required to be within a timing window individually set for each detector. The online veto threshold for each detector element are shown in Table 3.1.

### 3.2.3 *Physics Trigger*

The physics trigger for E391a was the requirement that two or more of the hardware clusters passed the energy threshold and none of the vetoes passed their threshold. For running during the one week period this gave us a trigger rate of approximately 800 events per 2 second beam spill with a live time ratio of 78%.

### 3.2.4 *Accidental Triggers*

The E391a beam is dominated by neutrons with a neutron to kaon ratio of approximately 60 to 1. This means the majority of activity in our detector is unrelated to kaon decays. This activity is occurring at all times, so it overlays the kaon decays we

are interested in. To properly understand our backgrounds this activity must be included in our simulations, but it is difficult to correctly reproduce low energy neutron activity with current Monte Carlo software.

Several different triggers were employed to provide an unbiased sampling of the accidental activity. The most useful trigger was the Target Monitor trigger. The Target Monitor is a counter telescope near the kaon production target. This trigger is therefore proportional to the beam intensity.

### *3.2.5 Calibration & Pedestal Triggers*

Additional triggers were used for monitoring the detectors and electronics. The CsI gain was monitored by a xenon lamp. The light output was fed to the CsI crystals by quartz fibers. The lamp flashed at a rate of 4 times a second.

Other detector components were flashed by a LED light system which operated on the same clock timing as the xenon lamp.

## **3.3 Timing**

The timing of energy deposit in each detector is measured using a TDC system. The system uses a common start and individual stop. The timing window is opened by the trigger signal and closed by the individual stop logic signal produced by the Amp/Disc module.

### *3.3.1 Calibration*

It is necessary to correctly determine the relative timing offsets of the different detector elements to use timing information in the analysis. To determine the timing of a signal we must measure the delays between the signal being generated and the TDC.

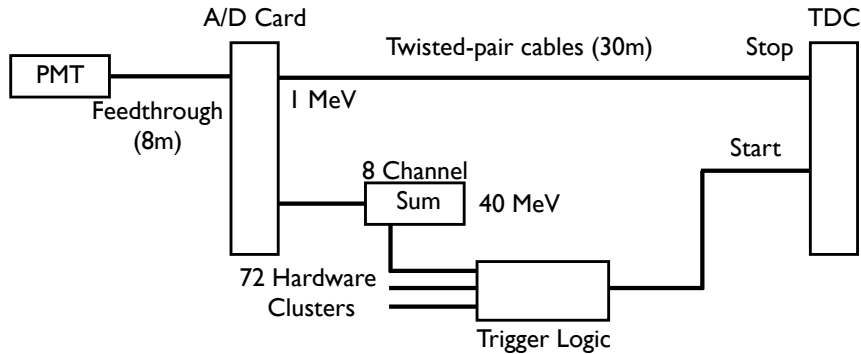


Figure 3.2: Signal propagation between PMT and TDC.

The timing is calibrated in stages, first the relative timings within the CsI channels are adjusted. Once the CsI timing is calibrated the other detectors timing is adjusted to match.

The calibration of the CsI timing can be divided into two parts, first the delays between the particle striking the CsI and the input of the Amp/Disc module and secondly between the input of the module and the TDC. The delay between the Amp/Disc module and the TDC was measured using a pulser on each channel. The delay from particle impact to the Amp/Disc module is fit in stages using three parameters for each channel: the propagation time from the photo-cathode of the PMT to the input of the Amp/Disc module, a correction factor the flight time of the cosmic ray muon, and a correction factor for the travel time of the scintillation light in the CsI. The travel time inside the CsI block was fit using tracks which start and end inside the calorimeter, corresponding to muons which strike the face of one CsI block and exit out the opposite face of another. The track can then be reconstructed in all three-dimensions and the timing difference between the crystals can be factored out. The distribution of timing difference between the six gammas of  $K_L \rightarrow \pi^0 \pi^0 \pi^0$  events was found to have a  $\sigma$  of 0.51 ns once the calibration was completed [18], as shown in Fig 3.3.

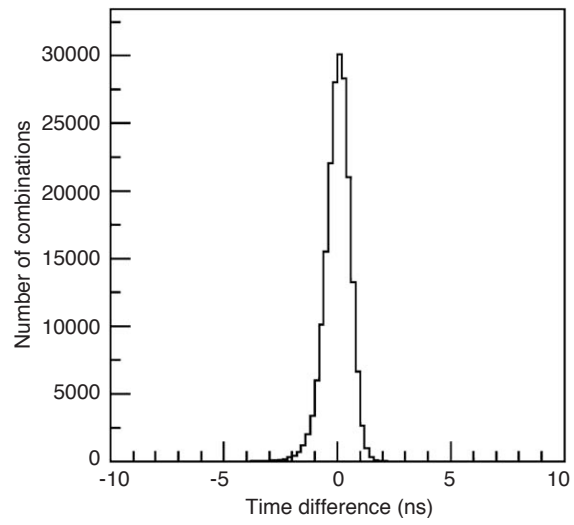


Figure 3.3: Time-difference distribution among 6γ's for  $K_L \rightarrow \pi^0 \pi^0 \pi^0$  [18].

## CHAPTER 4

### MONTE CARLO SIMULATION

We used a GEANT 3 [20] based Monte Carlo simulation to help understand our data. The Monte Carlo is used to calculate acceptance for the signal and normalization modes and to help identify our background sources. It is insufficient in statistics and accuracy to be used to predict the background to our signal.

#### 4.1 Event Generation

Kaons were generated with a momentum spectrum at the end of the beamline which is the position of the last collimator, C6. They were propagated forward to a decay point.

The  $K_L \rightarrow \pi^0\pi^0$  decay has no form factors and is generated with a flat phase space. The  $K_L \rightarrow \pi^0\pi^0\pi^0$  decay has a matrix element in the decay. However, the contribution is small ( $< 1\%$ ) and is not included in our Monte Carlo generation. The  $K_L \rightarrow \pi^0\pi^0\nu\bar{\nu}$  decay has a form factor as described in Chapter 2. Simulations were performed with and without this factor. The  $K_L \rightarrow \pi^0\pi^0P$  decay was generated without a matrix element with a flat phase space. Events with a range of masses were generated.

#### 4.2 Samples

The sample sizes for the different decay modes are summarized in Table 4.1. In order to increase the speed of the simulation we did not fully process all events.

For comparison to data the  $K_L \rightarrow \pi^0\pi^0$  and  $K_L \rightarrow \pi^0\pi^0\pi^0$  samples are used with events with four clusters in the CsI array. The  $K_L \rightarrow \pi^0\pi^0$  sample is normalized

Mode	Sample Size	Data Equivalent
$K_L \rightarrow \pi^0\pi^0$	$1.36 \times 10^7$ $K_L$ decays in fiducial region	870%
$K_L \rightarrow \pi^0\pi^0\pi^0$	$1.36 \times 10^8$ $K_L$ decays in fiducial region	46%
Core Neutron	$7.5 \times 10^9$ at C6	$\approx 10\%$
$K_L \rightarrow \pi^0\pi^0\nu\bar{\nu}$	$1.45 \times 10^6$ $K_L$ decays in fiducial region	NA
$K_L \rightarrow \pi^0\pi^0P$	$2.0 \times 10^5$ $K_L$ decays in fiducial region for each mass value	NA

Table 4.1: Monte Carlo samples and their equivalent data size.

to data through the  $K_L \rightarrow \pi^0\pi^0$  mass peak. The  $K_L \rightarrow \pi^0\pi^0\pi^0$  sample is then normalized to  $K_L \rightarrow \pi^0\pi^0$  through the branching ratio.

#### 4.2.1 Decay Region

The main background modes of  $K_L \rightarrow \pi^0\pi^0$  and  $K_L \rightarrow \pi^0\pi^0\pi^0$  were allowed to propagate and decay according to the kaon lifetime after their generation at C6 (-192.5 cm). The fraction of kaons which decayed in the fiducial region (300 to 500 cm) was 2.72%.

For the signal mode samples we controlled where the kaon decayed. Events were generated with kaons decaying in the region between 200 cm to 600 cm. The fraction of kaons which decayed in the fiducial region (300 to 500 cm) was 50.0%

#### 4.2.2 Energy Cut-offs

To speed processing time loose vetoes were applied during the event generation stage. When energy deposited in a detector element surpassed these limits (see Table 4.2), the further processing of the event was halted.

Detector Element	Simulation Cut-Off
CC02	50 MeV
CC03	50 MeV
CC04	50 MeV
CC05	50 MeV
CC06	50 MeV
CC07	50 MeV
Main Barrel	50 MeV
Front Barrel	50 MeV
Charge Veto	2 MeV

Table 4.2: Simulation cut-off values for individual detectors. If the energy deposit in a detector element exceeds this value processing of the event is halted.

### 4.3 Accidental Overlay

The beam related background is nearly impossible to simulate and so we must take information from the data to properly account for it. We use the accidental target monitor trigger to collect a sample of events which is representative of the activity in the detector during running.

Then a randomly selected accidental event is overlaid on top of one Monte Carlo event. This is done by adding the energies on a channel by channel basis. The channel's timing is produced by selecting the earliest signal between the Monte Carlo and accidental overlay.

### 4.4 Data and Monte Carlo Comparison

The Monte Carlo reproduces well most aspects of the E391a data. There are inconsistencies in the timing and neutron interactions. The primary indicator that our Monte Carlo is imperfect is a significant discrepancy between the low mass  $K_L \rightarrow \pi^0 \pi^0 \pi^0$  peak in data and Monte Carlo as shown in Fig 4.1. The Monte Carlo predicts a higher level of background than the data. This results in a discrepancy in the vertex

distribution as well, due to the number  $K_L \rightarrow \pi^0\pi^0\pi^0$  events having a strong position dependence. We handled this problem by varying the normalization of  $K_L \rightarrow \pi^0\pi^0\pi^0$  relative to that of  $K_L \rightarrow \pi^0\pi^0$ . The improvement can be seen in Fig 4.2.

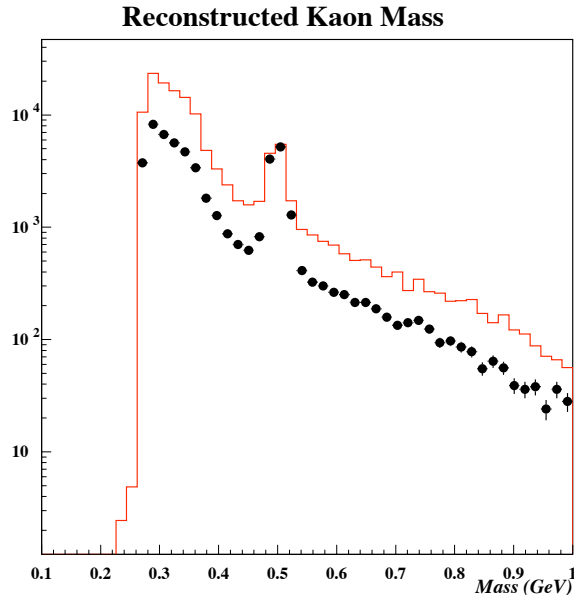


Figure 4.1: Reconstructed invariant mass for data and Monte Carlo for  $4\gamma$  events. Monte Carlo is normalized to data using the  $2\pi^0$  mass peak. It includes  $K_L \rightarrow \pi^0\pi^0\pi^0$  and  $K_L \rightarrow \pi^0\pi^0$  events, which are normalized relative to each other by branching ratio. The accidental overlay is applied.

After varying the normalization, Monte Carlo well reproduces the kinematic variables associated with the kaon beam. A sample of the comparisons is shown in Fig. 4.3. Comparison of Monte Carlo and data energy spectrums for individual detector elements is shown in Chapter 3 in the sections for each detector.

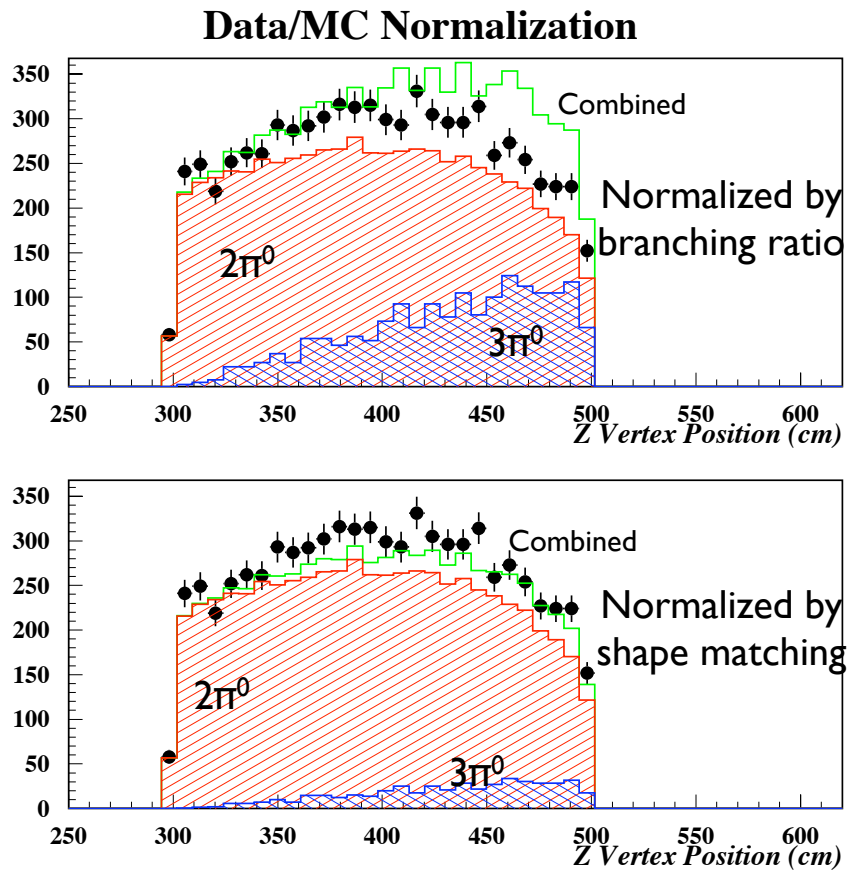


Figure 4.2: Reconstructed  $Z$  decay vertex for  $4\gamma$  events. Top plot shows  $K_L \rightarrow \pi^0\pi^0$  and  $K_L \rightarrow \pi^0\pi^0\pi^0$  MC samples normalized relative to each other by their branching ratio. Bottom plot shows them relatively normalized to match data.

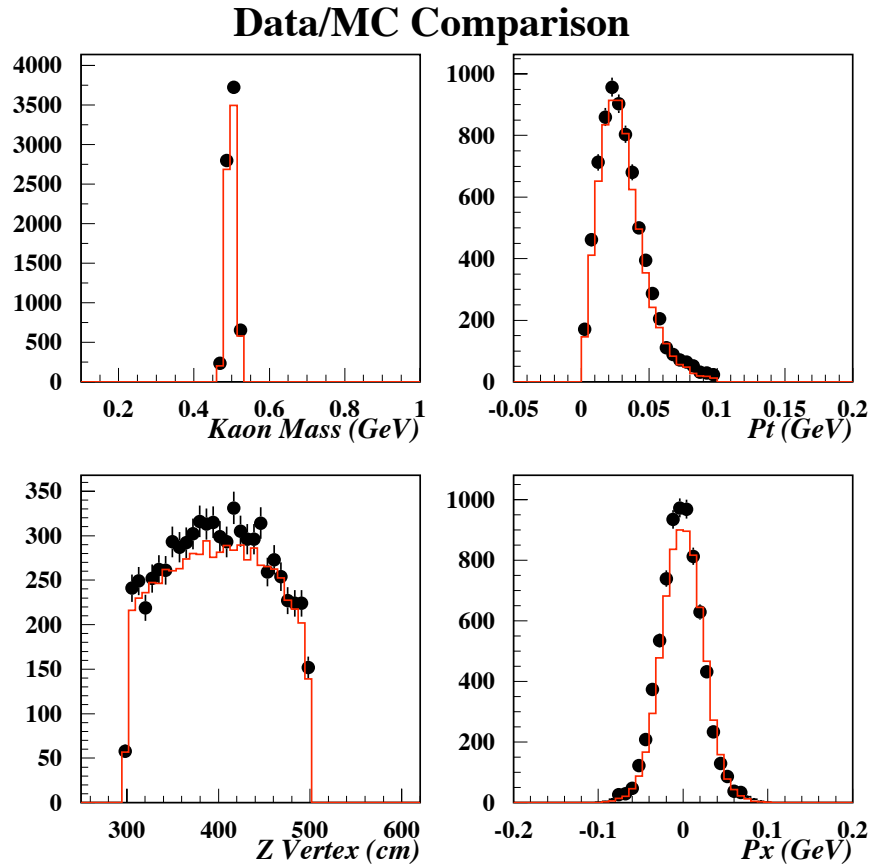


Figure 4.3: Monte Carlo-data comparison in  $K_L \rightarrow \pi^0\pi^0$  signal region for reconstructed kaon mass,  $P_T$ ,  $z$  of decay vertex, and kaon momentum in the horizontal direction. MC sample include  $K_L \rightarrow \pi^0\pi^0$  the count in  $K_L \rightarrow \pi^0\pi^0$  signal region and  $K_L \rightarrow \pi^0\pi^0\pi^0$  normalized to match distributions. Loose cuts are applied. Dots represent data and the line represents MC.

# CHAPTER 5

## RECONSTRUCTION

In this chapter we describe the procedure for going from the signals in the detector to a reconstructed kaon. We also describe the cuts applied to the reconstructed gammas and the kaon reconstruction.

### 5.1 Clustering

The first stage in the reconstruction is finding the photons which struck the CsI array. We call this process clustering. We find clusters of blocks which all have energy deposited by single photons in them using the following algorithm. The first step is producing a list of blocks which are a local maximum of energy deposit. From these “seed” blocks we build clusters.

First, we check for a minimum energy threshold of 5 MeV. Then, the horizontally and vertically adjacent blocks are checked if they have energy above 3 MeV. If they do, they are added to the cluster. The process is then repeated for the blocks which have been added to the cluster.

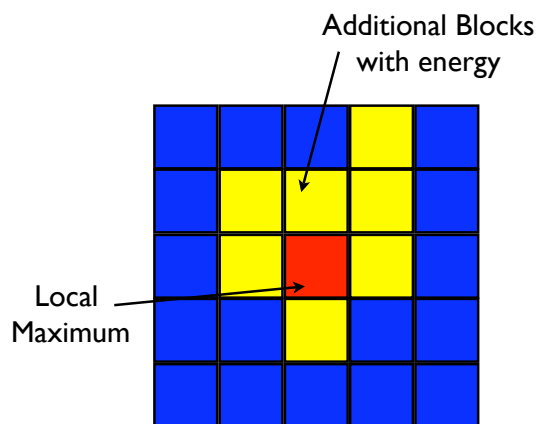


Figure 5.1: Diagram of clustering procedure.

### 5.1.1 Cluster Position

The first iteration of the finding the cluster position is to calculate the center of energy position:

$$x_{COE} = \left( \sum_{i=1}^{N_{\text{blocks}}} x_i E_i \right) / E_{\text{cluster}}. \quad (5.1)$$

### 5.1.2 Cluster Energy Recalculation

The KEK CsI crystals are 30 cm long which corresponds to 16.2 radiation lengths. This does not fully contain all the electromagnetic showers that are produced. We therefore apply a correction to the raw energy calculated by summing the energy deposit in each crystal. The energy leak through was studied using Monte Carlo data and parameterized:

$$\text{leak} = 0.024 + \frac{1.664 \times 10^{-2}}{\sqrt{E_{\text{deposit}}}} \quad (5.2)$$

$$E_{\text{corrected}} = (1 + \text{leak}) \times E_{\text{deposit}} \times 1.01. \quad (5.3)$$

### 5.1.3 Cluster Timing

The timing of the clusters is determined by the TDC value of the peak block in each cluster. The timing for the clusters, as for all detectors, is relative to the time of the earliest cluster. The calibration of the timing for individual blocks is described in Sect. 3.3.1.

## 5.2 $\pi^0$ Reconstruction

The second step in reconstructing an event is the determination of the decay vertex. The photons we are interested in are the daughter particles of  $\pi^0$ 's which are in turn daughter particles of the  $K_L$ . All of the decays we are interested in have  $\pi^0$ 's which decay into two photons with a branching fraction of  $(98.798 \pm 0.032)\%$  [? ].

Making the assumption that the photons we observe in the CsI come from the decay of a  $\pi^0$ , we can reconstruct the decay vertex of the  $\pi^0$ . We must assume that the  $K_L$  decayed at the beam center, because we are missing energy in the CsI, due to neutrinos or missing photons, so the center of energy in the CsI does not correspond to the decay vertex. This is called the pencil beam assumption. Making this assumption introduces spurious transverse momentum into our reconstruction, but with missing energy in our signal modes, we have no way of calculating the  $x$  and  $y$  position. The  $z$  vertex can be calculated using the photons' energy and position along with the assumption that they both came from the same  $\pi^0$ .

### 5.2.1 $Z$ Vertex

By using energy and momentum conservation we can calculate the opening angle between the two photons:

$$p_{\pi^0}^2 = (p_{\gamma 1} + p_{\gamma 2})^2, \quad (5.4)$$

$$E_{\pi^0}^2 - m_{\pi^0}^2 = p_{\gamma 1}^2 + p_{\gamma 2}^2 + 2p_{\gamma 1} \cdot p_{\gamma 2}, \quad (5.5)$$

$$E_{\gamma 1}^2 + E_{\gamma 2}^2 + 2E_{\gamma 1}E_{\gamma 2} - m_{\pi^0}^2 = E_{\gamma 1}^2 + E_{\gamma 2}^2 + 2E_{\gamma 1}E_{\gamma 2} \cos \theta, \quad (5.6)$$

$$m_{\pi^0}^2 = 2E_{\gamma 1}E_{\gamma 2}(1 - \cos \theta), \quad (5.7)$$

$$\cos \theta = 1 - \frac{m_{\pi^0}^2}{2E_{\gamma 1}E_{\gamma 2}}. \quad (5.8)$$

It is important to note that in many experiments using this technique it is possible

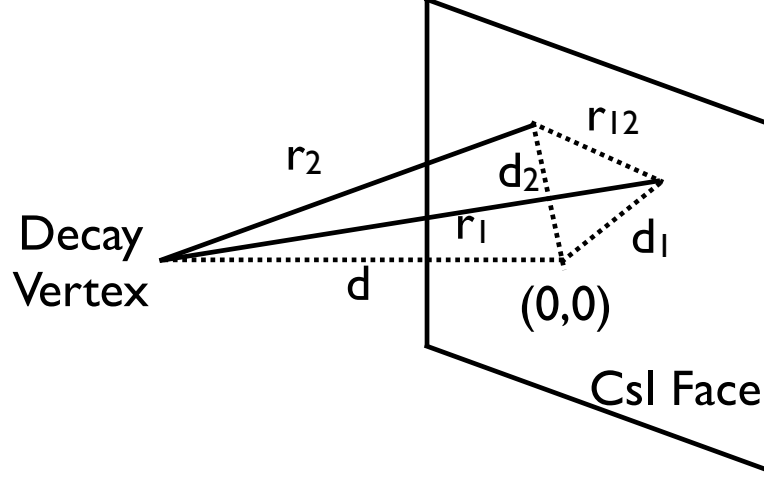


Figure 5.2: Reconstruction of pion decay vertex.

to approximate the  $\cos \theta$  using a small angle approximation. In our case this is not possible due to the relatively low energy of  $\pi^0$ 's and the closeness of the fiducial decay region to the CsI face which can produce separation angles of nearly  $90^\circ$ .

Using the opening angle, we can relate the separation of the photons,  $r_{12}$ , to their path lengths,  $d_1$  and  $d_2$ :

$$r_{12}^2 = d_1^2 + d_2^2 - 2d_1d_2 \cos \theta. \quad (5.9)$$

The path lengths of the photons are simply:

$$d_1 = \sqrt{r_1^2 + d^2}, d_2 = \sqrt{r_2^2 + d^2}. \quad (5.10)$$

We relate the photon separations to their  $x$  and  $y$  coordinates on the CsI face:

$$r_1^2 + r_2^2 - r_{12}^2 = 2(x_1x_2 + y_1y_2). \quad (5.11)$$

Substituting  $d_1$ ,  $d_2$ , and  $r_{12}$  into Eqn 5.9, gives us:

$$(r_1^2 + d^2)(r_2^2 + d^2) \cos^2 \theta = (d^2 + \frac{r_1^2 + r_2^2 - r_{12}^2}{2})^2. \quad (5.12)$$

Rearranging the equation we find:

$$\begin{aligned} d^4(1 - \cos^2 \theta) - d^2(r_{12}^2 - (r_1^2 + r_2^2)(1 - \cos^2 \theta)) + \\ (x_1x_2 + y_1y_2)^2 - r_1^2r_2^2 \cos^2 \theta = 0. \end{aligned} \quad (5.13)$$

In order to solve this expression, we first simplify it by introducing several new variables:

$$a = (1 - \cos^2 \theta), \quad (5.14)$$

$$b = r_{12}^2 - (r_1^2 + r_2^2)(1 - \cos^2 \theta), \quad (5.15)$$

$$c = (x_1x_2 + y_1y_2)^2 - r_1^2r_2^2 \cos^2 \theta, \quad (5.16)$$

$$a \cdot d^4 - b \cdot d^2 + c = 0. \quad (5.17)$$

This is simply a quadratic equation for the square of the distance. Solving for the square of the distance we find:

$$d^2 = \frac{b \pm \sqrt{b^2 - 4ac}}{2a}. \quad (5.18)$$

This leads us to as many as four different values of the distance between the kaon decay vertex and CsI calorimeter. The negative solutions of  $\sqrt{d^2}$  correspond to vertices downstream of the CsI array, these we ignore. Only one of the solutions of the  $d^2$  equation is consistent with the pion mass we assumed at the beginning. We can check which one is correct by using the value of  $d$ , the photons' hit position, and energy

to calculate the photons' 4-momentum. Using the 4-momentum we can calculate the invariant mass of the pion. The calculated mass of the correct solution will be very close to the true  $\pi^0$  momentum and the incorrect solution will typically be very different. In some cases where the value of  $b^2 - 4ac$  is small the recalculated mass will not be that different so we must carry both possible solutions into the pairing algorithm.

### 5.2.2 Selection of Pairing

There are three possible ways to assign four photons to two pions and fifteen ways six photons can be assigned to 3 pions. We have an additional possible ambiguity from the calculation of the decay vertex which could increase the number of solutions to 12 for the four photon case and 120 for six photons. In general if the photons are paired incorrectly the decay vertices of the different pions will not match. To quantify this we created a  $\chi^2$  variable for the differences in vertex position:

$$\chi^2 = \sum_{i=1}^{N_{\pi^0}} \frac{(z_{avg} - z_i)^2}{\sigma_i^2}. \quad (5.19)$$

We select the pairing with the smallest  $\chi^2$ . Additionally, we apply cuts on the  $\chi^2$  of the best pairing and the second best pairing. Now, knowing the decay vertex of the  $\pi^0$ 's, we can use the cluster position and energy to determine the photon momentum.

### 5.2.3 Transverse Momentum

An important variable for identifying the event type is the transverse momentum of the  $\pi^0$ - $\pi^0$  system:

$$P_T = \sqrt{p_x^2 + p_y^2}. \quad (5.20)$$

The  $P_T$  squared is a relativistic invariant. A perfectly reconstructed  $K_L \rightarrow \pi^0\pi^0$  event should have nearly zero  $P_T$  corresponding to the angular spread of the beam. However, by making our pencil beam assumption we introduce additional  $P_T$  into our reconstruction.

### 5.3 Normalization Modes

In order to know what limit we can set for the decay modes of interest, we must first determine the number of  $K_L$ 's that passed through our detector in the experiment. To do this we measured two well understand kaon decays,  $K_L \rightarrow \pi^0\pi^0\pi^0$  and  $K_L \rightarrow \pi^0\pi^0$ .

#### 5.3.1 $2\pi^0$ Mode

The decay  $K_L \rightarrow \pi^0\pi^0$  is extremely important as a normalization mode, because it shares so many of the characteristics of the  $K_L \rightarrow \pi^0\pi^0\nu\bar{\nu}$  mode. Both of the decays have four photons in the final state and the same reconstruction algorithm can be applied.

The same reconstruction routine can be applied to both  $K_L \rightarrow \pi^0\pi^0$  and  $K_L \rightarrow \pi^0\pi^0\nu\bar{\nu}$ , and so we do. For the purposes of normalization we define a  $2\pi^0$  box in the  $P_T$ -mass plane. The box is defined as  $473\text{MeV}/c^2 < M < 523\text{MeV}/c^2$  and  $P_T < 80\text{MeV}/c$ . The distribution is shown in Fig 5.3.

#### 5.3.2 $3\pi^0$ Mode

As a cross check of our flux calculation with  $K_L \rightarrow \pi^0\pi^0$ , we also determine the flux using the decay  $K_L \rightarrow \pi^0\pi^0\pi^0$ . With 6 photons in the CsI array there are no significant background modes to the decay.

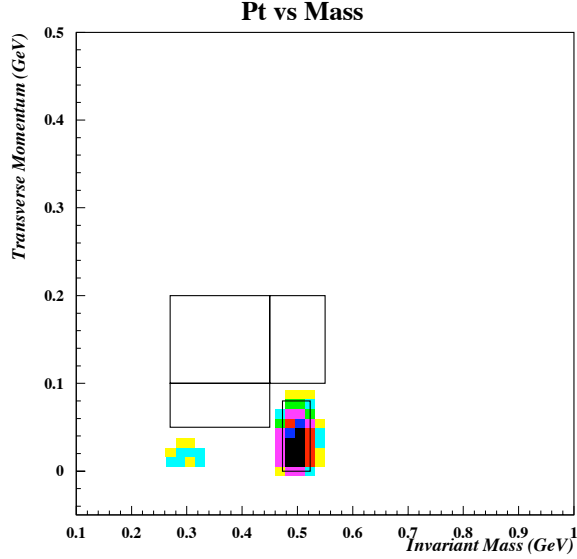


Figure 5.3: Distribution of Monte Carlo  $K_L \rightarrow \pi^0 \pi^0$  events in the  $P_T$  -Mass plane.

## 5.4 Signal Modes

### 5.4.1 $K_L \rightarrow \pi^0 \pi^0 \nu \bar{\nu}$

The decay  $K_L \rightarrow \pi^0 \pi^0 \nu \bar{\nu}$  has a signature of four photons in the CsI array which reconstruct to two pions, with a high  $P_T$  and a low invariant mass. The maximum  $P_T$  for this mode is 209 MeV/c. The kinematically allowed region forms a triangle in the  $P_T$  -mass plane. The minimum invariant mass is  $2m_{\pi^0}$ . The distribution is shown in Fig 5.4.

### 5.4.2 $K_L \rightarrow \pi^0 \pi^0 P$

The signature for  $K_L \rightarrow \pi^0 \pi^0 P$  is very similar to that of  $K_L \rightarrow \pi^0 \pi^0 \nu \bar{\nu}$ . The bounds in the  $P_T$  -mass plane depend on the mass of the  $P$ . Since the mass of the  $P$  is not predicted by theory, we must run simulations for a range of  $P$  masses. Our acceptance decreases as the mass of the  $P$  increases, because the available energy

to go into the transverse motion of the daughter particles decreases. With lower allowable  $P_T$ , a larger fraction of the signal events are in the same  $P_T$ -mass region as the  $K_L \rightarrow \pi^0\pi^0\pi^0$  background. A selection of distributions for differing masses are shown in Fig 5.4.

### 5.4.3 Signal Box

Poor reconstructions often manifest themselves as events with a z vertex close to the CsI face and with a high  $P_T$ . Additionally, the vacuum membrane hangs into the beam line at the location of the Charge Veto at 550 cm. We therefore cut events close to the CsI. Additionally, CC02 and the Front Barrel strongly restrict the decay volume that we can see. Therefore events which are reconstructed upstream, outside of our fiducial region, are also cut. We define the fiducial decay region as between 300 and 500 cm.

As discussed below the  $K_L \rightarrow \pi^0\pi^0\pi^0$  background sets a lower bound for the  $P_T$  at which we can achieve a high signal to background ratio. We set the lower bound for allowed  $P_T$  at  $100\text{MeV}/c^2$ . The maximum  $P_T$  which these decays produce corresponds to the mass difference between the  $K_L$  and  $2\pi^0$ 's. We set the upper bound of the signal box at  $200\text{MeV}/c^2$ .

## 5.5 Cut Philosophy

The primary consideration for the tuning of the individual cuts was maximizing the signal-to-noise ratio for that cut. This was done by comparing the effect of the cut on the  $K_L \rightarrow \pi^0\pi^0\pi^0$  Low Mass-Low  $P_T$  region and the  $K_L \rightarrow \pi^0\pi^0$  signal region. Acceptance loss from the cuts was a secondary factor which we studied using both the  $K_L \rightarrow \pi^0\pi^0$  signal region and the  $K_L \rightarrow \pi^0\pi^0\nu\bar{\nu}$  Monte Carlo. The signal-to-noise

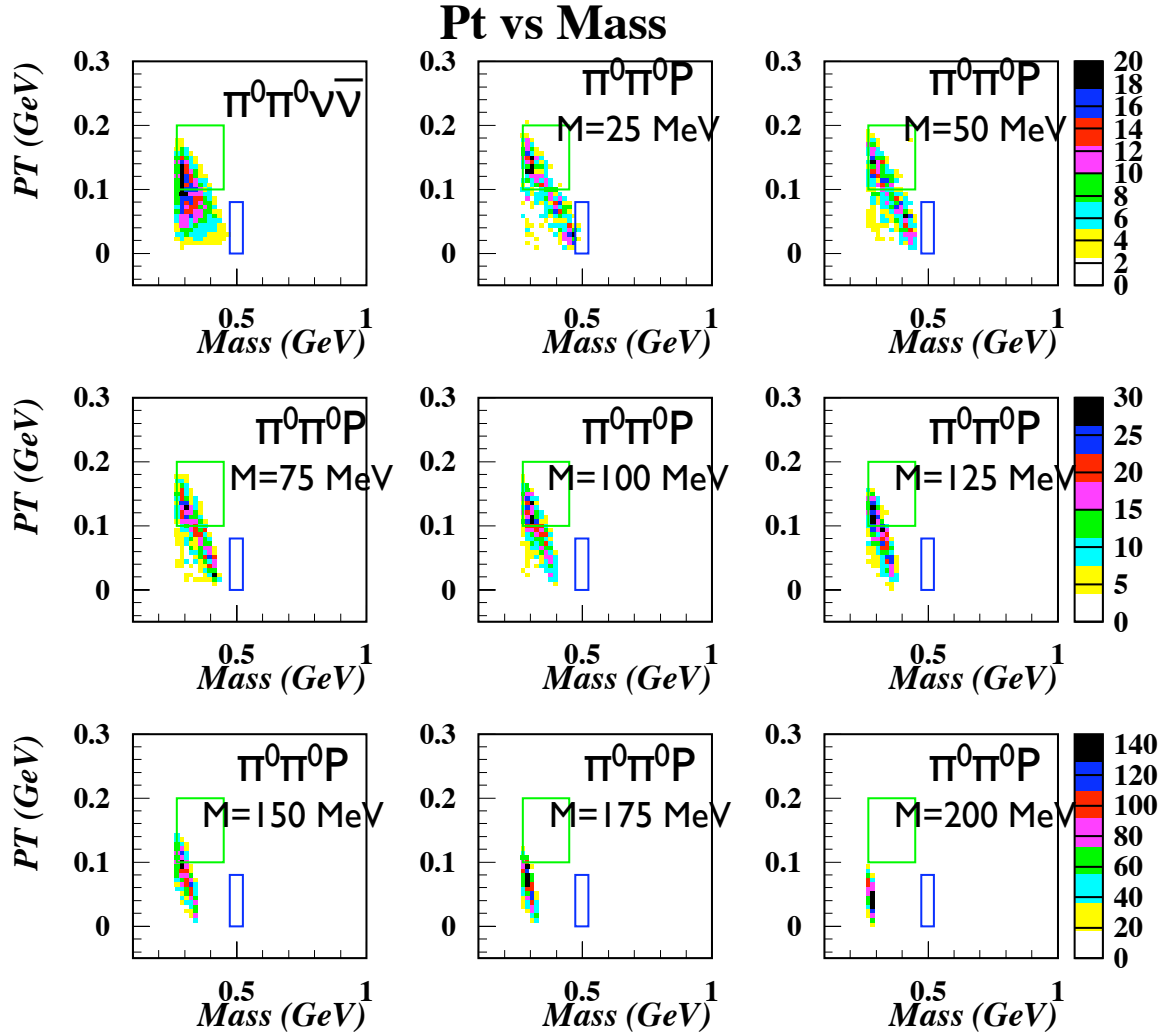


Figure 5.4: Event distributions in the  $P_T$  -Mass plane for  $K_L \rightarrow \pi^0\pi^0\nu\bar{\nu}$  and  $K_L \rightarrow \pi^0\pi^0P$  signal modes. Green box represents the signal box and the blue box represents the  $K_L \rightarrow \pi^0\pi^0$  signal box used for normalization.

ratios and acceptance losses from the cuts are shown in Table 5.1.

## 5.6 Veto Cuts

Since the primary background is  $K_L \rightarrow \pi^0\pi^0\pi^0$  it is of primary importance to detect all photons produced by the decay of the kaon. For this analysis we applied the following photon vetoes: CC02, CC03, CC05, Front Barrel, Main Barrel, and Back-Anti. There are no major charged backgrounds to the decay modes we are interested in, so we only cut on the charged veto systems at the online level. More detailed descriptions of the veto cuts are found in Sections 2.3 to 2.9. The values of the cuts, the acceptance losses, and signal-to-noise ratios of the cuts are shown in Table 5.1.

## 5.7 Gamma Quality Cuts

A large source of “missing” photons is cluster fusion in the CsI array. This occurs when two photons strike the array close together and our clustering routine does not separate them. Cuts on a variety of variables associated with the cluster can be used to identify these fusion events. Additionally, the neutron background is characterized by photons being generated close to the CsI face which produces photons striking the CsI at high angles which have properties distinct from the those produced by kaon decays in the fiducial region.

### 5.7.1 Neural Network for Fusion Identification

We apply a neural network to the cluster which has been trained to identify photon fusion. A neural network is a flexible algorithm for the separation of events into different classes. The inputs are multiplied by weights and summed. A function  $\sigma$  is

then applied to produce the inputs for each of the "hidden" layers. This process is repeated to produce the output from the hidden layer. A schematic of the connections is shown in Fig 5.5:

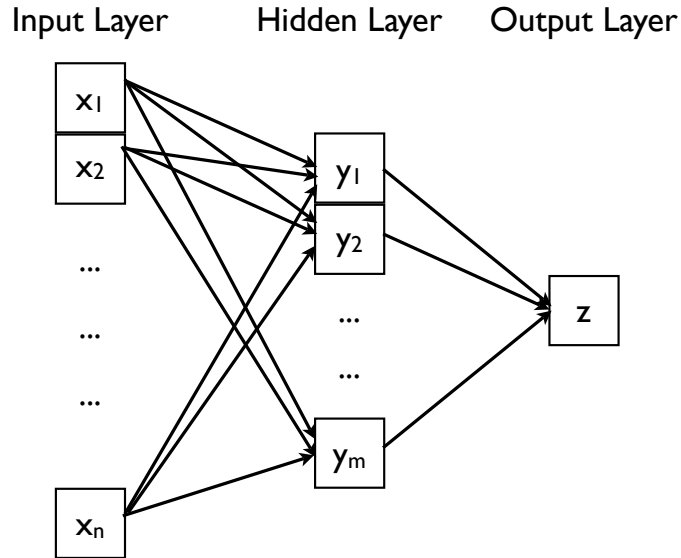


Figure 5.5: Schematic of neural network.

$$y_j = \sigma\left(\sum_{k=1}^n W_{jk}x_k + B_j\right), \quad (5.21)$$

$$z = \sigma\left(\sum_{k=1}^m W_kx_k\right). \quad (5.22)$$

Here  $\sigma$  is a sigmoid function. A sigmoid function smoothly maps  $(-\infty, \infty)$  onto  $(0,1)$ , is monotonic, and is linear when  $|x| \approx 0$ . For our neural net, we use the function:

$$\sigma(x) = \frac{1}{1 + e^{-x}}. \quad (5.23)$$

This is plotted in Fig 5.6.

Our neural network for fusion identification has 12 inputs, 10 hidden units, and 1

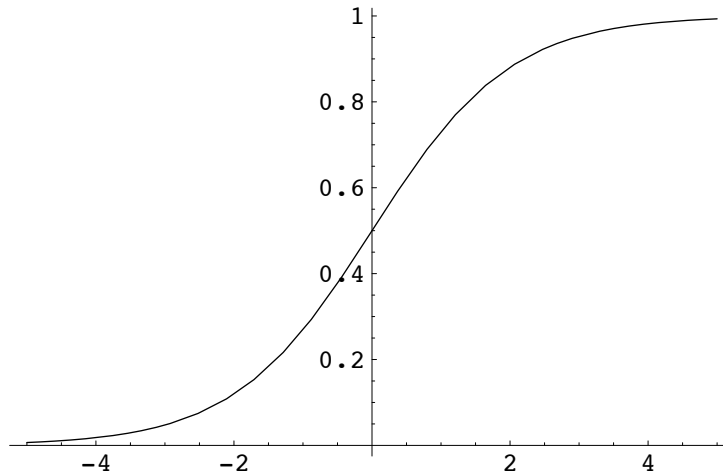


Figure 5.6: The sigmoid function  $\sigma(x) = \frac{1}{1+e^{-x}}$ .

output. The inputs are the energies deposited in the nine blocks around the center of the cluster normalized by the total energy, the cluster position on the CsI face, and its azimuthal angle.

### 5.7.2 Training the Neural Network

Before the neural network can be used, the weights must be “trained.” This is equivalent to fitting a non-linear function. The algorithm which we used is called “back-propagation.” In back-propagation the errors of the function are first calculated for the last layer and then propagated backwards to the earlier layers. Using these errors a non-linear fitting procedure can be applied.

The neural network for fusion identification was trained a combination of Monte Carlo and real data. To properly train the network a sample of photon clusters with fusion and without is necessary. For our sample of clusters without fusion we used data from our 6 gamma sample with clean  $K_L \rightarrow \pi^0\pi^0\pi^0$  reconstructions. The fusion sample is taken from our Monte Carlo, where we required five clusters identified when six clusters hit the CsI. A comparison of the output for data and Monte Carlo is shown

in Fig 5.7.

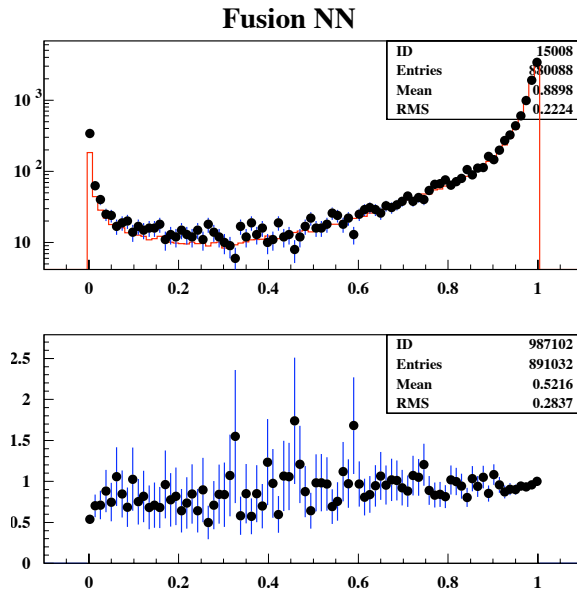


Figure 5.7: Comparison for Fusion Neural Net output for data and Monte Carlo. Data is represented by the black dots and Monte Carlo by the red line. Samples are normalized by the maximum bin. Lower plot is ratio of Monte Carlo to data.

### 5.7.3 Energy Cut

We cut events which have reconstructed photons below a minimum energy. Low energy photon events can be produced by either accidental activity or from  $K_L \rightarrow \pi^0 \pi^0 \pi^0$  events which tend to have lower photon energies than many of our signal modes. We cut any event with a gamma energy of less than 200 MeV.

### 5.7.4 Gamma Fiducial Cut

The inner and outer edges of our CsI array suffer a variety of problems. The inner edge, close to the beam, has significant level of accidental activity. The outer edge consists of CsI blocks which have been cut. They both face the prospect of photon showers which have not been completely contained within the calorimeter. Therefore,

we require all the reconstructed photons to be within a fiducial region. We require the photons to be outside a 35 cm by 35 cm box around the beamhole. This corresponds to being outside the inner layer of  $7 \times 7$  cm crystals. We also require the photons be inside a 90 cm circle from the center of the beamline.

### 5.7.5 *Gamma EDI*

We cut on the spread of photon energies in the event. This cut is called the gamma energy dispersion index. Events with an E.D.I. of less than 0.8 are cut:

$$\text{Gamma E.D.I.} = \frac{1}{N} \sqrt{\sum (E_i - E_m)^2}. \quad (5.24)$$

Here,  $E_i$  is the energy of one of the reconstructed photons and  $E_m$  is the mean energy of the reconstructed photons. A comparison of the Gamma E.D.I. between data and Monte Carlo is shown in Fig 5.8.

### 5.7.6 *Gamma TDI*

We cut on the spread of photon cluster timing. This cut is the called the gamma timing dispersion index. Events with a T.D.I. of greater than 2.0 are cut:

$$\text{Gamma T.D.I.} = \frac{1}{N} \sqrt{\sum (T_i - T_m)^2}. \quad (5.25)$$

Here,  $T_i$  is the timing of one of the reconstructed photons and  $t_m$  is the mean timing of the reconstructed photons. A comparison of the Gamma T.D.I. between data and Monte Carlo is shown in Fig 5.8. Our Monte Carlo does not well reproduce timing at this point. Therefore we cannot use the Monte Carlo to study acceptance loss from this cut.

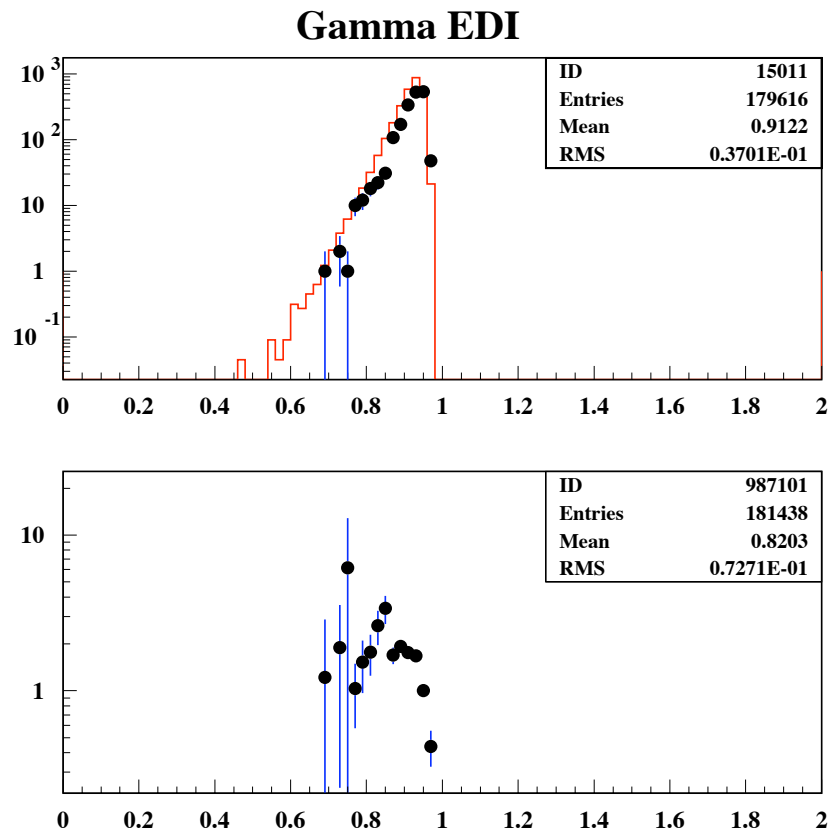


Figure 5.8: Gamma EDI. Data is represented by the black dots and Monte Carlo by the red line. Samples are normalized by the maximum bin. Lower plot is ratio of Monte Carlo to data.

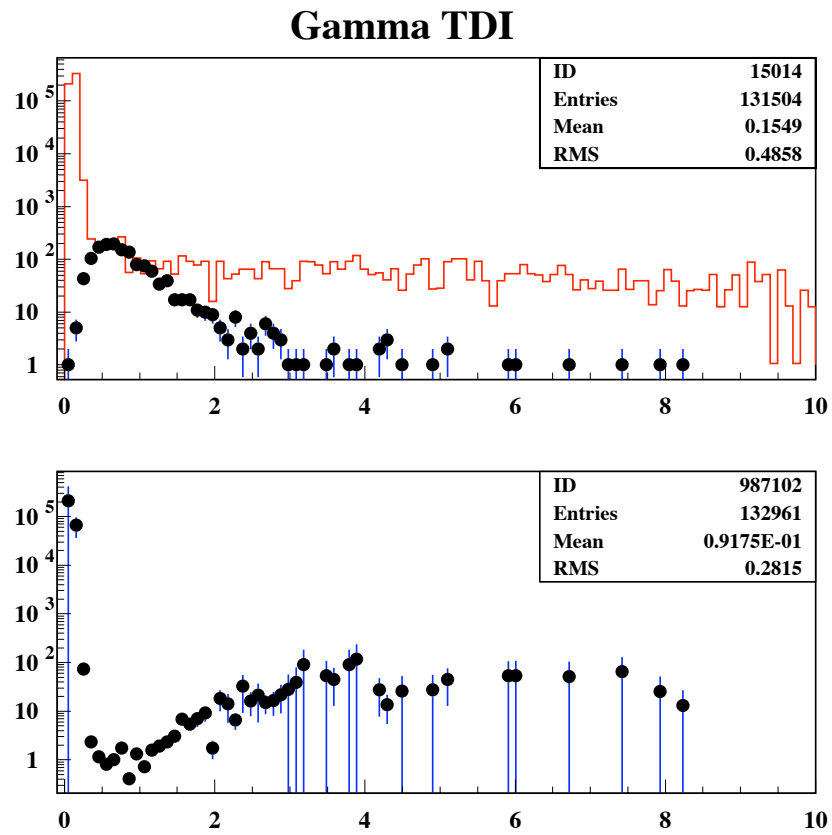


Figure 5.9: Gamma TDI. Data is represented by the black dots and Monte Carlo by the red line. Samples are normalized by the maximum bin. Lower plot is ratio of Monte Carlo to data.

### 5.7.7 Gamma R.M.S.

We construct a cut on the shape of the photon cluster:

$$\text{Gamma R.M.S.} = \sqrt{\frac{\sum E_i \times r_i^2}{\sum E_i}}. \quad (5.26)$$

Here,  $E_i$  is the energy of an individual block in the cluster and  $r_i$  is distance between the center of that block and the reconstructed cluster position. We cut on the R.M.S. with different values depending on the number of blocks in the cluster. The cut values are shown in Fig 5.10. A comparison between data and Monte Carlo values of the R.M.S. is shown in Fig 5.11.

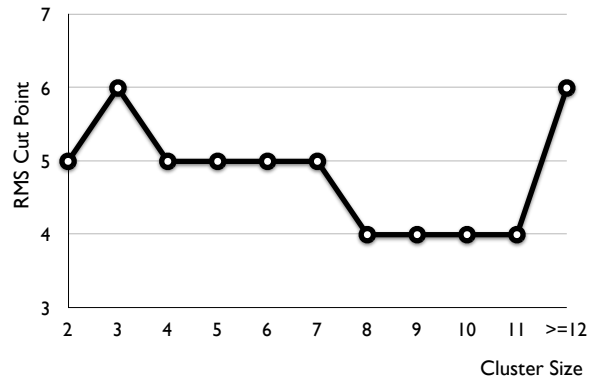


Figure 5.10: Cut point for Gamma R.M.S. as a function of cluster size in CsI blocks.

### 5.7.8 Gamma Energy Ratio

An additional cut on the quality of the gamma is a cut on the ratio of the three highest energy blocks to the total cluster energy. We apply the cut when a cluster has an energy ratio of less than 0.8:

$$\text{Gamma Energy Ratio} = \frac{E_1 + E_2 + E_3}{\sum E_i}. \quad (5.27)$$

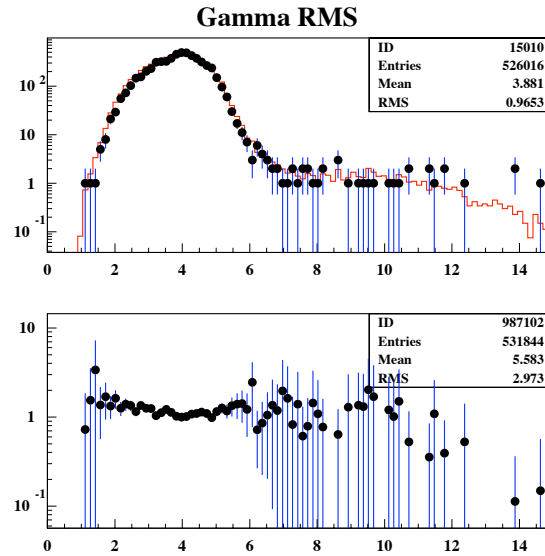


Figure 5.11: Gamma RMS. Data is represented by the black dots and Monte Carlo by the red line. Samples are normalized by the maximum bin. Lower plot is ratio of Monte Carlo to data.

Here,  $E_1$  to  $E_3$  are the three highest energy blocks and  $E_i$  are the energies of each individual block. A comparison of this variable between data and Monte Carlo is shown in Fig 5.12.

## 5.8 Reconstruction Quality Vetoes

It is important to test that the reconstruction of the kaon has been done correctly. The most important figure of merit for the quality of the reconstruction is the  $\chi^2$  of the  $\pi^0$  vertices, Eqn 5.19. We select the pairing which produces the lowest  $\chi^2$  value as the pairing which we reconstruct.

### 5.8.1 Best $\chi^2$

If the  $\chi^2$  of the best pairing is large then that indicates that the reconstruction is a poor one. We therefore require the  $\chi^2$  of the best pairing to be less than 0.5. A

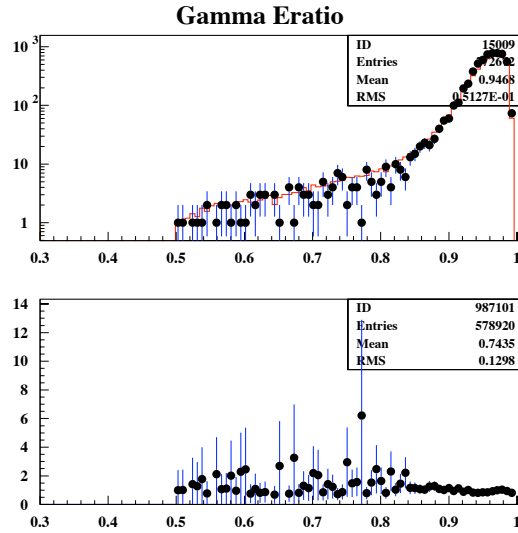


Figure 5.12: Energy ratio.

comparison between data and Monte Carlo for this variable is shown in Fig 5.13.

### 5.8.2 Second Best $\chi^2$

Another effective cut is to look at the  $\chi^2$  of the second best pairing. If it is small then that can indicate that the pairing that we categorized as the best because it had a low  $\chi^2$  was in fact not the best. We therefore require the second best  $\chi^2$  pairing to have a  $\chi^2$  value. We set the cut point at 50. A comparison between data and Monte Carlo for this variable is shown in Fig 5.14.

## 5.9 Acceptance and Flux

The acceptance for the kaon decay modes was primarily calculated using the Monte Carlo simulation. The acceptance loss for individual cuts is shown in Table 5.1. The acceptance of signal events of the various signal modes as a fraction of decays in the fiducial region is shown in Table 5.3.

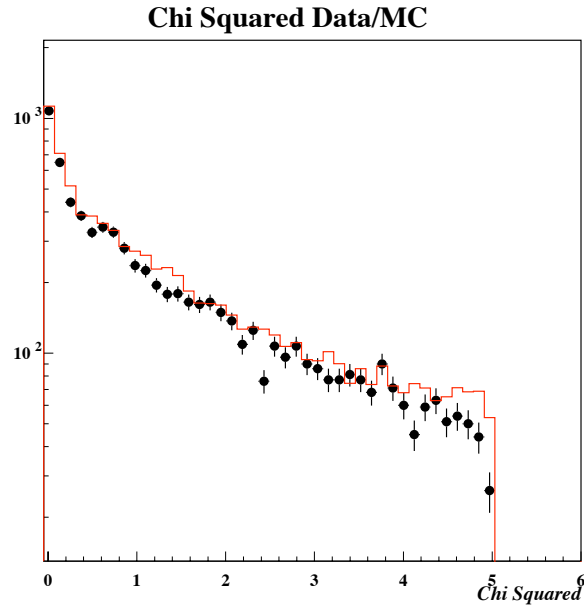


Figure 5.13: Comparison between data and Monte Carlo of  $\chi^2$  of vertex reconstruction. Plots are normalized by  $K_L \rightarrow \pi^0\pi^0$  signal box. Monte Carlo consists of  $K_L \rightarrow \pi^0\pi^0$  and  $K_L \rightarrow \pi^0\pi^0\pi^0$  events.

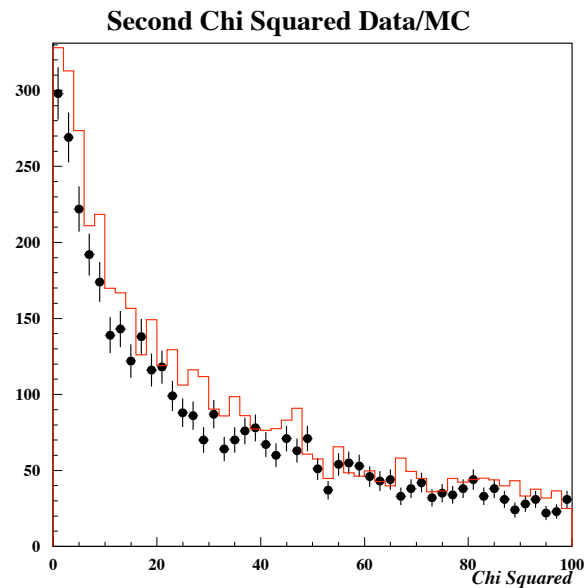


Figure 5.14: Comparison between data and Monte Carlo of  $\chi^2$  of the second best  $\pi^0$  pairing vertex reconstruction. Plots are normalized by  $K_L \rightarrow \pi^0\pi^0$  signal box. Monte Carlo consists of  $K_L \rightarrow \pi^0\pi^0$  and  $K_L \rightarrow \pi^0\pi^0\pi^0$  events.

### 5.9.1 Non-simulated Cuts

The Monte Carlo did not fully reproduce the behavior of several of the cuts. The primary cuts where this is the case are cuts which involve the timing behavior of the detector and the BA. These cuts are the BA veto, the CsI veto, the Gamma T.D.I., and the fusion neural net cut. We determine the effect of these cuts on acceptance from the data by comparing the number of  $K_L \rightarrow \pi^0\pi^0$  signal events with and without these cuts. This acceptance loss is then applied to the signal mode acceptance calculated with the simulated cuts. Table 5.2 shows the non-simulated acceptance loss.

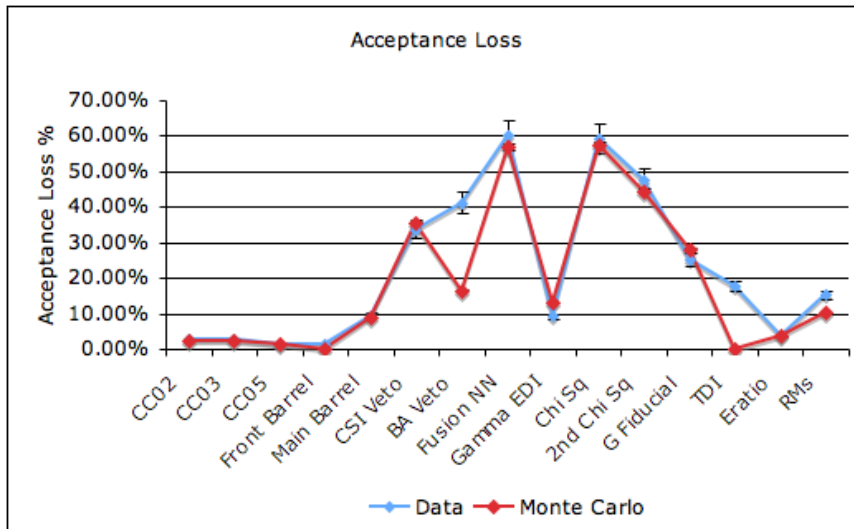


Figure 5.15:  $K_L \rightarrow \pi^0\pi^0$  acceptance loss from individual vetoes.

### 5.9.2 Flux

The flux of kaons which decayed in the fiducial region was calculated using both  $K_L \rightarrow \pi^0\pi^0$  and  $K_L \rightarrow \pi^0\pi^0\pi^0$ . After calculating the acceptance of these two modes, the number of observed events can be used to determine the flux. The values are shown in Table 5.2. We use both modes as a check on our acceptance calculations.

Cut	Cut Value	Acceptance Loss			Signal to Noise Ratio	
		$2\pi^0$		$2\pi^0\nu\bar{\nu}$	Data	MC
		Data	MC	MC	Data	MC
<i>Photon Vetoes</i>						
CC02	1 MeV	$(2.6 \pm 0.2)\%$	$(2.4 \pm 0.1)\%$	$(2.1 \pm 0.1)\%$	1.29	1.90
CC03	2.5 MeV	$(2.6 \pm 0.2)\%$	$(2.2 \pm 0.1)\%$	$(2.1 \pm 0.1)\%$	1.14	1.48
CC05	4 MeV	$(1.3 \pm 0.1)\%$	$(1.3 \pm 0.1)\%$	$(0.7 \pm 0.1)\%$	1.06	0.90
CsI Veto*	30 MeV	$(33.8 \pm 2.5)\%$	$(35.3 \pm 0.7)\%$	$(29.2 \pm 3.5)\%$	1.73	1.67
Main Barrel	2 MeV	$(9.5 \pm 0.8)\%$	$(8.9 \pm 0.2)\%$	$(6.5 \pm 0.8)\%$	1.27	1.76
Front Barrel	4 MeV	$(1.3 \pm 0.1)\%$	$(0.0 \pm 0.0)\%$	$(0.0 \pm 0.0)\%$	7.43	201.2
Back-Anti*		$(41.3 \pm 3.0)\%$	NA	NA	1.40	NA
<i>Gamma Quality</i>						
Gamma E.D.I.	0.8	$(9.2 \pm 0.7)\%$	$(12.9 \pm 0.3)\%$	$(11.7 \pm 1.4)\%$	1.29	1.54
Gamma T.D.I. *	2.0	$(17.8 \pm 1.4)\%$	NA	NA	1.10	NA
Fusion Neural Net *	0.75	$(60.3 \pm 4.1)\%$	$(56.9 \pm 1.0)\%$	$(49.1 \pm 5.8)\%$	1.32	1.03
Gamma Fiducial	17.5 and 90.0 cm	$(25.3 \pm 1.9)\%$	$(27.8 \pm 0.5)\%$	$(21.4 \pm 2.3)\%$	1.10	0.93
Gamma Energy Ratio	0.8	$(3.6 \pm 0.3)\%$	$(3.9 \pm 0.1)\%$	$(7.1 \pm 0.8)\%$	1.56	1.51
Gamma RMS	6.	$(15.2 \pm 1.2)\%$	$(10.1 \pm 0.2)\%$	$(10.1 \pm 1.1)\%$	1.15	1.02
<i>Reconstruction Quality</i>						
Best $\chi^2$	0.5	$(59.3 \pm 4.1)\%$	$(57.5 \pm 1.0)\%$	$(51.4 \pm 6.1)\%$	1.19	1.18
2 <sup>nd</sup> Best $\chi^2$	50.0	$(47.5 \pm 3.4)\%$	$(44.3 \pm 0.8)\%$	$(57.7 \pm 6.8)\%$	1.24	1.36

Table 5.1: Acceptance loss and signal to noise ratio for individual veto cuts. Signal to noise ratio of the cuts is calculated as the factor by which the ratio of  $K_L \rightarrow \pi^0\pi^0$  signal events to events in the Low  $P_T$  Low Mass region changes. \* Cuts with an asterisk are excluded from the flux calculation and their acceptance loss is determined from  $K_L \rightarrow \pi^0\pi^0$  data.

Normalization Mode	Acceptance MC	Acceptance Loss Non-Simulated Cuts	Flux
$K_L \rightarrow \pi^0 \pi^0$	$(1.49 \pm 0.01) \times 10^{-3}$	$(85.5 \pm 0.9)\%$	$(1.54 \pm 0.04) \times 10^9$
$K_L \rightarrow \pi^0 \pi^0 \pi^0$	$(1.31 \pm 0.03) \times 10^{-5}$	$(89.4 \pm 0.5)\%$	$(1.57 \pm 0.04) \times 10^9$

Table 5.2: Flux calculation and non-simulated cut acceptance loss.

The calculated flux from the two modes agrees within statistical error. We use the central value of  $K_L \rightarrow \pi^0 \pi^0$  for our calculations.

The acceptance of the signal mode is calculated primarily from the signal Monte Carlo. The acceptance loss for cuts which are not simulated are calculated from the acceptance loss in the data  $K_L \rightarrow \pi^0 \pi^0$  signal loss. The cuts which we derive the acceptance loss from data because they are not simulated are the back anti veto and the gamma T.D.I. cut. Additionally the CsI veto and the fusion neural network show significant discrepancies between data and Monte Carlo and produce significant differences in the flux between  $K_L \rightarrow \pi^0 \pi^0$  and  $K_L \rightarrow \pi^0 \pi^0 \pi^0$ . These cuts are removed when we are calculating the flux. With those four cuts removed, the flux calculated by each of these two modes agree with statistical error.

### 5.9.3 Signal Mode Acceptance

The acceptances for our various signal modes are calculated using Monte Carlo. The non-simulated cuts and those which have significant data-Monte Carlo discrepancies were removed and their effect on acceptance was determined by the use of the  $K_L \rightarrow \pi^0 \pi^0$  data. We use a flat phase space for the  $K_L \rightarrow \pi^0 \pi^0 \nu \bar{\nu}$  decays for this acceptance calculation. The acceptance for  $K_L \rightarrow \pi^0 \pi^0 P$  depends on the mass of the sgoldstino. This dependence is shown in Table 5.3 and Fig 5.16.

The acceptance for the  $K_L \rightarrow \pi^0 \pi^0 P$  is significantly higher than that for  $K_L \rightarrow \pi^0 \pi^0 \nu \bar{\nu}$ . This is due to higher  $P_T$  distribution, because there is only one unobservable

Signal Mode	Acceptance MC	Acceptance Loss Non-Simulated Cuts	Final Acceptance	Single Event Sensitivity
$K_L \rightarrow \pi^0 \pi^0 \nu \bar{\nu}$	$(3.68 \pm 0.16) \times 10^{-4}$	$(14.5 \pm 0.9)\%$	$(5.33 \pm 0.23) \times 10^{-5}$	$(1.21 \pm 0.06) \times 10^{-5}$
$K_L \rightarrow \pi^0 \pi^0 \nu \bar{\nu}$ Form Factor	$(3.79 \pm 0.20) \times 10^{-4}$	$(14.5 \pm 0.9)\%$	$(5.50 \pm 0.28) \times 10^{-5}$	$(1.18 \pm 0.07) \times 10^{-5}$
$K_L \rightarrow \pi^0 \pi^0 P$				
$M_P = 25\text{MeV}$	$(1.55 \pm 0.03) \times 10^{-2}$	$(14.5 \pm 0.9)\%$	$(2.24 \pm 0.04) \times 10^{-3}$	$(2.89 \pm 0.06) \times 10^{-7}$
$M_P = 50\text{MeV}$	$(1.48 \pm 0.03) \times 10^{-2}$	$(14.5 \pm 0.9)\%$	$(2.14 \pm 0.04) \times 10^{-3}$	$(3.02 \pm 0.09) \times 10^{-7}$
$M_P = 75\text{MeV}$	$(1.54 \pm 0.03) \times 10^{-2}$	$(14.5 \pm 0.9)\%$	$(2.24 \pm 0.04) \times 10^{-3}$	$(2.89 \pm 0.09) \times 10^{-7}$
$M_P = 100\text{MeV}$	$(1.46 \pm 0.03) \times 10^{-2}$	$(14.5 \pm 0.9)\%$	$(2.11 \pm 0.04) \times 10^{-3}$	$(3.06 \pm 0.09) \times 10^{-7}$
$M_P = 125\text{MeV}$	$(1.29 \pm 0.03) \times 10^{-2}$	$(14.5 \pm 0.9)\%$	$(1.86 \pm 0.05) \times 10^{-3}$	$(3.47 \pm 0.11) \times 10^{-7}$
$M_P = 150\text{MeV}$	$(9.82 \pm 0.22) \times 10^{-3}$	$(14.5 \pm 0.9)\%$	$(1.42 \pm 0.03) \times 10^{-3}$	$(4.55 \pm 0.15) \times 10^{-7}$
$M_P = 175\text{MeV}$	$(4.96 \pm 0.16) \times 10^{-3}$	$(14.5 \pm 0.9)\%$	$(7.19 \pm 0.23) \times 10^{-4}$	$(9.00 \pm 0.35) \times 10^{-7}$
$M_P = 200\text{MeV}$	$(9.05 \pm 0.67) \times 10^{-4}$	$(14.5 \pm 0.9)\%$	$(1.31 \pm 0.10) \times 10^{-4}$	$(4.93 \pm 0.38) \times 10^{-6}$

Table 5.3: Acceptance and single event sensitivity for the various signal modes.

particle rather than two which can cancel each others contributions to  $P_T$  .

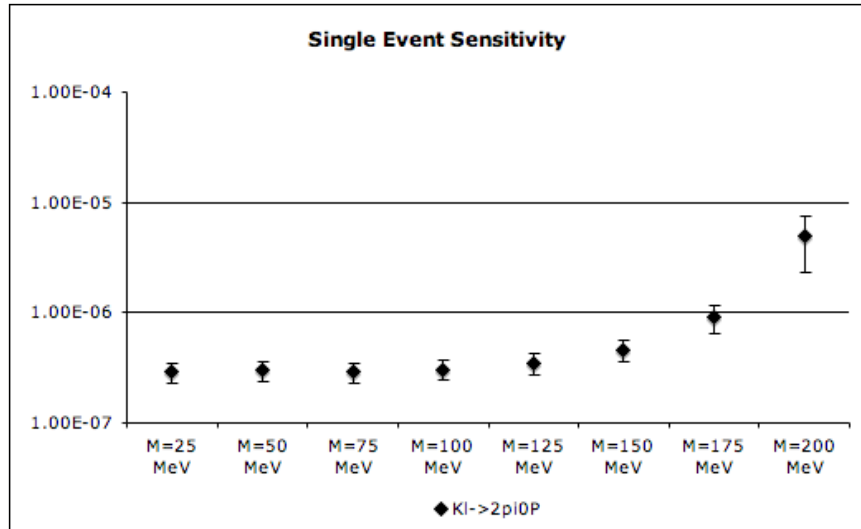


Figure 5.16: Single event sensitivity to  $K_L \rightarrow \pi^0 \pi^0 P$  as function of sgoldstino mass.

## CHAPTER 6

### BIFURCATION ANALYSIS TECHNIQUE

In this chapter I describe the bifurcation analysis procedure for background prediction that I use in the next chapter. The goal of the bifurcation analysis is to predict the level of background in the signal region using data without opening the signal box. I use the term cut to refer to a specific selection criteria. An event which passes a cut is selected an event which fails is thrown out. The procedure use the application of inverse cuts to properly measure the veto power of different sets of cuts while not opening the signal box. This technique was first developed in the stopped K experiments E787 and E949 at Brookhaven [21]. I begin with a derivation of the bifurcation analysis in the case of one background source and uncorrelated cuts, which is the technique used at the Brookhaven experiments. I then extend this to two background sources and a simple model of correlation between cuts. I cover the various derivations with a fair amount of algebraic detail.

#### 6.1 One Background Case

I begin discussing this method in the case of a single background source. Here a collection of setup cuts have been applied which eliminate all other sources of background. I use the term cut to refer to a specific selection criteria. An event that passes a cut is selected and an event which fails a cut is thrown out. I then want to know the amount of background in the signal region when I apply the Cuts A and B. The number of events we observe will be determined by the number of events before applying the cuts A and B (after applying the setup cuts),  $N_0$ , and the cut survival probability (CSP):

$$N_{\text{bkg}} = N_0 P(AB). \quad (6.1)$$

If events are considered to lie in a multi-dimensional space with a dimension corresponding to every variable on which can be used to make a cut. The set of cuts defines a multidimensional signal box which should be kept blinded. If two cuts show no correlation in the events that they cut, this implies that these two cuts are orthogonal in this space. The CSP can then be decomposed into  $P(AB) = P(A)P(B)$ .

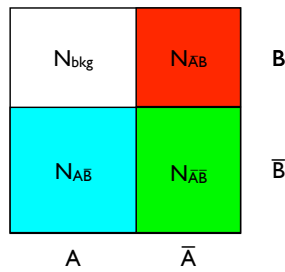


Figure 6.1: Schematic of background distribution in the cut space.

$$N_{\text{bkg}} = N_0 P(A)P(B) \quad (6.2)$$

This can be expanded into:

$$N_{\text{bkg}} = \frac{N_0^2 P(A)P(B)P(\bar{A})P(\bar{B})}{N_0 P(\bar{A})P(\bar{B})}. \quad (6.3)$$

Here  $\bar{A}$  and  $\bar{B}$  are the inverses of cuts  $A$  and  $B$ , events which pass cut  $A$  fail cut  $\bar{A}$ . Then this can be calculated from data based on the number of observed events in the

signal box under the different cut conditions:

$$N_{A\bar{B}} = N_0 P(A) P(\bar{B}), \quad (6.4)$$

$$N_{\bar{A}B} = N_0 P(B) P(\bar{A}), \quad (6.5)$$

$$N_{\bar{A}\bar{B}} = N_0 P(\bar{A}) P(\bar{B}). \quad (6.6)$$

Where  $N_{A\bar{B}}$  is the number of background events observed with the application of cut A and the inverse of cut B.  $N_{\bar{A}B}$  is the observed background events with the inverse of cut A and cut B applied.  $N_{\bar{A}\bar{B}}$  is the count when the inverse of both A and B are applied. All of these values are outside the signal box defined in the multi-dimensional cut space allowing us to predict the background without opening the box:

$$N_{\text{bkg}} = \frac{N_{A\bar{B}} N_{\bar{A}B}}{N_{\bar{A}\bar{B}}}. \quad (6.7)$$

The procedure goes as follows. First, apply setup cuts to the data, the number of events in the signal box is  $N_0$ . The setup cuts should remove any background sources other than the ones that are being considered. Then the group of cuts  $A$  is applied, while requiring that events don't pass the set of cuts  $B$ . Only events which are outside the signal box in the multidimensional space remain, because the inverse of cut  $B$  has been applied. The number of events which pass these sets of cuts is  $N_{A\bar{B}}$ . Repeating the same procedure in reverse applying the set of cuts  $B$  and the inverse of  $A$  produces  $N_{\bar{A}B}$ . Finally, applying the inverse of both cuts A and B gives  $N_{\bar{A}\bar{B}}$ . These values are combined in Eqn. 6.7 to produce the background prediction.

Eqn. 6.7 predicts no background events, if  $N_{A\bar{B}}$  or  $N_{\bar{A}B}$  are zero. This can be true for one of three reasons:  $N_0 = 0$ ,  $P(A)$  or  $P(B)=0$ , or  $P(\bar{A})$  or  $P(\bar{B}) = 0$ . The first two possibilities are what we expect and reflect cases where there should

be no background events. The third possibility is more problematic. When  $P(\bar{A})$  or  $P(\bar{B}) = 0$ ,  $N_{\bar{A}\bar{B}}$  should also be zero, but statistical fluctuations may prevent that from being true. This condition results from a poor choice of cuts where one cut eliminates almost no background events. If possible a different choice of cuts for  $A$  and  $B$  should be made.

## 6.2 Two Background Case

Multiple background sources can introduce a specific kind of correlation between the cuts. The effect this correlation has on the background can be accounted for.

### 6.2.1 Derivation

The previous derivation applied in the case of a single background source. However, if the background is made up of two different background sources,  $N_0 = N_1 + N_2$ , which have different cut survival probabilities then this is not correct. If that is the case then the terms defined by Eqns. 6.3 and 6.5-6.6 instead have the form:

$$N_{\text{bkg}} = N_1 P_1(A) P_1(B) + N_2 P_2(A) P_2(B), \quad (6.8)$$

$$N_{A\bar{B}} = N_1 P_1(A) P_1(\bar{B}) + N_2 P_2(A) P_2(\bar{B}), \quad (6.9)$$

$$N_{\bar{A}B} = N_1 P_1(B) P_1(\bar{A}) + N_2 P_2(B) P_2(\bar{A}), \quad (6.10)$$

$$N_{\bar{A}\bar{B}} = N_1 P_1(\bar{A}) P_1(\bar{B}) + N_2 P_2(\bar{A}) P_2(\bar{B}). \quad (6.11)$$

This introduces a cross-term in the previous calculation of  $N_{\text{bkg}}$ . I begin by

substituting the above definitions into the solution for the one background case:

$$\frac{N_{A\bar{B}}N_{\bar{A}B}}{N_{\bar{A}\bar{B}}} = \frac{[N_1P_1(A)P_1(\bar{B}) + N_2P_2(A)P_2(\bar{B})][N_1P_1(B)P_1(\bar{A}) + N_2P_2(B)P_2(\bar{A})]}{N_{\bar{A}\bar{B}}}. \quad (6.12)$$

I can expand the numerator into:

$$\begin{aligned} N_{A\bar{B}}N_{\bar{A}B} &= N_1^2P_1(A)P_1(\bar{A})P_1(B)P_1(\bar{B}) \\ &\quad + N_1N_2[P_1(A)P_2(\bar{A})P_2(B)P_1(\bar{B}) + P_2(A)P_1(\bar{A})P_1(B)P_2(\bar{B})] \\ &\quad + N_2^2P_2(A)P_2(\bar{A})P_2(B)P_2(\bar{B}). \end{aligned} \quad (6.13)$$

I multiply  $N_{\text{bkg}}$  by  $N_{\bar{A}\bar{B}}$  to allow us to find the difference of Eqn. 6.12 and  $N_{\text{bkg}}$ :

$$\begin{aligned} N_{\text{bkg}}N_{\bar{A}\bar{B}} &= [N_1P_1(A)P_1(B) + N_2P_2(A)P_2(B)][N_1P_1(\bar{A})P_1(\bar{B}) + N_2P_2(\bar{A})P_2(\bar{B})] \\ &= N_1^2P_1(A)P_1(\bar{A})P_1(B)P_1(\bar{B}) \\ &\quad + N_1N_2[P_1(A)P_2(\bar{A})P_1(B)P_1(\bar{B}) + P_2(A)P_1(\bar{A})P_2(B)P_1(\bar{B})] \\ &\quad + N_2^2P_2(A)P_2(\bar{A})P_2(B)P_2(\bar{B}). \end{aligned} \quad (6.14)$$

Comparing Eqns. 6.13 and 6.14 and dividing by  $N_{\bar{A}\bar{B}}$ , I find:

$$\begin{aligned}
\frac{N_{A\bar{B}}N_{\bar{A}B}}{N_{\bar{A}\bar{B}}} &= N_{\text{bkg}} \\
&+ \frac{N_1N_2}{N_{\bar{A}\bar{B}}} \left[ P_1(A)P_2(\bar{A})P_2(B)P_1(\bar{B}) \right. \\
&+ P_2(A)P_1(\bar{A})P_1(B)P_2(\bar{B}) \\
&- P_1(A)P_2(\bar{A})P_1(B)P_2(\bar{B}) \\
&\left. - P_2(A)P_1(\bar{A})P_2(B)P_1(\bar{B}) \right].
\end{aligned} \tag{6.15}$$

The cross term vanishes if one of the following conditions are met, if  $P_1(A) = P_2(A)$  and  $P_1(B) = P_2(B)$ . In this case for the purposes of the cuts, the two background sources are the same.

I can simplify the cross term by rewriting the CSP's of the inverse cuts in terms of the CSP's of the cuts,  $P_i(\bar{A}) = 1 - P_i(A)$ . Each element of the cross term has the same structure which can be expanded to:

$$\begin{aligned}
P_i(A)P_j(\bar{A})P_k(B)P_\ell(\bar{B}) &= P_i(A)P_k(B)(1 - P_j(A))(1 - P_\ell(B)) \\
&= P_i(A)P_k(B)(1 - P_j(A) - P_\ell(B) + P_j(A)P_\ell(B)) \\
&= P_i(A)P_k(B) - P_i(A)P_j(A)P_k(B) - P_i(A)P_k(B)P_\ell(B) \\
&\quad + P_i(A)P_j(A)P_k(B)P_\ell(B).
\end{aligned} \tag{6.16}$$

Summing the elements of the cross term cancels out everything except the terms

with two CSPs:

$$\begin{aligned}
\frac{N_{A\bar{B}}N_{\bar{A}B}}{N_{\bar{A}\bar{B}}} &= N_{\text{bkg}} \\
&+ \frac{N_1N_2(P_1(A)P_2(B) + P_2(A)P_1(B) - P_1(A)P_1(B) - P_2(A)P_2(B))}{N_{\bar{A}\bar{B}}} \\
&= N_{\text{bkg}} - \frac{N_1N_2(P_2(A) - P_1(A))(P_2(B) - P_1(B))}{N_{\bar{A}\bar{B}}}.
\end{aligned} \tag{6.17}$$

I can further simplify the cross term by defining  $\Delta_A = P_2(A) - P_1(A)$  and  $\Delta_B = P_2(B) - P_1(B)$ :

$$N_{\text{bkg}} = \frac{N_{A\bar{B}}N_{\bar{A}B}}{N_{\bar{A}\bar{B}}} + \frac{N_1N_2}{N_{\bar{A}\bar{B}}}\Delta_A\Delta_B. \tag{6.18}$$

The second term is not the contribution from the second background source. Instead it is a correction to the prediction from the first term which includes events of both background types. Secondly, the values of  $N_1$ ,  $N_2$ ,  $\Delta_A$ , and  $\Delta_B$  are not directly accessible in data without opening the signal box. These can either be derived from Monte Carlo or from other regions in signal space.

### 6.2.2 Properties of the Two Background Solution

As a check on my derivation, I examine some of the properties of this solution. Eqn. 6.18 has the reasonable property that it is symmetric with respect to the definitions of the cuts  $A$  and  $B$  and the backgrounds 1 and 2.

The correction term can be either positive or negative. However, the total  $N_{\text{bkg}}$  will not be negative. The correction term will have it's maximum negative value when  $\Delta_A = 1$  and  $\Delta_B = -1$  or  $\Delta_A = -1$  and  $\Delta_B = 1$ . Under these conditions,  $N_{\bar{A}\bar{B}} = 0$  and  $N_{\text{bkg}}$  is undefined. I therefore want to study  $N_{\text{bkg}}$ 's behavior as it approaches this limit. I begin by setting  $\Delta_B = -1$  and studying the limit as  $\Delta_A \rightarrow 1$ . In this

case cut  $B$  removes Background 1 completely, but the Background 1 events which survive  $\bar{A}B$  still contribute to the prediction produced by Eqn. 6.7. Since 6.18 is invariant with respect to the interchange of cuts A and B and backgrounds 1 and 2 this is sufficient to prove it for all cases.

The condition that  $\Delta_B = -1$  sets what values the CSP's of B can take:

$$P_1(B) = P_2(\bar{B}) = 0, \quad (6.19)$$

$$P_2(B) = P_1(\bar{B}) = 1. \quad (6.20)$$

Substituting these values into the definitions for the number of events under different cut conditions simplifies these values:

$$\begin{aligned} N_{A\bar{B}} &= N_1 P_1(A) P_1(\bar{B}) + N_2 P_2(A) P_2(\bar{B}) \\ &= N_1 P_1(A)[0] + N_2 P_2(A)[1] \\ &= N_2 P_2(A), \end{aligned} \quad (6.21)$$

$$\begin{aligned} N_{\bar{A}B} &= N_1 P_1(\bar{A}) P_1(B) + N_2 P_2(\bar{A}) P_2(B) \\ &= N_1 P_1(\bar{A})[1] + N_2 P_2(\bar{A})[0] \\ &= N_1 P_1(\bar{A}) = N_1(1 - P_1(A)), \end{aligned} \quad (6.22)$$

$$\begin{aligned} N_{\bar{A}\bar{B}} &= N_1 P_1(\bar{A}) P_1(\bar{B}) + N_2 P_2(\bar{A}) P_2(\bar{B}) \\ &= N_1 P_1(\bar{A})[0] + N_2 P_2(\bar{A})[1] \\ &= N_2 P_2(\bar{A}) = N_2(1 - P_2(A)). \end{aligned} \quad (6.23)$$

I then substitute these values into Eqn. 6.18:

$$N_{\text{bkg}} = \frac{N_2 P_2(A) N_1 (1 - P_1(A))}{N_2 (1 - P_2(A))} + \frac{N_1 N_2 (P_2(A) - P_1(A))[-1]}{N_2 (1 - P_2(A))}. \quad (6.24)$$

Adding the two terms together, I find:

$$\begin{aligned}
N_{\text{bkg}} &= \frac{N_1 P_2(A) - N_1 P_2(A) P_1(A) - N_1 P_2(A) + N_1 P_1(A)}{1 - P_2(A)} \\
&= \frac{N_1 P_1(A) - N_1 P_2(A) P_1(A)}{1 - P_2(A)} \\
&= \frac{N_1 P_1(A)(1 - P_2(A))}{1 - P_2(A)} \\
&= N_1 P_1(A).
\end{aligned} \tag{6.25}$$

As  $\Delta_A \rightarrow 1$ ,  $P_1(A) \rightarrow 0$ . Therefore the  $N_{\text{bkg}}$  goes to 0. This indicates that  $N_{\text{bkg}}$  is never has a non-physical negative value.

### 6.2.3 Interpretation of Two Background Solution

It may seem counterintuitive that two backgrounds cannot be combined simply. This can best be understood as the second background introducing an implicit correlation.

As an example, consider two backgrounds which individually have no correlation between cut A and cut B, but do have different cut survival probabilities. If  $P_1(A) = 0.75$  and  $P_1(B) = 0.75$ , while  $P_2(A) = 0.25$  and  $P_2(B) = 0.25$  then the resulting combination of the two backgrounds will have a correlation. Events which survive cut A are have a greater chance to survive cut B, because events which survive cut A are more likely to be part of Background 1. The events that don't survive cut A are less likely to survive cut B, because they are more likely to be part of background 2. Therefore there is a correlation between cuts A and B, even though for the individual backgrounds they are uncorrelated.

The values of  $N_1$ ,  $N_2$ ,  $\Delta_A$ , and  $\Delta_B$  are not directly accessible in data without opening the signal box. There are two options either derive these values from Monte Carlo or from other regions in signal space.  $N_1$  and  $N_2$  generally will require some

alternative way of predicting one of the backgrounds and the value of  $N_0$ , the total number of background after setup cuts. This raises the question, whether determining  $N_0$  biases the analysis. From  $N_0$  and the other observed background numbers,  $N_{A\bar{B}}$ ,  $N_{\bar{A}B}$ , and  $N_{\bar{A}\bar{B}}$ , it is possible to effectively open the box and count  $N_{\text{bkg}}$ . Determining  $\Delta_A$  and  $\Delta_B$  also requires additional input. Their values can be derived from either Monte Carlo or data outside the signal region.

#### 6.2.4 A Second Derivation

What follows is a second method of deriving the two background prediction. It is in my opinion less intuitive, but others may find it useful. It begins by defining the cut survival probabilities for the combination of the two backgrounds and how they relate to the CSP's of the individual backgrounds:

$$N_{\text{bkg}} = N_0 P_0(AB). \quad (6.26)$$

$P_0(AB)$  cannot be simply expanded into  $P_0(A)$  and  $P_0(B)$ , instead they are defined as:

$$P_0(AB) = \frac{N_1 P_1(AB) + N_2 P_2(AB)}{N_0}, \quad (6.27)$$

$$P_0(A) = \frac{N_1 P_1(A) + N_2 P_2(A)}{N_0}, \quad (6.28)$$

$$P_0(B) = \frac{N_1 P_1(B) + N_2 P_2(B)}{N_0}. \quad (6.29)$$

The product of  $P_0(A)$  and  $P_0(B)$  is:

$$P_0(A)P_0(B) = \frac{N_1^2 P_1(A)P_1(B) + N_1 N_2 (P_1(A)P_2(B) + P_2(A)P_1(B)) + N_2^2 P_2(A)P_2(B)}{N_0^2}. \quad (6.30)$$

I multiply the numerator and denominator of Eqn. 6.27 by  $N_0$ :

$$P_0(AB) = \frac{N_1^2 P_1(AB) + N_1 N_2 (P_1(AB) + P_2(AB)) + N_2^2 P_2(AB)}{N_0^2}. \quad (6.31)$$

$P_1(AB)$  and  $P_2(AB)$  should behave as simple probabilities without correlation, and can be simply expanded as  $P_i(AB) = P_i(A)P_i(B)$ . Applying this expansion to Eqn. 6.31 gives us:

$$P_0(AB) = \frac{N_1^2 P_1(A)P_1(B) + N_1 N_2 (P_1(A)P_1(B) + P_2(A)P_2(B)) + N_2^2 P_2(A)P_2(B)}{N_0^2}. \quad (6.32)$$

I then find the difference between Eqn.'s 6.30 and 6.32:

$$P_0(AB) - P_0(A)P_0(B) = \frac{N_1 N_2 (P_1(A)P_1(B) + P_2(A)P_2(B) - P_1(A)P_2(B) - P_2(A)P_1(B))}{N_0^2}. \quad (6.33)$$

I can further simplify the difference by again introducing  $\Delta_A = P_2(A) - P_1(A)$  and

$$\Delta_A = P_2(B) - P_1(B) :$$

$$P_0(AB) - P_0(A)P_0(B) = \frac{N_1 N_2 \Delta_A \Delta_A}{N_0^2}. \quad (6.34)$$

A similar calculation can be done for each combination of the cuts  $A, B$  and their inverses:

$$N_{\text{bkg}} = N_0 P(AB) = N_0 P_0(A)P_0(B) + \frac{N_1 N_2 \Delta_A \Delta_B}{N_0}, \quad (6.35)$$

$$N_{A\bar{B}} = N_0 P(A\bar{B}) = N_0 P_0(A)P_0(\bar{B}) - \frac{N_1 N_2 \Delta_A \Delta_B}{N_0}, \quad (6.36)$$

$$N_{\bar{A}B} = N_0 P(\bar{A}B) = N_0 P_0(\bar{A})P_0(B) - \frac{N_1 N_2 \Delta_A \Delta_B}{N_0}, \quad (6.37)$$

$$N_{\bar{A}\bar{B}} = N_0 P(\bar{A}\bar{B}) = N_0 P_0(\bar{A})P_0(\bar{B}) + \frac{N_1 N_2 \Delta_A \Delta_B}{N_0}. \quad (6.38)$$

I define  $c \equiv \frac{N_1 N_2 \Delta_A \Delta_B}{N_0}$ . To find the correction to the one background solution, I follow the derivation in the one background case and expand  $N_{\text{bkg}}$ :

$$N_{\text{bkg}} = N_0 P_0(AB) = N_0 P_0(A)P_0(B) + c \quad (6.39)$$

$$= \frac{N_0^2 P_0(A)P_0(B)P_0(\bar{A})P_0(\bar{B})}{N_0 P_0(\bar{A})P_{\bar{B}}} + c \quad (6.40)$$

$$= \frac{(N_{A\bar{B}} + c)(N_{\bar{A}B} + c)}{N_{\bar{A}\bar{B}} - c} + c. \quad (6.41)$$

I wish to find a correction to the original solution for the one background case:

$$N_{\text{bkg}} = \frac{N_{A\bar{B}} N_{\bar{A}B}}{N_{\bar{A}\bar{B}}} + \left( \frac{(N_{A\bar{B}} + c)(N_{\bar{A}B} + c)}{N_{\bar{A}\bar{B}} - c} - \frac{N_{A\bar{B}} N_{\bar{A}B}}{N_{\bar{A}\bar{B}}} \right) + c. \quad (6.42)$$

To simplify the derivation I first calculate the term in the parentheses in Eqn. 6.42:

$$\frac{(N_{A\bar{B}} + c)(N_{\bar{A}B} + c)}{N_{\bar{A}\bar{B}} - c} - \frac{N_{A\bar{B}}N_{\bar{A}B}}{N_{\bar{A}\bar{B}}} = \frac{c(N_{A\bar{B}}N_{\bar{A}\bar{B}} + N_{\bar{A}B}N_{\bar{A}\bar{B}} + N_{A\bar{B}}N_{\bar{A}B}) + c^2N_{\bar{A}\bar{B}}}{(N_{\bar{A}\bar{B}} - c)N_{\bar{A}\bar{B}}}. \quad (6.43)$$

I now add  $c$  to both sides of Equation 6.43:

$$\frac{(N_{A\bar{B}} + c)(N_{\bar{A}B} + c)}{N_{\bar{A}\bar{B}} - c} - \frac{N_{A\bar{B}}N_{\bar{A}B}}{N_{\bar{A}\bar{B}}} + c = \frac{c(N_{A\bar{B}}N_{\bar{A}\bar{B}} + N_{\bar{A}B}N_{\bar{A}\bar{B}} + N_{A\bar{B}}N_{\bar{A}B}) + c^2N_{\bar{A}\bar{B}}}{(N_{\bar{A}\bar{B}} - c)N_{\bar{A}\bar{B}}} + c \quad (6.44)$$

$$= \frac{c(N_{A\bar{B}}N_{\bar{A}\bar{B}} + N_{\bar{A}B}N_{\bar{A}\bar{B}} + N_{A\bar{B}}N_{\bar{A}B} + N_{\bar{A}\bar{B}}^2)}{(N_{\bar{A}\bar{B}} - c)N_{\bar{A}\bar{B}}} \quad (6.45)$$

$$= \frac{c((N_{A\bar{B}}N_{\bar{A}\bar{B}} + N_{\bar{A}\bar{B}}N_{\bar{A}\bar{B}}) + (N_{A\bar{B}}N_{\bar{A}B} + N_{\bar{A}\bar{B}}N_{\bar{A}B}))}{(N_{\bar{A}\bar{B}} - c)N_{\bar{A}\bar{B}}}. \quad (6.46)$$

I now introduce  $N_{\bar{A}} = N_{\bar{A}B} + N_{\bar{A}\bar{B}}$  and  $N_{\bar{B}} = N_{A\bar{B}} + N_{\bar{A}\bar{B}}$ . These are the number of events observed when only  $\bar{A}$  or  $\bar{B}$  are applied:

$$= \frac{c(N_{\bar{B}}N_{\bar{A}\bar{B}} + N_{\bar{A}\bar{B}}N_{\bar{B}})}{(N_{\bar{A}\bar{B}} - c)N_{\bar{A}\bar{B}}} \quad (6.47)$$

$$= \frac{cN_{\bar{A}}N_{\bar{B}}}{(N_{\bar{A}\bar{B}} - c)N_{\bar{A}\bar{B}}}. \quad (6.48)$$

Equation 6.48 gives the value of the correction to one background case:

$$N_{\text{bkg}} = \frac{N_{A\bar{B}}N_{\bar{A}B}}{N_{\bar{A}\bar{B}}} + \frac{cN_{\bar{A}}N_{\bar{B}}}{(N_{\bar{A}\bar{B}} - c)N_{\bar{A}\bar{B}}}. \quad (6.49)$$

The following identities allow us to simplify the above equation:

$$N_{\bar{A}\bar{B}} - c = N_0 P_0(A) P_0(B), \quad (6.50)$$

$$N_{\bar{A}} = N_0 P_0(A), \quad (6.51)$$

$$N_{\bar{B}} = N_0 P_0(B). \quad (6.52)$$

Substituting these in:

$$N_{\text{bkg}} = \frac{N_{A\bar{B}} N_{\bar{A}B}}{N_{\bar{A}\bar{B}}} + \frac{N_0 c}{N_{\bar{A}\bar{B}}}. \quad (6.53)$$

I expand out the value of  $c$ :

$$N_{\text{bkg}} = \frac{N_{A\bar{B}} N_{\bar{A}B}}{N_{\bar{A}\bar{B}}} + \frac{N_1 N_2 \Delta_A \Delta_B}{N_{\bar{A}\bar{B}}}. \quad (6.54)$$

This is the solution I originally derived in Section 6.2.

### 6.3 Cut Correlation

The criteria for cuts A and B to be uncorrelated is that the probability of an event being cut by A is the same whether or not it is cut by B. One measure of the correlation is the correlation coefficient [22]. A and B are random variables with values of either 0 or 1. They are 1 when an event passes the cut and 0 when the event is removed by the cut. Their CSP's are then the expectation values of the A and B:

$$\rho = \text{Cor}(A, \bar{B}) = \frac{\text{Cov}(A, \bar{B})}{\sqrt{\text{Var}(A)\text{Var}(\bar{B})}} = \frac{P(A\bar{B}) - P(A)P(\bar{B})}{\sigma_A \sigma_{\bar{B}}}. \quad (6.55)$$

Here,  $\sigma_A$  and  $\sigma_{\bar{B}}$  are the variances of the variables  $A$  and  $\bar{B}$  and not the variances of  $P(A)$  or  $P(\bar{B})$ :

$$\sigma_A^2 = \frac{1}{N_0} \sum (A_i - \langle A \rangle)^2 = \frac{N_A(1 - P(A))^2 + (N_0 - N_A)P(A)^2}{N_0}. \quad (6.56)$$

The statistical correlation ranges between -1 and 1. If the two cuts are uncorrelated then the statistical correlation is 0. It is not necessarily the case that they are uncorrelated if the statistical correlation is 0. It is generally considered that statistical correlations of less than 0.1 are uncorrelated.

### 6.3.1 Impact of Cut Correlation

The statistical correlation is a general measure of correlation, but without a model of how the cuts are correlated it is difficult to derive a correction to the background prediction. I describe a case where the cuts are weakly correlated to establish the impact correlation will have on the background prediction. Since the cuts are correlated, the prior probability, which specifies the state of the other cut, must be introduced. In this model the CSPs have small differences between posterior and prior probabilities.

I begin by specifying the background values in terms of the CSP's, which now specify the dependence on both cut conditions:

$$N_{\text{bkg}} = N_0 P(A|B)P(B) = N_0 P(A)P(B|A), \quad (6.57)$$

$$N_{A\bar{B}} = N_0 P(A|\bar{B})P(\bar{B}) = N_0 P(A)P(\bar{B}|A), \quad (6.58)$$

$$N_{\bar{A}B} = N_0 P(\bar{A}|B)P(B) = N_0 P(\bar{A})P(B|\bar{A}), \quad (6.59)$$

$$N_{\bar{A}\bar{B}} = N_0 P(\bar{A}|\bar{B})P(\bar{B}) = N_0 P(\bar{A})P(\bar{B}|\bar{A}). \quad (6.60)$$

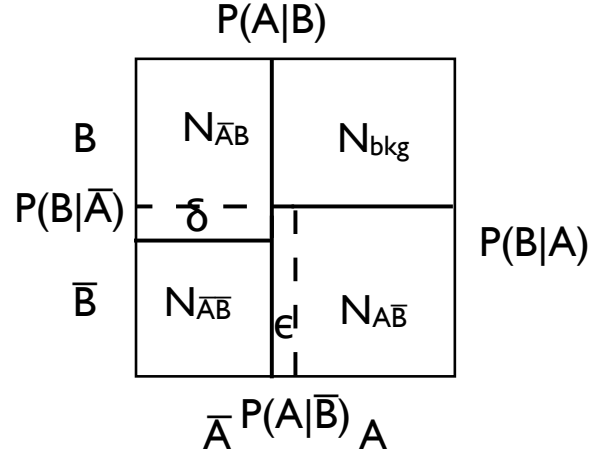


Figure 6.2: Cut space with correlated cuts.

I proceed in the same fashion as for the two background case and substitute these definitions into the solution (Equation 6.7) for the single background uncorrelated case:

$$\frac{N_{A\bar{B}}N_{\bar{A}B}}{N_{\bar{A}\bar{B}}} = \frac{N_0^2 P(A|\bar{B})P(\bar{B})P(\bar{A}|B)P(B)}{N_0 P(\bar{A}|\bar{B})P(\bar{B})}. \quad (6.61)$$

I am interested in the case where the correlations are small, so I define:

$$P(A|\bar{B}) = P(A|B) - \epsilon, \quad (6.62)$$

$$P(\bar{A}|\bar{B}) = P(\bar{A}|B) + \epsilon, \quad (6.63)$$

$$P(B|\bar{A}) = P(B|A) - \delta, \quad (6.64)$$

$$P(\bar{B}|\bar{A}) = P(\bar{B}|A) + \delta. \quad (6.65)$$

The values of  $\epsilon$  and  $\delta$  should be small compared to those of the CSP's. I substitute these definitions into Eqn 6.61:

$$\frac{N_{A\bar{B}}N_{\bar{A}B}}{N_{\bar{A}\bar{B}}} = \frac{N_0 P(\bar{A}|B)(P(A|B) - \epsilon)P(B)}{P(\bar{A}|B) + \epsilon}, \quad (6.66)$$

$$\frac{N_{A\bar{B}}N_{\bar{A}B}}{N_{\bar{A}\bar{B}}} = \frac{N_0(P(A|B)P(B) - \epsilon P(B))}{1 + \frac{\epsilon}{P(\bar{A}|B)}}. \quad (6.67)$$

If I assume the  $\epsilon$  term in the denominator is small, I can then expand this result as:

$$\begin{aligned} \frac{N_{A\bar{B}}N_{\bar{A}B}}{N_{\bar{A}\bar{B}}} &\approx (N_0(P(A|B)P(B) - \epsilon P(B))) \\ &\times \left(1 - \frac{\epsilon}{P(\bar{A}|B)} + \frac{\epsilon^2}{P(\bar{A}|B)^2} + \mathcal{O}(\epsilon^3)\right). \end{aligned} \quad (6.68)$$

Multiplying this out and keeping the second order terms of  $\epsilon$  gives the equation

$$\begin{aligned} \frac{N_{A\bar{B}}N_{\bar{A}B}}{N_{\bar{A}\bar{B}}} &= N_0P(A|B)P(B) - \epsilon N_0\left(P(B) + \frac{P(A|B)P(B)}{P(\bar{A}|B)}\right) \\ &+ \epsilon^2 N_0\left(\frac{P(B)}{P(\bar{A}|B)} + \frac{P(A|B)P(B)}{P(\bar{A}|B)^2}\right). \end{aligned} \quad (6.69)$$

The first term with no  $\epsilon$  factors is  $N_{\text{bkg}}$ . The condition for the correlations to have a negligible impact on the background prediction is that the  $\epsilon$  terms be much smaller than  $\frac{N_{A\bar{B}}N_{\bar{A}B}}{N_{\bar{A}\bar{B}}}$ :

$$\begin{aligned} N_{\text{bkg}} &= \frac{N_{A\bar{B}}N_{\bar{A}B}}{N_{\bar{A}\bar{B}}} + \epsilon N_0P(B)\left(1 + \frac{P(A|B)}{P(\bar{A}|B)}\right) \\ &- \epsilon^2 N_0\frac{P(B)}{P(\bar{A}|B)}\left(1 + \frac{P(A|B)}{P(\bar{A}|B)}\right). \end{aligned} \quad (6.70)$$

I can rearrange Eqn 6.70 to find correction terms to account for the correlation. These terms however, require opening the signal box to know the correct values of the CSP's. I can approximate these values with less knowledge, under the assumption that the

number of events in the signal box is small:

$$P(B) = \frac{N_{AB} + N_{\bar{A}B}}{N_0}, \quad (6.71)$$

$$P(B) \approx \frac{N_{\bar{A}B}}{N_0}, \quad (6.72)$$

$$\frac{P(A|B)}{P(\bar{A}|B)} = \frac{\frac{N_{AB}}{N_B}}{\frac{N_{\bar{A}B}}{N_B}} \approx \frac{N_{\text{pred}}}{N_{\bar{A}B}}. \quad (6.73)$$

These approximations give us first order correction of:

$$C_\epsilon = \epsilon N_{\bar{A}B} \left(1 + \frac{N_{\text{pred}}}{N_{\bar{A}B}}\right). \quad (6.74)$$

One particular aspect of the impact of the prediction on the cut correlation is its dependance on the value of  $N_0$ . This leads to two competing forces in optimizing the division of cuts into the setup cuts and the bifurcation cuts. From the perspective of minimizing statistical error in the bifurcation prediction, one would like a large value for  $N_0$  with powerful cuts for cut  $A$  and  $B$ , so that the statistical errors on the terms of Eqn. 6.7 are small. On the other hand, a large  $N_0$  means the prediction is sensitive to small correlations between the cuts.

## 6.4 Discussion

The bifurcation analysis technique allows us to produce data driven background predictions while still maintaining a blind analysis. In this chapter I have shown how to extend the bifurcation analysis to the case of two background sources and correlated cuts. The primary purpose that we will use them for is to estimate errors on the one background, uncorrelated cut analysis. Properly correcting for multiple back-

ground sources and cut correlations requires the input of Monte Carlo or applying cut probability information from background regions to the signal box which is poorly understood or has high statistical uncertainties.

# CHAPTER 7

## TOY MODEL OF THE BIFURCATION ANALYSIS TECHNIQUE

In this chapter I describe the application of the bifurcation analysis technique to a toy model. I utilize the Mathematica software package to simulate this system [23].

### 7.1 The Model

Each event consists of four variables. Two kinematic variables,  $p$  and  $x$  which are used to describe the signal region and two cut variables,  $a$  and  $b$  which will be used to define the cuts. All of these variables range from 0 to 1.

We define 2 different types of events: background 1 and background 2. The probability distribution function of each variable for the two background types is shown in Table 7.1. They both have  $x$  variables with uniform distributions between 0 and 1. Their  $p$ 's have uniform distributions between 0 and  $x$  for Background 1 and between 0 and  $1 - x$  for Background 2. Background 1 has an uniform distribution of  $a$  between 0 and 1 and variable  $b$  has a linearly decreasing density with values between 0 and 1. Background 2's  $a$  distribution is a linearly decreasing density with values between 0 and 1 and an uniform distribution between 0 and 1 for  $b$ . The distributions of the kinematic variables  $p$  and  $x$  are shown in Fig 7.1. We define a signal region by specifying the allowed kinematic variables:  $0.25 < x < 0.75$  and  $0.25 < p < 0.75$ .

Background	$x$	$p$
1	$f(x) = 1, x \in (0, 1]$ $f(x) = 0, x \notin (0, 1]$	$f(p) = 1/x, p \in [0, x]$ $f(p) = 0, p \notin [0, x]$
2	$f(x) = 1, x \in [0, 1]$ $f(x) = 0, x \notin [0, 1]$	$f(p) = 1/(1-x), p \in [0, 1-x]$ $f(p) = 0, p \notin [0, 1-x]$

Background	$a$	$b$
1	$f(a) = 1, a \in [0, 1]$ $f(a) = 0, a \notin [0, 1]$	$f(b) = 1-b, b \in [0, 1]$ $f(b) = 0, b \notin [0, 1]$
2	$f(a) = 1-a, a \in [0, 1]$ $f(a) = 0, a \notin [0, 1]$	$f(b) = 1, b \in [0, 1]$ $f(b) = 0, b \notin [0, 1]$

Table 7.1: Probability distribution functions for the variables of each event type in the Toy Model.

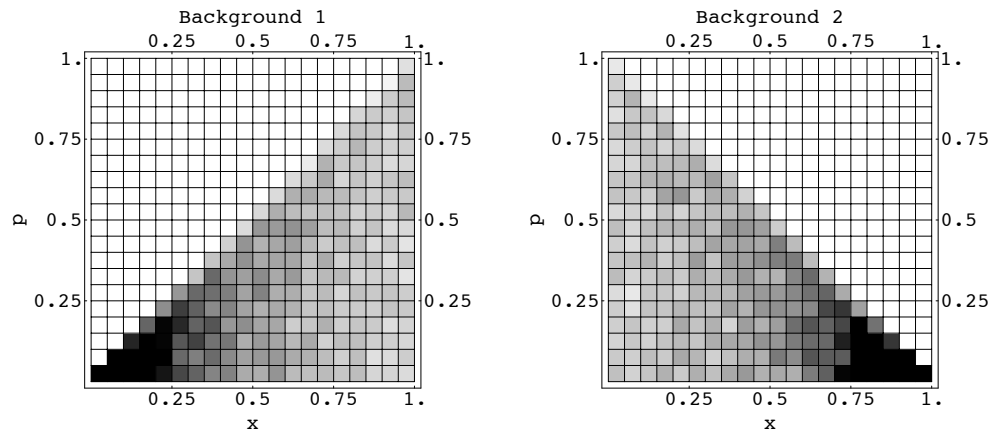


Figure 7.1: Kinematic variable distributions for Backgrounds 1 and 2.

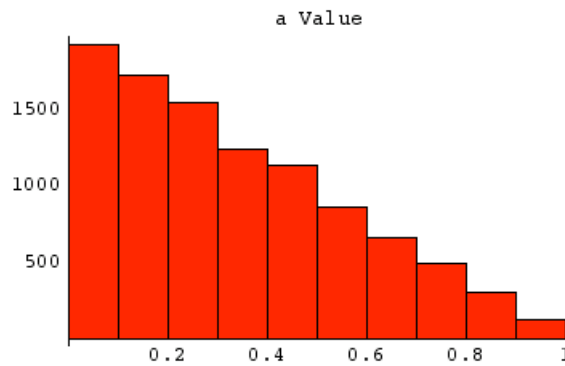


Figure 7.2: Distribution of  $a$  for Background 2.

Event Type	$P(A)$	$P(B)$
Background 1	0.5	0.25
Background 2	0.25	0.5

Table 7.2: Cut survival probabilities for each event type.

### 7.1.1 Cuts

We define our cuts on variables  $a$  and  $b$  as

$$A = (a > 0.5) \tag{7.1}$$

$$B = (b > 0.5) \tag{7.2}$$

$A$  and  $B$  are true or false statements. If they are false the event is cut. With the cut points defined, we can then calculate the cut survival probability (CSP) for each event type which we represent as  $P(A)$  or  $P(B)$ . In this toy model the CSP's can be calculated analytically because we know the underlying distributions. These values are shown in Table 7.2.

## 7.2 One Background

For this section we discuss the case of a single significant background. Our background prediction is given by Eqn 6.7.

For this example we generated  $1 \times 10^4$  Background 1 events over the whole range of kinematic variables. This leaves us with  $\approx 2200$  background events in the signal region before applying cuts A and B. In Table 7.3, we show the observed number of events for each combination of cuts, the predicted background, and the observed background after applying both cut A and B. The predicted background of  $267.8 \pm 20.6$  agrees well with the  $256 \pm 16$  observed background events.

$N_0$	$2236 \pm 47$
$N_{A\bar{B}}$	$831 \pm 29$
$N_{\bar{A}B}$	$280 \pm 17$
$N_{\bar{A}\bar{B}}$	$869 \pm 29$
Predicted Background	$267.8 \pm 20.6$
Observed Background	$256 \pm 16$

Table 7.3: Single background study.

### 7.2.1 Cut Correlation

To study the effects of cut correlation, we introduce a correlation between the  $a$  and  $b$  variables in Background 1. We add a term linearly dependent on  $b$  to  $a$ , and then rescale  $a$  to reduce the change in background due to just the change in the average value of  $a$ .

$$f(a) = (1 + \epsilon'), a \in [\epsilon'b/(1 + \epsilon'), (1 + \epsilon'b)/(1 + \epsilon)] \quad (7.3)$$

The variable  $\epsilon'$  is the knob we use to tune the correlation. It is closely related to the variable  $\epsilon$  that is described in Section 6.3.1 as is shown in Figure 7.3. For easier comparison to the derivation in Chapter 6, we describe the variation of the model in terms of the  $\epsilon$  variable.

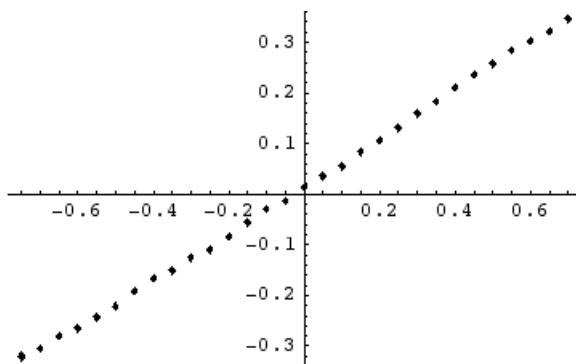


Figure 7.3: The value of  $\epsilon$  (described in Section 6.3.1 as a function of  $\epsilon'$  as given in Equation 7.3.)

The statistical correlation of the cuts changes as  $\epsilon$  changes, as we would expect.

As shown in Figure 7.4, the correlation goes from highly positive with negative  $\epsilon$  to highly negative correlated with positive  $\epsilon$ .

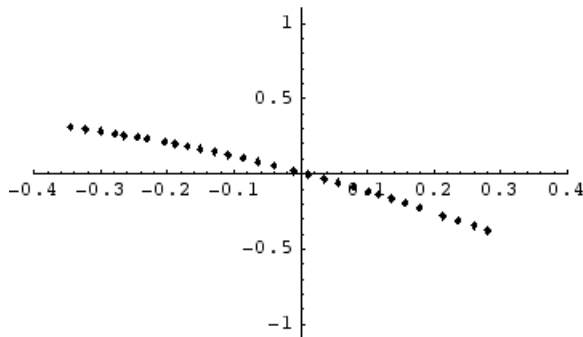


Figure 7.4: The statistical correlation,  $\rho$ , as a function of  $\epsilon$ .

We show the predicted and observed background in Figure 7.5. As  $\epsilon'$  increases the background in data increases, as the correlation increases the average value  $a$ , while the predicted background decreases.

We can try to correct for the correlation by adding the first order correlation term of Eqn 6.73 as

$$C_\epsilon = N_0 \left( \epsilon(P(B) + \frac{P(A|B)P(B)}{P(\bar{A}|B)}) \right) \quad (7.4)$$

In Figure 7.5, we show the prediction with  $C_\epsilon$  added. It improves the agreement for a fairly wide range of  $\epsilon$ . We then show the effect of the practical correction of Eqn. 6.74 on the prediction in Fig. 7.6. This improves the agreement for all values of  $\epsilon$  although the agreement is not as good for small values of  $\epsilon$ .

### 7.3 Two Backgrounds

In this case we add events from Background 2. In Fig. ??, we show the distribution of Background 1, Background 2, and an equally weighted combination of the two backgrounds. We can see how the two variables which are uncorrelated for the separate

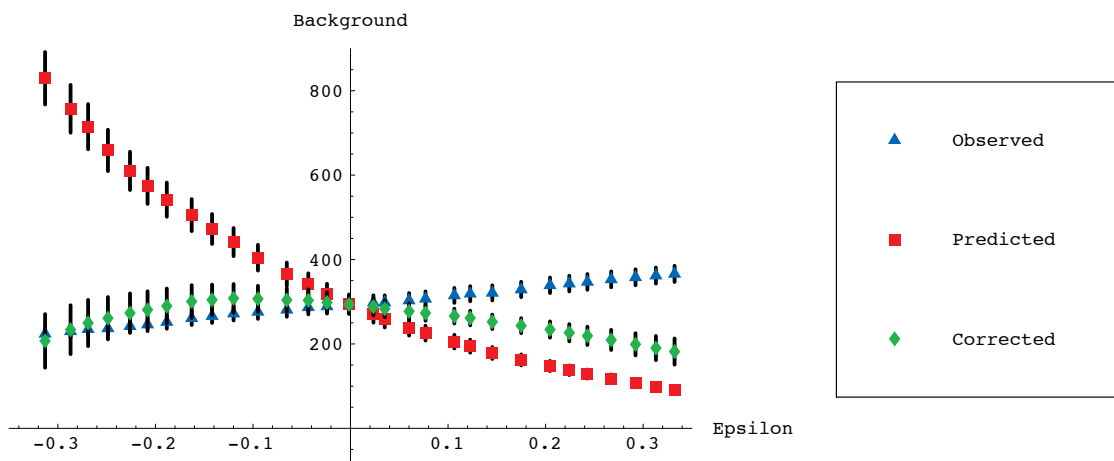


Figure 7.5: Predicted and observed background for different levels of correlation between  $a$  and  $b$ . Blue triangles are data background, red squares are predicted, and green diamonds are predicted plus first order  $\epsilon$  correction (Eqn. 7.4). The x-axis is  $\epsilon$ .

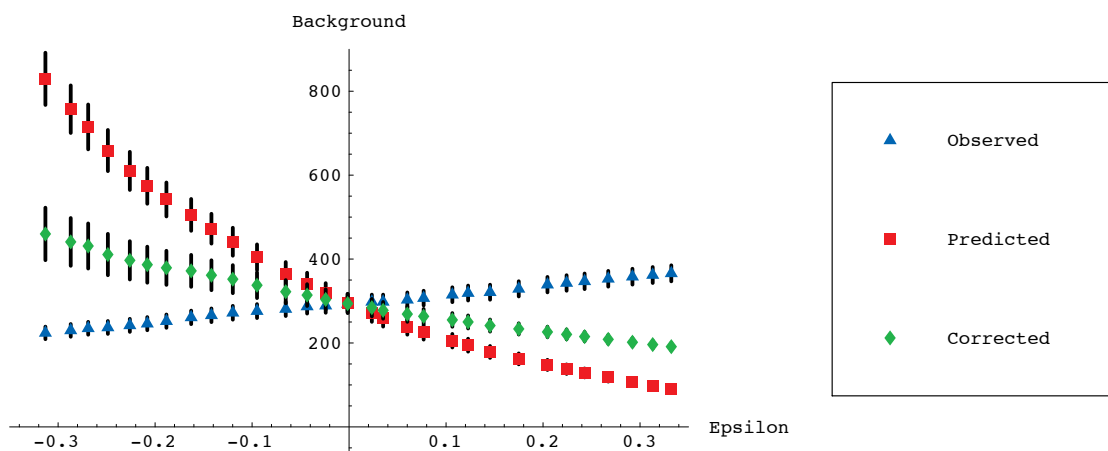


Figure 7.6: Predicted and observed background for different levels of correlation between  $a$  and  $b$ . Blue triangles are data background, red squares are predicted, and green diamonds are predicted plus practical  $\epsilon$  correction (Eqn. 6.74). The x-axis is  $\epsilon$ .

backgrounds, but are strongly correlated when both backgrounds are present.

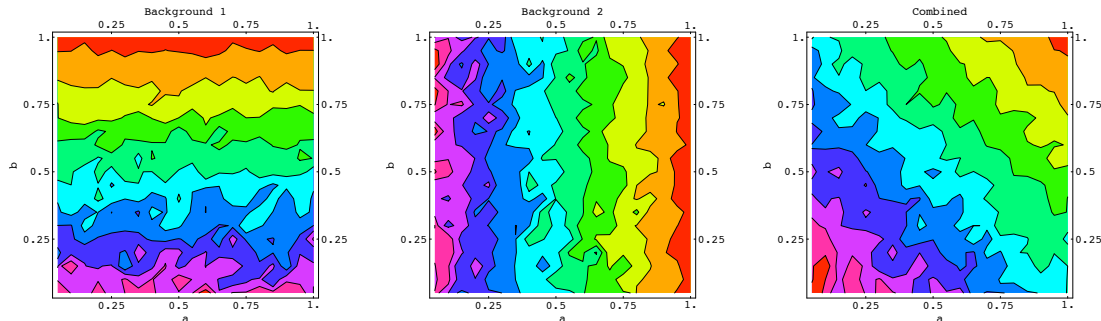


Figure 7.7: Contour plots of the distribution of  $a$  and  $b$  for backgrounds 1 and 2 and an equally weighted combination of the two.

### 7.3.1 One background calculation

We begin by calculating with the false assumption that there is a single background mode. We vary the relative admixture of Background 2. The discrepancy between the prediction and the observed background increases as the the number of background events from the second source increases. In Figure 7.8, we show the variation of predicted and observed background as the number of Background 2 events increases while holding the total number of background events constant.

### 7.3.2 Correction

We now apply the correction term, Eqn. 6.18, to the background prediction.

In the case of this toy model, we know the values of  $N_1$  and  $N_2$  because we have set them. In a real analysis, it would be necessary to determine these values through either Monte Carlo studies or studies of different signal regions which are then extrapolated into the signal box. The differences in the cut probabilities,  $\Delta_A$  and  $\Delta_B$ , also need to be determined from outside sources. In Figure 7.8, we show the

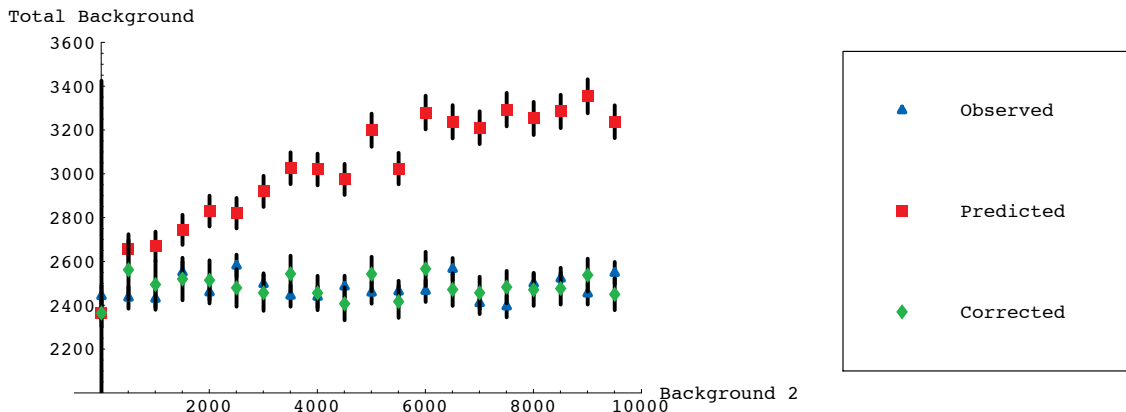


Figure 7.8: Predicted and observed background for different admixtures of a second background source. Red squares are predicted background (without second background correction), blue triangles are the observed background in data, and green diamonds are the corrected background. The x-axis is number of generated Background 2 events, the total number of events,  $N_1 + N_2$ , was held constant at  $2 \times 10^4$ .

results of keeping the total number of background events the same while increasing the fraction of Background 2 events. In this model  $\Delta_A = -25\%$  and  $\Delta_B = 25\%$ . Since the probability differences are of opposite signs the correction factor is negative and reduces the predicted background.

### 7.3.3 Model 2

We can change the model so that the differences in cut survival probability have the same sign inducing a positive correction. We alter our original model so that Background 1 has the same linearly decreasing distribution in both cut variables, while Background 2 has a uniform distribution in each cut variables. The probability distribution functions for  $a$  and  $b$  are shown in Table 7.4. This produces values for the differences in the cut variables of  $\Delta_A = \Delta_B = 0.25$ . We then can see in Figure 7.9 that the uncorrected prediction now under predicts the background and correction is positive.

Background	$a$	$b$
1	$f(a) = 1 - a, a \in [0, 1]$ $f(a) = 0, a \notin [0, 1]$	$f(b) = 1 - b, b \in [0, 1]$ $f(b) = 0, b \notin [0, 1]$
2	$f(a) = 1, a \in [0, 1]$ $f(a) = 0, a \notin [0, 1]$	$f(b) = 1, b \in [0, 1]$ $f(b) = 0, b \notin [0, 1]$

Table 7.4: Probability distribution functions for the variables of each event type in Model 2.

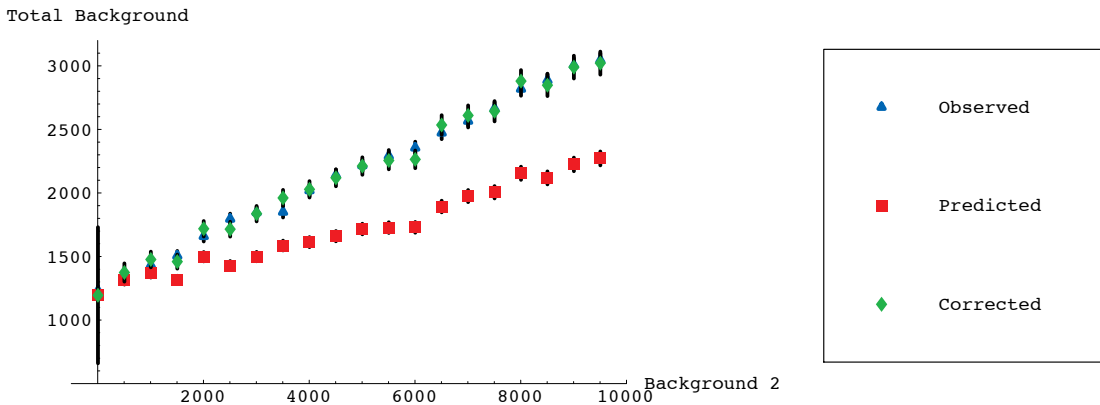


Figure 7.9: Predicted and observed background for different admixtures of Background 2 for Model 2. Red squares are predicted background (without second background correction), blue triangles are the observed background in data, green diamonds are the corrected prediction. The x-axis is the number of generated Background 2 events, the total number of events,  $N_1 + N_2$ , was held constant at  $2 \times 10^4$ .

## CHAPTER 8

### BACKGROUND ANALYSIS

It is necessary to predict the background to the signal modes. These backgrounds are primarily  $K_L \rightarrow \pi^0\pi^0\pi^0$  decays and interactions of neutrons in the beam core. It is difficult to simulate these backgrounds for a variety of reasons. The amount of Monte Carlo necessary to adequately predict the background level from  $K_L \rightarrow \pi^0\pi^0\pi^0$  is difficult to produce. The core neutrons are difficult to simulate because accurately reproducing low-energy hadronic interactions is problematic. Additionally, it is difficult to normalize a neutron Monte Carlo sample to the data with any certainty. Therefore we use the data based bifurcation analysis technique described in Chapters 6 and 7 rather than a Monte Carlo based background prediction.

#### 8.1 Kaon Background Modes

The primary backgrounds for our analysis come from other  $K_L$  decay modes in the detector. There are several potential kaon decay modes which could produce backgrounds, including both  $K_L \rightarrow \pi^0\pi^0\pi^0$  and  $K_L \rightarrow \pi^0\pi^0$ . The charged kaon decay modes are not a significant background source.

##### 8.1.1 $K_L \rightarrow \pi^0\pi^0\pi^0$

The primary background to  $K_L \rightarrow \pi^0\pi^0\nu\bar{\nu}$  and  $K_L \rightarrow \pi^0\pi^0P$  is the decay  $K_L \rightarrow \pi^0\pi^0\pi^0$ . As the  $\pi^0$  decays to 2 photons with a branching ratio of 98.8%, this normally has six photons in the final state, if we miss two of the photons then this can mimic the final states of the signal decays which have 4 photon final states. The primary difference is that the peak of the  $P_T$  distribution for  $K_L \rightarrow \pi^0\pi^0\pi^0$  is lower than that

of  $K_L \rightarrow \pi^0\pi^0\nu\bar{\nu}$  or  $K_L \rightarrow \pi^0\pi^0P$ .

There are two causes of missing photons in the final state, photon inefficiency and photon fusion. Photon inefficiency occurs when a photon either does not produce a detectable signal in one of the detector elements. This can occur either because of geometric inefficiency, where photon did not strike an active detector element, or detector inefficiency, where the photon does not interact in the detector or interacts via the photo-nuclear effect and does not produce a detectable in-time signal. The second cause of missing photons is photon fusion in the CsI calorimeter. Here two photons strike close to each other in the CsI array. If the photons are close enough only one cluster is reconstructed.

The requiring four clusters in the CsI for reconstructions allows three different channels for  $K_L \rightarrow \pi^0\pi^0\pi^0$  to be a background depending on the number of photon fusions and missing photons. The relative level of background from each channel was found using our  $K_L \rightarrow \pi^0\pi^0\pi^0$  Monte Carlo. We assumed there was a minimum separation of two photons at which they could be distinguished. Applying our setup cuts, we find that the  $K_L \rightarrow \pi^0\pi^0\pi^0$  background is predominately from events with two missing photons. The relative background levels of the different channels under different effective separations are shown in Table 8.1. The background events generally have low  $P_T$  and mass values compared to signal events. The  $P_T$  of  $K_L \rightarrow \pi^0\pi^0\pi^0$  events increases for vertices which are closer to CsI face, Fig 8.2. The different channels have similar distributions of kinematic variables as shown in Fig 8.1.

### 8.1.2 $K_L \rightarrow \pi^0\pi^0$

It is possible for a  $K_L \rightarrow \pi^0\pi^0$  event to be poorly reconstructed or have extra energy deposited by accidentals, so that the event has a high  $P_T$  and low invariant mass.

$K_L \rightarrow \pi^0 \pi^0 \pi^0$ Background	Maximum Fusion Separation		
	7 cm	10 cm	14 cm
2 Missing Photons	$(97.0 \pm 1.4)\%$	$(96.1 \pm 1.4)\%$	$(94.4 \pm 1.4)\%$
1 Missing Photon, 1 Fusion	$(2.4 \pm 0.2)\%$	$(3.3 \pm 0.2)\%$	$(4.8 \pm 0.2)\%$
2 Fusion	$(0.7 \pm 0.1)\%$	$(0.7 \pm 0.1)\%$	$(0.8 \pm 0.1)\%$

Table 8.1: Relative levels of different types of  $K_L \rightarrow \pi^0 \pi^0 \pi^0$  background under different levels of photon separation efficiency.

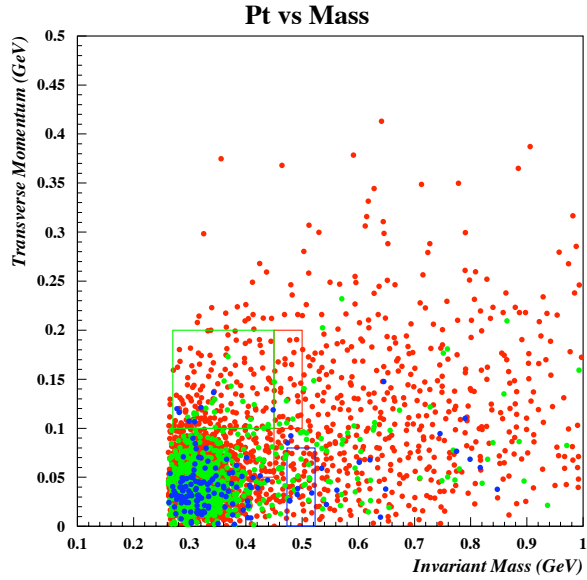


Figure 8.1:  $K_L \rightarrow \pi^0 \pi^0 \pi^0$  Monte Carlo background events in  $P_T$  vs invariant mass plane. Red dots represent events with no photon fusion, green dots are events with one photon fusion, and blue dots have 2 photon fusions.

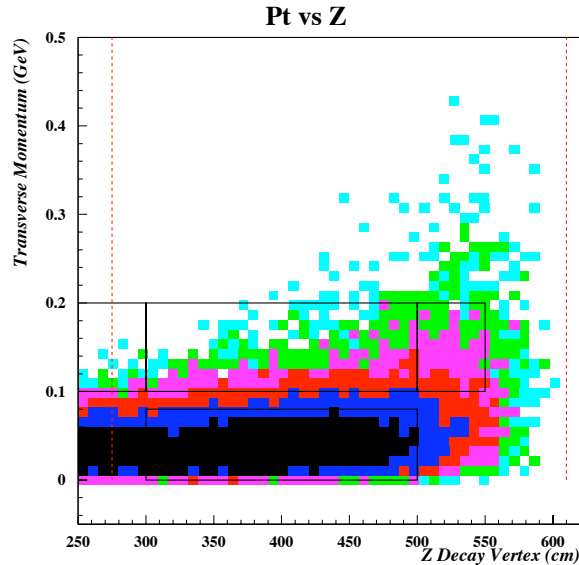


Figure 8.2: Distribution of Monte Carlo  $K_L \rightarrow \pi^0 \pi^0 \pi^0$  events in  $P_T$  - $Z$  plane.

These events are primarily in the High  $P_T$  background region.

### 8.1.3 Charged Kaon Decays

The various charged decays of  $K_L$  are not a significant source of background at this sensitivity. These decays

One source of charged particles is the Dalitz decay of  $\pi^0$ 's into  $e^+e^-\gamma$ . This decay is included in our simulations of  $K_L \rightarrow \pi^0 \pi^0 \pi^0$  and  $K_L \rightarrow \pi^0 \pi^0$ . This is not a significant source of backgrounds.

## 8.2 Neutron Background

The e391a beam has a neutron to kaon ratio of approximately 60 to 1 [2]. These neutrons can produce backgrounds in a variety of ways. Neutrons directly interacting with the detector can produce showers which can be misinterpreted as photon showers. Additionally,  $\pi^0$ 's can be produced by neutron interactions. The largest source of

these interactions is the vacuum membrane which hung down into the membrane during this run as described in Sect. 2.2.1. In general low energy neutrons are difficult to simulate. Additionally, we do not know the actual distribution of the membrane in the beam which produces core neutron events. Therefore it necessary to produce estimates of the neutron background from the data itself. We can predict the background from the core neutrons hitting the membrane by fitting the reconstructed  $Z$  distribution outside the signal box and extrapolating into the signal box.

### 8.2.1 Core Neutrons

Neutrons which are part of the central beam are called core neutrons. These neutrons primarily interact with the vacuum membrane which is in the beamline during Run I. They produce high  $P_T$  four gamma events similar to the halo neutrons. These are localized at the position of the vacuum membrane 60 cm from the CsI face.

### 8.2.2 Halo Neutrons

The beam is surrounded by a halo of neutrons. Halo neutrons are generally produced by beam interaction with the collimators. The beam has a low level of halo neutrons relative to the beam intensity. The primary source of halo neutron background is from the interaction of the halo with CC02, which is the upstream detector element closest to the beam. This produces high  $P_T$  four gamma events. They are localized in  $Z$  at the downstream edge of CC02.

## 8.3 Application of the Bifurcation Analysis

To predict the number of background events, we begin by using Eqn 6.7. This assumes there is a single background source and no correlations between the sets of cuts.

Cut Correlation Values $K_L \rightarrow \pi^0\pi^0\pi^0$						
Cuts	Setup Cuts		Cut Set A		Cut Set B	
	Data	MC	Data	MC	Data	MC
Setup	-1	-1	0.0526	0.0146	-0.0487	-0.0544
Set A	0.0526	0.0146	-1	-1	0.0311	0.0122
Set B	-0.0487	-0.0544	0.0311	0.0122	-1	-1

Table 8.2: Statistical correlation between setup, set A, and set B cuts in  $K_L \rightarrow \pi^0\pi^0\pi^0$  background region. Monte Carlo values are for  $K_L \rightarrow \pi^0\pi^0\pi^0$  events.

For the bifurcation analysis we divide our cuts into:

- Setup: Fusion Neural Network, Gamma Fiducial, Energy Ratio, Gamma E.D.I., CsI Veto, BA Veto
- A: Photon veto cuts. CC02, CC03, CC05, Front Barrel, Main Barrel
- B: Gamma Quality and Reconstruction cuts. Gamma Energy, Gamma RMS,  $\chi^2$ , 2<sup>nd</sup> Best  $\chi^2$

Applying cuts A and B to the  $K_L \rightarrow \pi^0\pi^0\pi^0$  background region, we find they a statistical correlation of 0.031. This is summarized in Table 8.2. A statistical correlation with an absolute value of less than 0.1 indicates the cuts are not linearly correlated. In Section 8.4.3, we estimate the uncertainty to the background prediction arising from this level of cut correlation.

The  $K_L \rightarrow \pi^0\pi^0\pi^0$  background with the setup cuts applied is dominated by events with two missing photons. One fusion events are a few percent of the  $K_L \rightarrow \pi^0\pi^0\pi^0$  background and two fusion events are less than one percent. Additionally, the veto survival probability of the cuts we use does not vary greatly between the different background channels. The core neutron background is small enough (see below) that it is not a problem for using the bifurcation analysis.

To check the background prediction methodology, we applied the technique to

Region	$N_{A\bar{B}}$	$N_{\bar{A}B}$	$N_{\bar{A}\bar{B}}$	Background Prediction	Data
Low $P_T$	$72 \pm 8.5$	$115.0 \pm 10.7$	$393 \pm 19.8$	$21.1 \pm 3.34$	13
High Mass	$4.0 \pm 2.0$	$3.0 \pm 1.7$	$46 \pm 6.8$	$0.78 \pm 0.48$	1
Low $Z$	0	0	0	0	0
High $Z$	0	$6.0 \pm 2.4$	0	0	0

Table 8.3: Background prediction for regions neighboring the signal box.

Cut Set	Number of Events in Signal Box
Setup Cuts	$104.0 \pm 10.2$
$N_{A\bar{B}}$	$18.0 \pm 4.2$
$N_{\bar{A}B}$	$2.0 \pm 1.4$
$N_{\bar{A}\bar{B}}$	$83 \pm 9.1$
Background Prediction	$0.43 \pm 0.32$

Table 8.4: Number of events in signal box for various cut conditions and  $K_L \rightarrow \pi^0\pi^0\pi^0$  background prediction.

regions near the signal box. The Low  $P_T$  region is defined by same bounds in  $Z$  and invariant mass as the signal region and a  $P_T$  between 50 and 100 MeV. The High Mass region is defined by the same bounds in  $Z$  and  $P_T$  as the signal region and a mass between 450 and 550 MeV. The High and Low  $Z$  regions have the same bounds in invariant mass and  $P_T$  as the signal region and have reconstructed vertices between 500 to 550 cm and 250 to 300 cm respectively. The measurements and predictions are compared in Table 8.3. There is a significant discrepancy in the Low  $P_T$  region, which can be explained by cut correlation as will be shown in sect:correlation.

## 8.4 Background Prediction Errors

The  $K_L \rightarrow \pi^0\pi^0\pi^0$  background prediction has two sources of systematic error, the first is contamination from other decay modes. The second is correlation between the cut sets producing error into our prediction.

### 8.4.1 Core Neutron Background

The primary source of background events, besides  $K_L \rightarrow \pi^0\pi^0\pi^0$ , are the core neutrons. To determine the impact of core neutron interactions contaminating the bifurcation analysis, we use Eqn 6.18. The first step is estimating the number of core neutrons in the signal box under the setup cuts. We do this by fitting the distribution of core neutron events in data outside the fiducial Z region and extrapolating it into the fiducial region.

We would like to fit the distribution under the final cut conditions, but the number of events in the region with  $z$  greater than 500 cm and  $P_T$  greater than 0.1 GeV/c is too small to fit when all cuts are applied. We therefore fit using a loose set of cuts. We remove the BA cut, the gamma E.D.I. cut, and the gamma T.D.I. cut. Additionally we apply the reverse of cuts A and B. With these sets of cuts the core neutron peak in the high  $P_T$  -high Z region is clearly visible and can be fit with a Gaussian.

The primary membrane peak of the core neutrons is fit by a Gaussian. To account for a possibly non-Gaussian tail to the core neutron peak, we assume a flat distribution underneath the peak. The density of this distribution is calculated by subtracting off the  $K_L \rightarrow \pi^0\pi^0\pi^0$  contribution found by Monte Carlo. Using our  $K_L \rightarrow \pi^0\pi^0\pi^0$  Monte Carlo normalized to the  $K_L \rightarrow \pi^0\pi^0$  peak significantly over predicts this background. However the shape of the background is similar in data and Monte Carlo. We reduce the  $K_L \rightarrow \pi^0\pi^0\pi^0$  by a factor of 3.3 from its' normalized value to match the data. Then what remains is fit by a Gaussian plus a straight line. Integrating this function over the fiducial region gives an estimate of the background as  $248 \pm 4_{\text{stat.}} + 124_{\text{syst.}}$ . The large systematic error is from uncertainty over the normalization of the  $K_L \rightarrow \pi^0\pi^0\pi^0$  sample which we subtract off. The application of

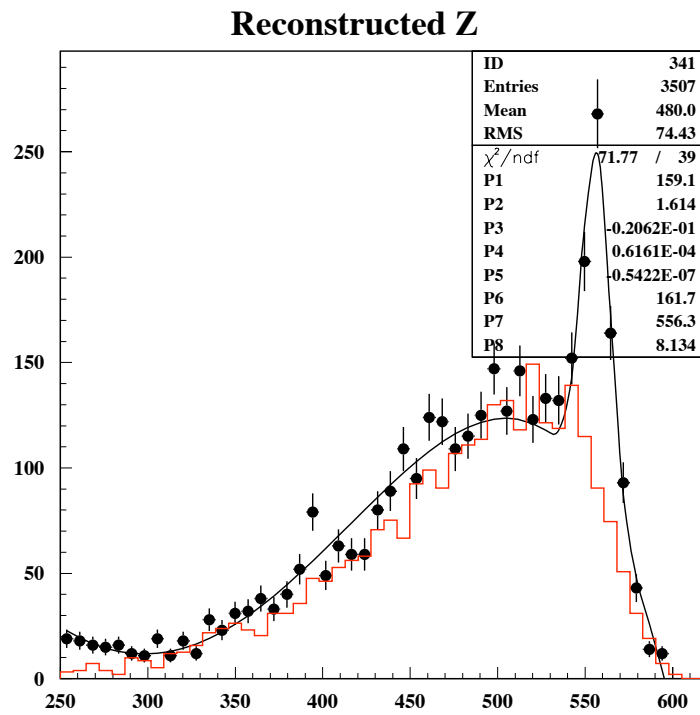


Figure 8.3: Reconstructed Z distribution with loose cuts and  $P_T$  greater than 100 Mev/c. Fit with a 4th-order polynomial plus a Gaussian. Red line is scaled  $K_L \rightarrow \pi^0\pi^0\pi^0$  Monte Carlo.

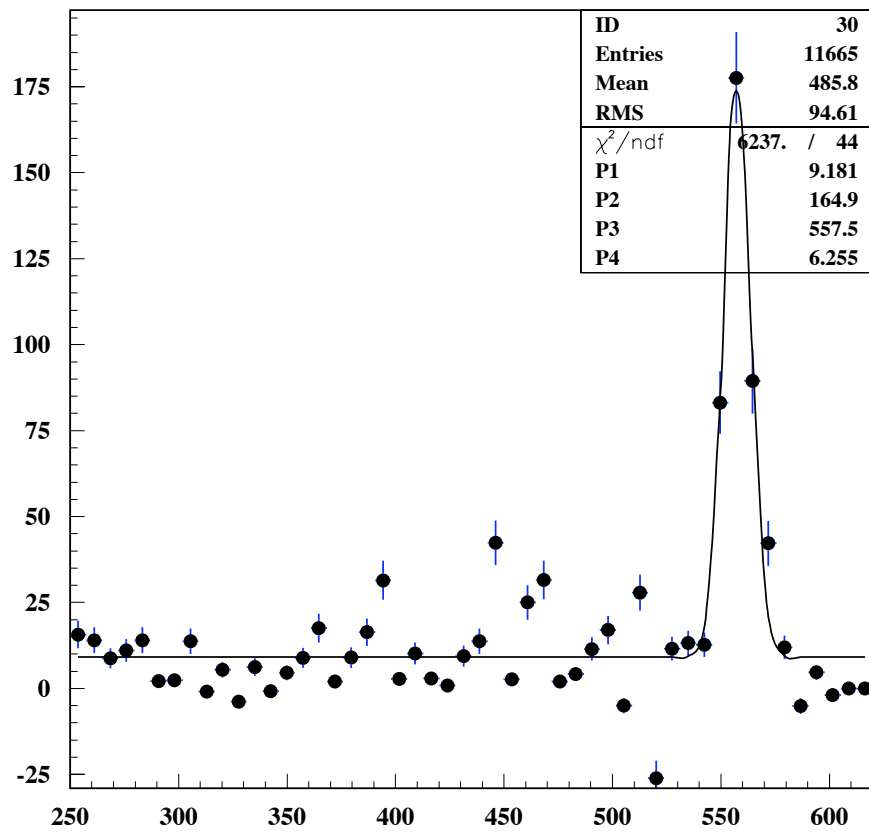


Figure 8.4: Reconstructed Z distribution with loose cuts and  $P_T$  greater than 100 Mev/c with scaled  $K_L \rightarrow \pi^0\pi^0\pi^0$  Monte Carlo subtracted. Fit with a straight line plus a Gaussian.

$K_L \rightarrow \pi^0\pi^0\pi^0$ Channel	Number of Events Setup Cuts	Background Survival Probability	
		Cut A	Cut B
2 Missing Photons	9087	$(59.4 \pm 1.0)\%$	$(11.6 \pm 0.4)\%$
1 Missing Photon, 1 Fusion	309	$(59.2 \pm 4.4)\%$	$(7.8 \pm 1.7)\%$
2 Fusion	64	$(65.6 \pm 13.0)\%$	$(17.2 \pm 5.6)\%$

Table 8.5:  $K_L \rightarrow \pi^0\pi^0\pi^0$  background survival probability from  $K_L \rightarrow \pi^0\pi^0\pi^0$  Monte Carlo.

the rest of the setup cuts reduces this by a factor of  $\approx 115$ .

Producing a predicted total core neutron background in the signal region of  $2.16 \pm 0.03_{\text{stat.}} \pm 1.05_{\text{sys.}}$  under the setup cuts, before the application of cuts A and B. This corresponds to  $N_2$  in Eqn 6.18.

The next step in applying Eqn 6.18 is finding the differences in cut survival probabilities,  $\Delta_A$  and  $\Delta_B$ . We use the data in the High  $P_T$  - High  $Z$  region to estimate this. We find that the cut survival probabilities do differ significantly with  $\Delta_A = (26.4 \pm 1.3)\%$  and  $\Delta_B = (8.6 \pm 0.5)\%$ . This results in a correction to the background prediction of  $0.06 \pm 0.05$  events.

#### 8.4.2 Other $K_L \rightarrow \pi^0\pi^0\pi^0$ Background Channels

As discussed in Section 8.1.1 there are three channels through which  $K_L \rightarrow \pi^0\pi^0\pi^0$  events can become backgrounds to our signal. The primary source of  $K_L \rightarrow \pi^0\pi^0\pi^0$  background at the setup cut stage are events with two missing photons. The second largest source are events with 1 missing photon and 1 photon fusion. Using Monte Carlo we estimate that  $(3.3 \pm 0.2)\%$  of the  $K_L \rightarrow \pi^0\pi^0\pi^0$  background are 1 missing and 1 fusion events. We estimate the difference in cut survival probabilities between the three modes using Monte Carlo as shown in Table 8.5 and 8.6.

Background Channel	$N_1$	$N_2$	$\Delta_A$	$\Delta_B$	Change
$K_L \rightarrow \pi^0\pi^0\pi^0$ 1 Fusion	100.6	3.4	4.4 %	3.8 %	$6.8 \times 10^{-3}$
Core Neutron	101.9	2.1	26.4%	8.6%	0.06

Table 8.6: Effects of contamination on  $K_L \rightarrow \pi^0\pi^0\pi^0$  bifurcation background prediction.  $N_1$  is the number of  $K_L \rightarrow \pi^0\pi^0\pi^0$  2 missing photon events under the setup cuts.  $N_2$  is the number of contaminating events under the setup cuts.  $\Delta_A$  and  $\Delta_B$  are the difference in the veto survival probabilities.

### 8.4.3 Correlation

We divided our cuts on the basis of minimizing cut correlation. However, as discussed in Sect. 8.3, there is some correlation. We use Eqn 6.74 to estimate the error in our prediction from what correlation there is. We determined  $\epsilon$  using events in the Low  $P_T$  region. The value of  $\epsilon$  is  $(-0.049 \pm 0.035)$ . We first apply Eqn 6.74 to the Low  $P_T$  region and find a correction of  $-6.67 \pm 4.81$ . This correction brings the prediction in Table 8.3 into much better agreement with data. Next, we apply this procedure to the signal region. We calculate a systematic error of  $0.12 \pm 0.12$  background events in the signal region.

### 8.4.4 Combining Systematic Errors

We add the systematic error from correlation and the core neutrons in quadrature. In Sect. 6.2.3, we discussed how multiple background sources are actually an implicit correlation. However, since our estimate of the correlation error is based on the strength of correlation in the  $K_L \rightarrow \pi^0\pi^0\pi^0$  Low Mass-Low  $P_T$  region where there is no significant core neutron contamination this does not cause any overcounting.

The total error for our background prediction is 0.32 events statistical error and 0.13 event systematic error.

Systematic Error Source	Contribution
Core Neutron Contamination	0.06
$K_L \rightarrow \pi^0 \pi^0 \pi^0$ 1 Fusion Contamination	0.01
Cut Correlation	0.12
Total Systematic Error	0.13

Table 8.7: Contributions to background prediction systematic error.

## CHAPTER 9

### RESULTS AND ERROR ANALYSIS

#### 9.1 Single Event Sensitivity

From the acceptance of the  $K_L \rightarrow \pi^0 \pi^0 \nu \bar{\nu}$  and the flux we can determine our single event sensitivity.

$$\text{S.E.S.} = \frac{1}{A_{K_L \rightarrow \pi^0 \pi^0 \nu \bar{\nu}} \times N_{K_L}}. \quad (9.1)$$

Our single event sensitivity for  $K_L \rightarrow \pi^0 \pi^0 \nu \bar{\nu}$  is  $(1.21 \pm 0.06) \times 10^{-5}$ . The calculated sensitivities for the other modes are shown in Table 5.3 and Fig. 5.16.

#### 9.2 Opening the Box

We open the box and observe one event in the signal box. This is consistent with our background prediction of  $0.43 \pm 0.32_{\text{stat.}} \pm 0.13_{\text{sys.}}$ . The event is located near the low  $P_T$  edge of the signal box and well inside the fiducial Z region, indicating that it is likely a  $K_L \rightarrow \pi^0 \pi^0 \pi^0$  event. The results are shown in Figures 9.1 and 9.2.

##### *9.2.1 Limit*

We use Poisson statistics to calculate an upper limit for the branching ratio of  $K_L \rightarrow \pi^0 \pi^0 \nu \bar{\nu}$ . At the 90% confidence level with one observed background event the limit is

$$\text{Br}(K_L \rightarrow \pi^0 \pi^0 \nu \bar{\nu}) \leq 3.89 \times \text{S.E.S} \quad (9.2)$$

$$\leq 4.7 \times 10^{-5}. \quad (9.3)$$

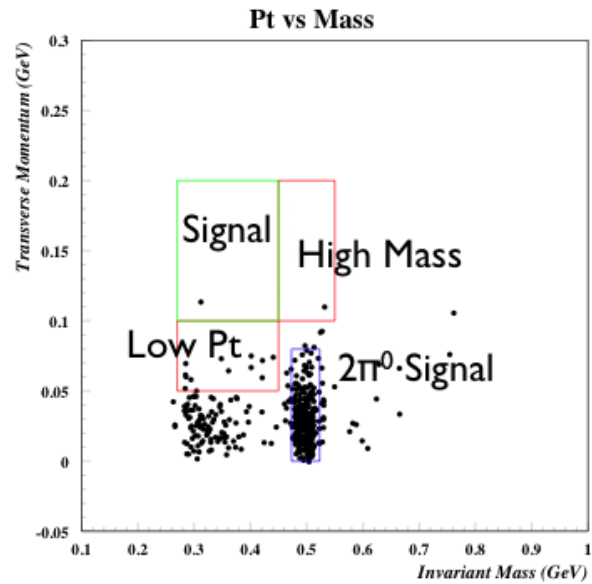


Figure 9.1: Plot of  $P_T$  versus invariant mass from data with an opened signal box. There is one event inside the signal region. All cuts are applied and only events in the fiducial Z region (300 to 500 cm) are shown.

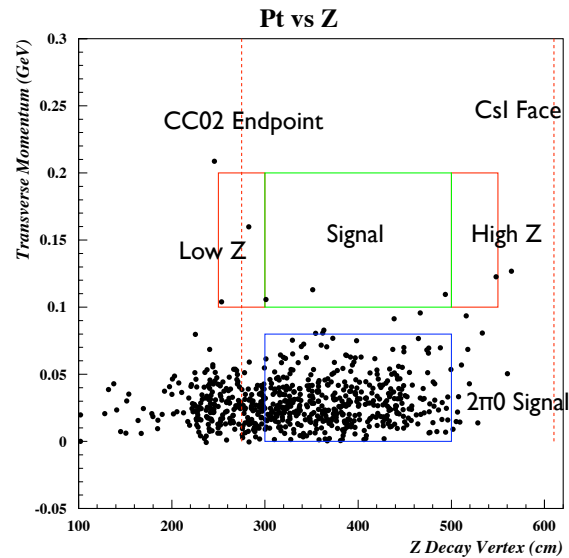


Figure 9.2: Plot of  $P_T$  versus reconstructed Z from data with an opened signal box. All cuts are applied and events with all invariant mass values are shown.

In Figure 9.3, we show the limits we establish for  $K_L \rightarrow \pi^0 \pi^0 \nu \bar{\nu}$  with and without the decay form factor, and for  $K_L \rightarrow \pi^0 \pi^0 X$  with masses of up to 200 MeV.

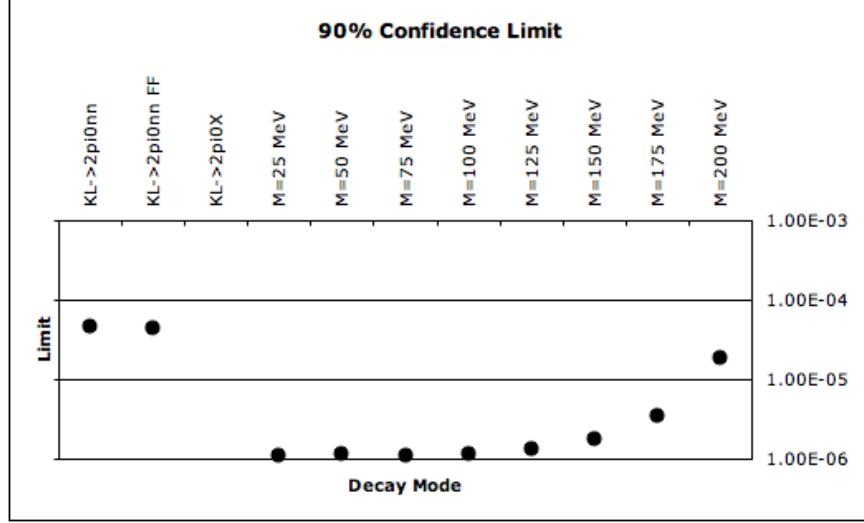


Figure 9.3: Limits at the 90% confidence level for  $K_L \rightarrow \pi^0 \pi^0 \nu \bar{\nu}$  and  $K_L \rightarrow \pi^0 \pi^0 P$  decay modes.

## 9.3 Error Analysis

### 9.3.1 Acceptance and Flux Errors

Errors in the acceptance and flux are caused primarily by discrepancies between data and Monte Carlo. For cuts where there appeared to be a significant discrepancy, the cut was removed from the flux calculation and the impact of that cut on the signal acceptance was determined using data. However, there are still smaller discrepancies that introduce error in our acceptance and flux calculations. One important source of these errors is the energy calibration of the detector elements.

$$\text{S.E.S.} = \frac{1}{A_{K_L \rightarrow \pi^0 \pi^0 \nu \bar{\nu}} \times N_{K_L}} = \frac{\text{BR}(K_L \rightarrow \pi^0 \pi^0) \times A_{K_L \rightarrow \pi^0 \pi^0}}{A_{K_L \rightarrow \pi^0 \pi^0 \nu \bar{\nu}} \times N_{K_L \rightarrow \pi^0 \pi^0}}. \quad (9.4)$$

Veto	Cut Point	Change in Acceptance	
		Lower Energy Scale (80%)	Higher Energy Scale (120%)
CC02	1 MeV	0.0 %	0.0 %
CC03	2.5 MeV	1.6 %	1.4%
CC05	4 MeV	0.7 %	0.3 %
Front Barrel	4 MeV	1.6%	1.0 %
Main Barrel	2 MeV	1.7%	2.4 %
CsI Veto	3 MeV	0.3%	0.0 %

Table 9.1: Variation in  $K_L \rightarrow \pi^0\pi^0$  acceptance due to variation in energy scale for photon vetoes.

### 9.3.2 Energy Calibration Errors

To estimate the impact that incorrect detector calibration may have on our acceptance and flux calculation we varied the cut points of our photon vetoes. Then we determined the change of acceptance in data for the  $K_L \rightarrow \pi^0\pi^0$  decay mode. The change in acceptance for variations in energy scale of 20% for each photon veto is a few percent. The results are summarized in Table 9.1.

Taking the largest variation for each photon veto and summing the contributions we calculate a 3.7% error in the acceptance from the photon vetoes' energy scale.

### 9.3.3 Other Cuts

We use the acceptance loss difference between  $K_L \rightarrow \pi^0\pi^0$  data and Monte Carlo to determine the systematic errors in acceptance from the other simulated cuts. These values are shown in Table 5.1. There are only three cuts which have statistically significant differences in the acceptance loss. These are the Gamma E.D.I. cut, the Gamma Fiducial cut, and the Gamma RMS cut. Combining the differences from these three cuts, we find a 3.4% systematic error in acceptance from these vetoes.

Region	Acceptance Loss from Non-simulated Cuts
$K_L \rightarrow \pi^0\pi^0$ Low $P_T$ ( $< 50$ MeV)	$(85.9 \pm 0.9)\%$
$K_L \rightarrow \pi^0\pi^0$ High $P_T$ (50-100 MeV)	$(81.0 \pm 3.5)\%$
$K_L \rightarrow \pi^0\pi^0$ All	$(85.5 \pm 0.9)\%$
$K_L \rightarrow \pi^0\pi^0\pi^0$ All	$(89.4 \pm 0.5)\%$

Table 9.2: Acceptance loss from non-simulated cuts in different  $P_T$  regions.

### 9.3.4 Non-Simulated Cuts

Several of our cuts were either not simulated or showed significant discrepancy between their data and Monte Carlo acceptances. For these cuts we used their acceptance losses from  $K_L \rightarrow \pi^0\pi^0$  signals to estimate the acceptance loss for  $K_L \rightarrow \pi^0\pi^0\nu\bar{\nu}$ . The largest difference between these two signal regions is the difference in  $P_T$ . One way to try to understand what impact this has on the acceptance loss from these cuts is to study the difference in acceptance loss in high and low  $P_T$   $K_L \rightarrow \pi^0\pi^0$  events.

There is no significant difference in the acceptance loss between the two  $P_T$  regions as summarized in Table 9.2. This indicates that for the non-simulated cuts there is no significant  $P_T$  dependence in the acceptance loss.

### 9.3.5 Single Event Sensitivity Error

Summing the systematic error contributions quadratically gives us a 7.1% systematic error in the single event sensitivity. The contributions are summarized in Table 9.3. This is an overestimate, because the acceptance errors in  $K_L \rightarrow \pi^0\pi^0$  and  $K_L \rightarrow \pi^0\pi^0\nu\bar{\nu}$  are likely highly correlated.

Systematic Error Source	Contribution
Photon Veto Energy Calibration	3.7%
Other Simulated Cuts	3.4%
Total Acceptance Error	5.0%
$K_L \rightarrow \pi^0\pi^0$ Branching Ratio	0.46%
Total Systematic Error	7.1%

Table 9.3: Contributions to Single Event Sensitivity systematic error.

# CHAPTER 10

## CONCLUSIONS

### 10.1 Results

We have set the first experimental limit on  $K_L \rightarrow \pi^0 \pi^0 \nu \bar{\nu}$ . In addition, we have set the first direct experimental limits on the decay  $K_L \rightarrow \pi^0 \pi^0 P$  where the sgoldstino decay is unobservable. These results are summarized in Table 10.1.

Using Eqn. 1.34, we can constrain the real component of the coupling constant,  $h_{12}^{(D)}$ . These limits are shown in Fig. 10.1.

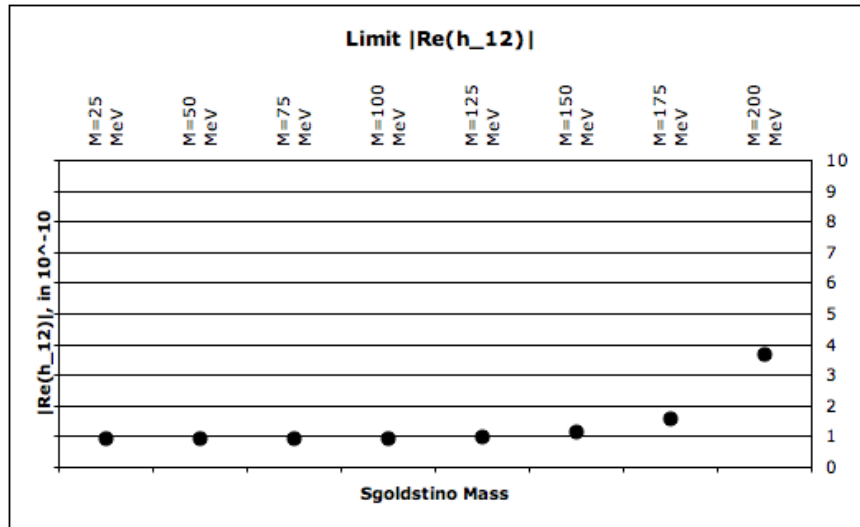


Figure 10.1: Limits on  $|Re(h_{12}^{(D)})|$  versus sgoldstino mass.

### 10.2 Future Prospects

This limit for these modes is background limited with the predicted background level and the compatible observation of one background event. The  $K_L \rightarrow \pi^0 \pi^0 \pi^0$  background is a fundamental background. Scaling to the full data set of Run I with the

Mode	Single Event Sensitivity	Limit (90% Confidence Level)
$K_L \rightarrow \pi^0 \pi^0 \nu \bar{\nu}$	$(1.21 \pm 0.06) \times 10^{-5}$	$4.7 \times 10^{-5}$
$K_L \rightarrow \pi^0 \pi^0 P$		
$M_P = 25\text{MeV}$	$(2.89 \pm 0.06) \times 10^{-7}$	$1.1 \times 10^{-6}$
$M_P = 50\text{MeV}$	$(3.02 \pm 0.09) \times 10^{-7}$	$1.2 \times 10^{-6}$
$M_P = 75\text{MeV}$	$(2.89 \pm 0.09) \times 10^{-7}$	$1.1 \times 10^{-6}$
$M_P = 100\text{MeV}$	$(3.06 \pm 0.09) \times 10^{-7}$	$1.2 \times 10^{-6}$
$M_P = 125\text{MeV}$	$(3.47 \pm 0.11) \times 10^{-7}$	$1.3 \times 10^{-6}$
$M_P = 150\text{MeV}$	$(4.55 \pm 0.15) \times 10^{-7}$	$1.8 \times 10^{-6}$
$M_P = 175\text{MeV}$	$(9.00 \pm 0.35) \times 10^{-7}$	$3.5 \times 10^{-6}$
$M_P = 200\text{MeV}$	$(4.93 \pm 0.38) \times 10^{-6}$	$1.9 \times 10^{-5}$

Table 10.1: Single event sensitivities and limits for the various signal modes and sgoldstino masses.

current background rejection power would produce approximately 5 to 10 background events which would overwhelm the increase in flux resulting in no improvement for the limit. However, the later runs do not have the vacuum membrane hanging in the beam line. This significantly changes the profile of background events. Loosening cuts which are powerful against the core neutron backgrounds (primarily gamma quality cuts) and tightening cuts effective against  $K_L \rightarrow \pi^0 \pi^0 \pi^0$  background (photon vetoes) may allow analysis of larger quantities of data without background limitations. The E391a experiment has taken two runs of data without the vacuum membrane problem which contain approximately ten times sample size of this analysis.

The E391a collaboration currently plans a series of follow up experiments at the new JPARC accelerator facility currently under construction. For this experiment there are several changes that could improve sensitivity to  $K_L \rightarrow \pi^0 \pi^0 \nu \bar{\nu}$ . First, is an improved CsI array with smaller blocks. Smaller blocks will allow for greater fusion rejection power. Since this is a major cause of  $K_L \rightarrow \pi^0 \pi^0 \pi^0$  background this should lead to improved performance.

## REFERENCES

- [1] O.G. Tchikilev et al. Search for light pseudoscalar sgoldstino in  $K^-$  decays. *Phys. Lett. B*, 602:149, 2004.
- [2] H. Watanabe et al. Neutral beam line to study  $K_L^0 \rightarrow \pi^0 \nu \bar{\nu}$  at the KEK 12-GeV proton synchrotron. *Nucl. Inst. Meth. A*, 545:542, 2005.
- [3] David Griffiths. *Introduction to Elementary Particles*. Wiley, 1987.
- [4] J. H. Christenson, J. W. Cronin, V. L. Fitch, and R. Turlay. Evidence for the  $2\pi$  Decay of the  $K_2^0$  Meson. *Phys. Rev. Lett.*, 13:138, 1964.
- [5] Yosef Nir. CP Violation In and Beyond the Standard Model, arXiv:hep-ph/9911321.
- [6] L.S. Littenberg and G. Valencia. The decays  $K \rightarrow \pi \pi \nu \bar{\nu}$  within the standard model. *Phys. Lett. B*, 385:379, 1996.
- [7] A.. Buras G. Buchalla and M. Harlander. CP-conserving and -violating contributions to  $K_L \rightarrow \pi^+ \pi^- \nu \bar{\nu}$ . *Nucl. Phys. B*, 349:1, 1991.
- [8] A. Pais and S. B. Treiman. Pion phase-shift information from  $K_{l4}$  decays. *Physical Review*, 168:1858, 1968.
- [9] Cheng-Wei Chiang and Frederick J. Gilman.  $K_{L,S} \rightarrow \pi \pi \nu \bar{\nu}$  decays within and beyond the standard model. *Phys. Rev. D*, 62:094026, 2000.
- [10] L. Rosset et al. Experimental study of 30000  $K_{e4}$  decays. *Phys. Rev. D*, 15:574, 1977.
- [11] S. Pislak et al. High statistics measurement of  $K_{e4}$  decay properties. *Phys. Rev. D*, 67:072004, 2003.
- [12] Andrea Brignole and Anna Rossi. Flavour non-conservation in goldstino interactions. *Nucl. Phys. B*, 587:3, 2000.
- [13] D. S. Gorbunov and V.A. Rubakov. Kaon physics with light sgoldstinos and parity conservation. *Phys. Rev. D*, 64:054008, 2001.
- [14] D. S. Gorbunov. Light sgoldstino: precision measurements versus collider searches. *Nucl. Phys. B*, 602:213, 2001.
- [15] H.K. Park et al. Evidence for the Decay  $\Sigma^+ \rightarrow p \mu^+ \mu^-$ . *Phys. Rev. Lett.*, 94:021801, 2005.
- [16] Xiao-Gang He et al. Implication of a New Particle from the HyperCP Data on  $\Sigma^+ \rightarrow p \mu^+ \mu^-$ . *hep-ph*, 0509041:0509041, 2005.

- [17] T. Inagaki. E391a Vacuum System. *E391a Technote*, 149:1, 2003.
- [18] M. Doroshenko et al. Undoped CsI calorimeter for the  $K_L \rightarrow \pi^0 \nu \bar{\nu}$  experiment at KEK-PS. *Nucl. Inst. Meth. A*, 545:278, 2005.
- [19] Ken SAKAKSHITA. *Search for the Decay  $K_L \rightarrow \pi^0 \nu \bar{\nu}$* . PhD thesis, Osaka University, 2006.
- [20] R. Brun et al. *GEANT 3.21*. CERN, 1994.
- [21] S. Adler et al. Evidence for the Decay  $K^+ \rightarrow \pi^+ \nu \bar{\nu}$ . *Phys. Rev. Lett.*, 79:2204, 1997.
- [22] Roger Porkess. *Collins Web-linked Dictionary of Statistics*. HarperCollins, 2005.
- [23] Wolfram Reasearch Inc. *Mathematica Edition: Version 5.2*, 2005.